New Frontiers in Galactic Archaeology: Spectroscopic Surveys, Carbon-Enhanced Metal-Poor Stars, and Machine Learning Applications

by

Collin Louis Kielty
B.Sc., University of Washington, 2013

A Thesis Submitted in Partial Fulfillment of the
Requirements for the Degree of

MASTER OF SCIENCE

in the Department of Physics and Astronomy

© Collin Louis Kielty, 2017
University of Victoria

All rights reserved. This thesis may not be reproduced in whole or in part, by photocopying or other means, without the permission of the author.

New Frontiers in Galactic Archaeology: Spectroscopic Surveys, Carbon-Enhanced Metal-Poor Stars, and Machine Learning Applications

by

Collin Louis Kielty
B.Sc., University of Washington, 2013

Supervisory Committee

Dr. K. Venn, Supervisor
(Department of Physics and Astronomy)

Dr. F. Herwig, Departmental Member
(Department of Physics and Astronomy)

Supervisory Committee

Dr. K. Venn, Supervisor
(Department of Physics and Astronomy)

Dr. F. Herwig, Departmental Member
(Department of Physics and Astronomy)

ABSTRACT

Large spectroscopic surveys are trailblazing endeavours in the study of stellar archaeology and near field cosmology. Access to homogeneous databases of thousands of stellar spectra allow for a detailed and statistically satisfying look into the chemical abundance distribution of our Galaxy and its surrounding satellites, ultimately working towards a better understanding of galactic chemical evolution. This thesis presents the work of three new studies at the current frontier of stellar archaeology. Through the first look at carbon-enhanced metal-poor (CEMP) stars using H-band spectra, six new CEMP stars and another seven likely candidates were found within the APOGEE database following Data Release 12. These stars have chemical compositions typical of metal-poor halo stars, however the α-abundances of two stars indicate possible origins in an accreted dwarf galaxy. A lack of heavy element spectral lines impedes further sub-classification of these CEMP stars, however, based on radial velocity scatter, we predict most are not CEMP-s stars which are typically found in binary systems. This preliminary investigation warrants optical observations to confirm the stellar parameters and low metallicities of these stars, to determine the heavy-element abundance ratios and improve the precision in the derived abundances, and to examine their CEMP sub-classifications. Additionally, the first results for the spectroscopic follow up to the *Pristine* survey are presented. Using a sample of 149 stars, a success rate of 70% for finding stars with [Fe/H] ≤ -2.5 and 22% for finding stars with [Fe/H] ≤ -3.0 is reported, significantly higher than other surveys that typically report success rates of 3-4% for recovering stars with [Fe/H] ≤ -3.0. Finally,

the new spectral analysis tool StarNet is introduced. A deep neural network architecture is used to examine both synthetic stellar spectra and SDSS-III APOGEE spectral data and can produce the stellar parameters of temperature, gravity, and metallicity with similar or better precision as the APOGEE pipeline values when trained directly with the APOGEE spectra. StarNet is capable of being trained on synthetic data as well, and is able to reproduce the stellar parameters for both synthetic and APOGEE spectra, including low signal-to-noise spectra, with similar precision to training on the APOGEE spectra itself. The residuals between StarNet predictions and APOGEE DR13 parameters are similar to or better than the differences between the APOGEE DR13 results and optical high resolution spectral analyses for a subset of benchmark stars. While developed using the APOGEE spectral database (real spectra and corresponding ASSET synthetic data with similar normalization functions), StarNet should be applicable to other large spectroscopic surveys like *Pristine*.

Contents

List of Tables

List of Figures

ACKNOWLEDGEMENTS

I would like to thank:

Jane and Steve Kielty for your infinite love and support, for always pushing me to the next summit, and for always encouraging the "what ifs."

Kim Venn for your expertise, encouragement, enthusiasm, and perspective you have given me these past two years both academically and not. I am very much looking forward to our continued collaboration.

Falk Herwig, Pavel Denisenkov, Benoit Coté, Christian Ritter, Austin Davis for your stimulating discussions on theoretical stellar astrophysics and nucleosynthesis.

Douglas Rennehan and Ondrea Clarkson for your support and friendship as classmates and bar-mates, easing the tensions of our first year.

Charli Sakari, Masen Lamb, and Farbod Jahandar for your stellar academic kinship and for helping me decipher the Book of Venn.

Sébastien Fabbro, Teaghan O'Briain, Spencer Bialek and Stephanie Monty for making humans obsolete when processing stellar spectra by developing StarNet.

Nicolas Martin, Piercarlo Bonifacio, and Nicolas Longeard for your experience, exceptional guidance, music preferences, and 3:00am jokes at the INT.

Else Starkenburg, Nicolas Martin, Kris Yoakim, David Aguado for making *Pristine* the remarkable survey it is and for reducing and processing the INT spectra.

The Physics and Astronomy Grads for welcoming me to the Victoria/UVic community as well as for the stimulating discussions at morning coffee, morning paper session, morning tea, lunch, lunch seminar, afternoon tea, afternoon coffee, afternoon gelato, beer o'clock, and any other *insert time here-insert foodstuffs here* events I may have missed.

Adventure friends including but not limited to Ben Gerard, Mara Johnson-Groh, Jason Kezwer, Zack Draper, Jared Keown, Cedar McMechan, Nicolas Riemer,

Brooke MacDonald, Clare Higgs, Mike Chen, Trystyn Berg, Chelsea Spengler, Kyle Oman, James Lane, Stefan Janiszewski, Sean Stettner, Bradley Mitchell, Robert DeVoe, Emery McGraw, Lena Terry, Ryan Steele, and Nathan Bright for keeping my mind clear, my feet grounded in the dirt, my boots in the snow, my hands on the rock, and my eyes on the horizon.

When we contemplate the whole globe as one great dewdrop, striped and dotted with continents and islands, flying through space with other stars all singing and shining together as one, the whole Universe appears as an infinite storm of beauty.

John Muir

DEDICATION

To my family here and above and my friends near and far.

Chapter 1

Introduction

1.1 Stellar Archaelogy

The detailed chemical abundances of stars and their interplay with stellar evolution and galactic evolution comprise the foundation of this thesis. To utilize these chemical abundances with integrity, one must be cognizant of the history of the elements and processes used to determine their abundances. The following sections serve to introduce the nucleosynthetic origins of the elements, how stellar chemical abundances can provide rich insight into the history and evolution of stellar populations, and the spectroscopic techniques used to determine chemical abundances.

1.1.1 Origin of the Elements

I refer the curious reader to Steigman (2007) for a detailed discussion of Big Bang Nucleosynthesis, however, to remain relevant to the scope of this thesis, the finer details of the origins of the Universe, the Big Bang model, and the primordial moments will be passed over and this discussion will begin after the formation of the first elements. Prior to the formation of the first stars, the Universe contained only hydrogen, helium, and trace amounts of lithium and beryllium. A keen observer may note the Galaxy today has a much greater chemical diversity, opening the question on the origin of the heavier elements.

In the hot and dense crucibles of stars the heavy elements are forged through a myriad of formation sites. Whether we consider the ejecta from rapidly rotating stars (Meynet et al., 2006; Chiappini et al., 2006), the yields from core collapse supernovae (SNe) (Nomoto et al., 2006; Tominaga et al., 2014), or the by-products of neutron star

mergers (Argast et al., 2004; Côté et al., 2017), this enriched material is ultimately injected into the interstellar medium, polluting the pristine gas with trace amounts of metals. Later generations of stars formed from this seeded material, locking the chemical signatures of the first generation into their atmospheres. The following overview highlights the principle groups of elements important for this thesis and their formation sites:

Light elements: The formation of the light elements, carbon and oxygen, can be traced to He-burning in post-main sequence stars (Herwig, 2005), the ejecta of Type II supernovae (SNe), and stellar yields from first generation stars (Umeda et al., 2006; Tominaga et al., 2014). The primary production of nitrogen is believed to be linked to the mixing of C and O into the hydrogen-burning shell via convective mixing in massive ($M > 20M_{\odot}$) rotating low metallicity stars (Meynet & Maeder, 2002; Hirschi, 2007). Stars on the asymptotic giant branch (AGB) play an important role in the formation of C in particular as dredge-up events bring C to the surface of the star where it may then be transferred to a binary companion or ejected into the interstellar medium (ISM) via stellar winds. At temperatures above $\sim 2x10^7$K the CNO cycle (Burbidge et al., 1957) becomes the favoured H-burning process for producing helium in the cores and H-burning layers of stars, using C, N, and O as catalysts (Kippenhahn & Weigert, 1994), see Figure 1.1 for a schematic. In this reaction network, the sum of the C, N, and O abundances remains constant, however the abundances of the individual element will vary throughout the course of stellar evolution on the RGB. As CNO cycling occurs deep in the H-burning layer, producing N through the astration of C, this processed material is brought to the surface through convective dredge-up events which result in the enhancement of surface N and the dilution of surface C (Gratton et al., 2000; Spite et al., 2005).

α-elements: The α-elements, typically Mg, Si, S, Ca, and Ti, are those associated with the capture of ^{4}He nuclei during the burning phases in massive stars (typically $> 8M_{\odot}$) and in SNe Type II. Through C-burning, ^{20}Ne is produced. ^{20}Ne will either photodisintegrate into ^{16}O + ^{4}He or capture a ^{4}He nuclei to produce ^{24}Mg. At temperatures around $\sim 2x10^9$K, O-burning produces ^{28}Si + ^{4}He. From here, ^{28}Si will capture free α particles, resulting in a nucleosynthetic chain producing ^{32}S, ^{40}Ca, and ^{44}Ti (Clayton, 1983). Tracing the evolution of these elements is central in studying the chemical evolution of galaxies (see

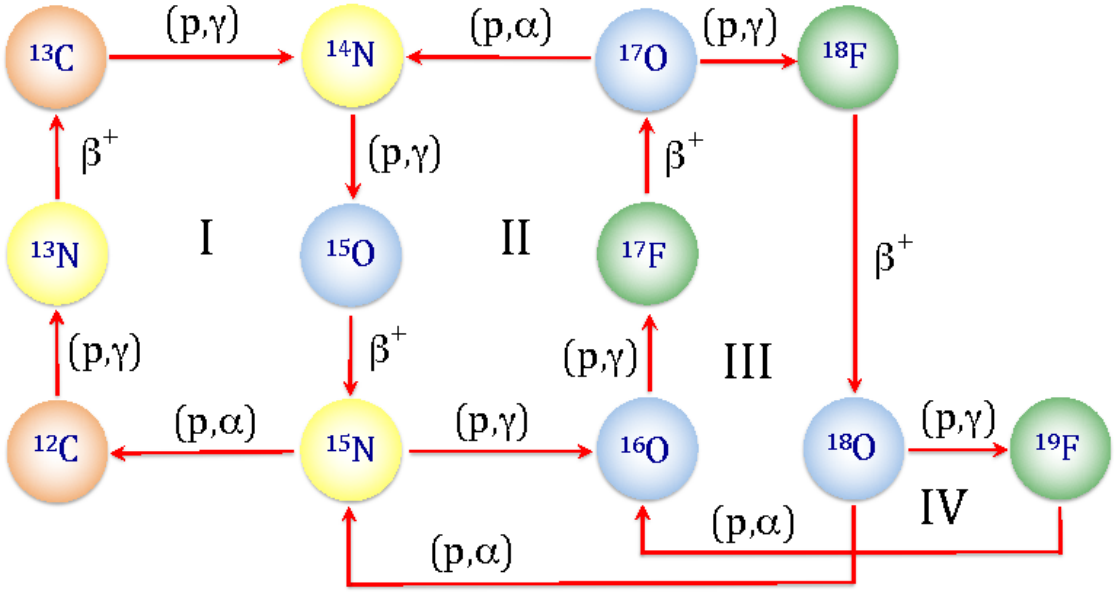

Figure 1.1 The four CNO cycles, adopted from `https://inspirehep.net/record/1445080/plots`. CNO-I is the primary cycle for Sun-like stars where the other cycles play small roles in the Sun or are present only in massive stars.

further discussion in section 1.1.2).

Iron-peak elements: While capable of being produced in SNe Type II, the Fe-peak (elements near Fe on the periodic table) elements appear to be significantly linked with SNe Type Ia (Iwamoto & Saio, 1999; Tominaga et al., 2014), ultimately reflecting galactic chemical evolution on time scales $\gtrsim$ 1 Gyr after periods of star formation.

Neutron-capture elements: The Fe-peak elements mark the heaviest elements capable of being produced via nuclear fusion in stars, meaning all heavier elements up to uranium can only be produced by neutron-capture events. In regions with high neutron densities, light, stable nuclei will capture neutrons, typically producing an unstable heavy isotope. These heavy nuclei decay via the emission of electrons (β- decays) ultimately increasing the atomic number Z of the parent element (see Figure 1.2).

Depending on the neutron densities, there are two primary processes which govern the formation of the heavier elements: the slow-process (s) and the rapid-process (r). Approximately half of the elements heavier than iron are s-process elements (Arlandini et al., 1999), those which are created when the neutron capture rate is slower than the typical decay time scale. AGB stars are the primary source for the s-process elements (Herwig, 2005) and enrich the ISM through stellar winds. The r-process elements are produced in high neutron flux environments when capture reactions occur on a time scale much faster than the decay time. The primary production site of the r-process is currently an active field of study with hypotheses ranging from high energy events such as supernovae (Woosley et al., 1994; Travaglio et al., 2004) to neutron star mergers (Freiburghaus et al., 1999; Tsujimoto & Shigeyama, 2014).

Since both processes can contribute to the production of a particular element, the relative contributions to an elemental abundance from the $s-$ and $r-$ process are often studied as functions of metallicity. As an example, Eu is considered a pure $r-$process element as solar-metallicity stars and the solar system abundance distribution of Eu is explained by 95% r-process contributions and $<$5% of s-process contributions (Burris et al., 2000; Sneden et al., 2008). On the other hand, elements like Sr, Y, Zr, and La show over-abundances at low metallicity, indicating different nucleosynthetic sites at low and high metallicity

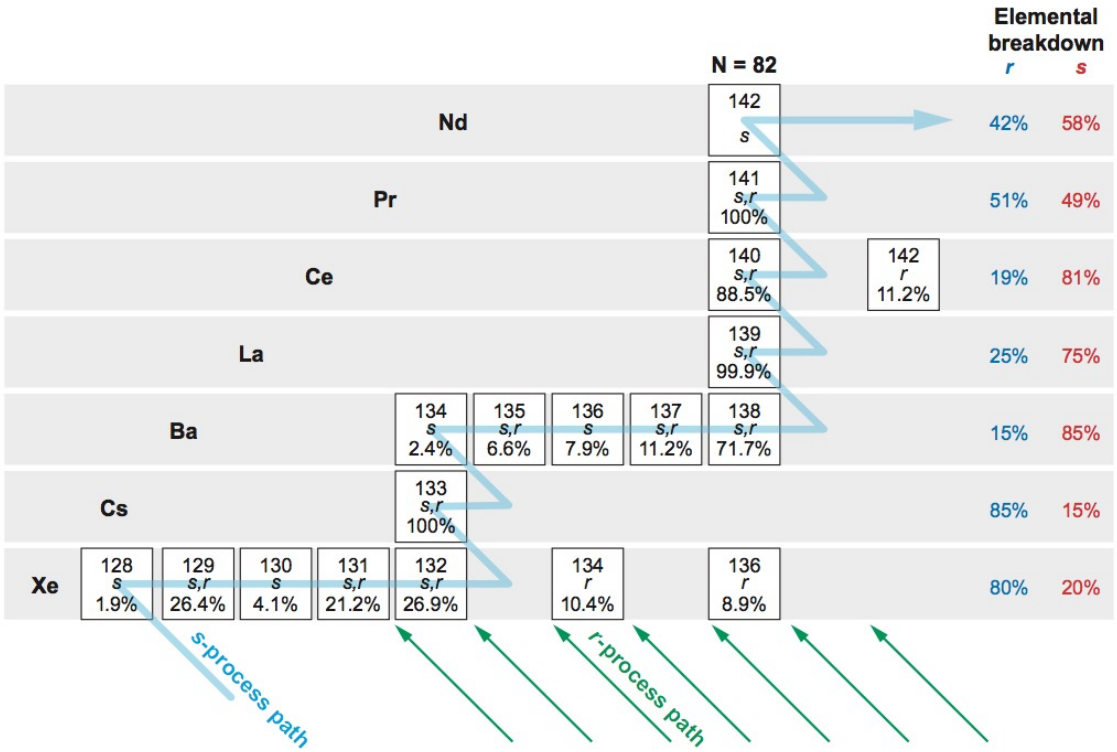

Figure 1.2 Reproduced from Sneden et al. (2008). Schematic of the $s-$ (light blue) and $r-$processes (green) for a portion of the chart of nuclides with relative relative contributions from each process labeled. The s-process follows the valley of stability while the r-process is capable of producing heavier neutron rich isotopes. Only stable isotopes are shown.

(Burris et al., 2000; Travaglio et al., 2004; Venn et al., 2004; François et al., 2007; Sneden et al., 2008). Detailed chemical abundances of stars spanning the full metallicity distribution function are needed to constrain the formation sites for the neutron-capture elements (e.g., Cohen et al., 2004; Norris et al., 2007; Heger & Woosley, 2010; Nomoto et al., 2013; Tominaga et al., 2014; Choplin et al., 2017; Côté et al., 2017)

It is through the detailed study of the chemical abundance patterns of individual stars and their distribution throughout a galaxy that we may identify the different astrophysical sources, time scales, and enrichment processes responsible for production of the elements.

1.1.2 Chemical Evolution and Chemical Tagging

The first stars in the Universe, Population III stars, formed from the pristine, metal-free gas that existed after the Big Bang. These stars evolved, formed heavier elements through the aforementioned nucleosynthetic pathways, and dispersed these new elements into their environments through supernovae and stellar winds. Subsequent generations of stars formed from this "enriched" material and continued the process of metal enrichment of the Universe, producing new generations of stars which are increasingly metal-rich.

The Universe however does not have a homogeneous chemical distribution because the distribution of stars is inhomogeneous. Most stars are locked into structures like galaxies and dwarf galaxies which themselves have finer stellar substructures which may experience their own evolutionary paths. As a result, each stellar substructure may have a chemical fingerprint as unique as the next depending on structure characteristics such as stellar mass, dark matter halo mass, luminosity, the assumed initial mass function of the stellar population, star formation history, and star formation efficiency (Freeman & Bland-Hawthorn, 2002; Tolstoy et al., 2009). Thus, detailed chemical abundance maps of these systems, particularly for elements sensitive to well defined pathways, allow for us to not only probe the astrophysical processes responsible for the formation of the elements themselves but the formation processes of the structures as a whole.

Initially recognized by Tinsley (1979) the ratio of α-elements to Fe (typically expressed as [α/Fe], the logarithmic ratio relative to the Sun) can provide insight on the relative contributions of SNe Type Ia and Type II in a system. SNe Type II occur

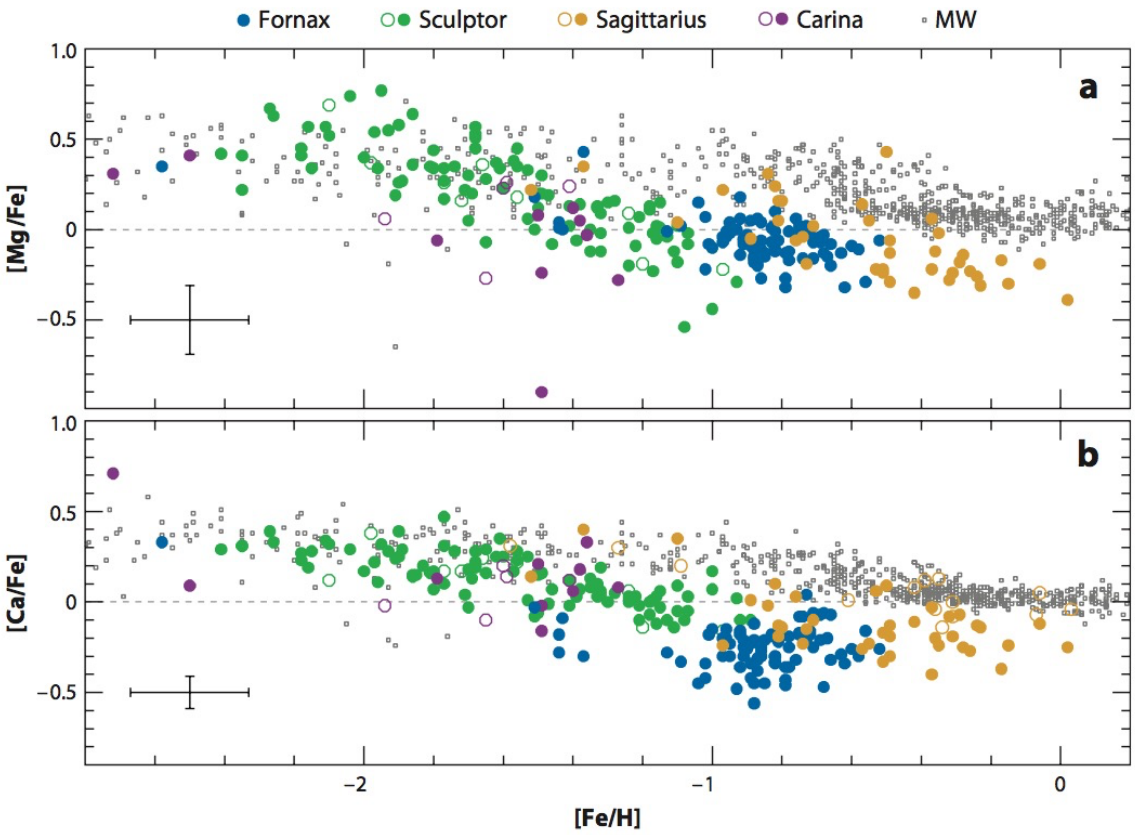

Figure 1.3 Mg and Ca abundance ratios for nearby dwarf galaxies (coloured points) and the Milky Way (grey circles), adopted from Tolstoy et al. (2009). Mg and Ca serve as proxies for the overall α abundance; representative error bars are shown.

in young systems as their short-lived, high mass progenitors quickly burn their way to through the MS and to later evolutionary phases. These events produce both α-elements and Fe, holding [α/Fe] roughly constant. It has been observed in the Milky Way and the dwarf galaxy satellites that SNe Type II contributions fix [α/Fe]$\sim +0.4$ (McWilliam et al., 1995; Gratton et al., 2000; Tolstoy et al., 2009; Mashonkina et al., 2017). On larger time scales, lower mass stars will evolve to the white dwarf phase of evolution and SNe Type Ia will begin to contribute to the environment. Since the SNe Type Ia produce Fe but minute amounts α-elements, the [α/Fe] ratio decreases with [Fe/H], producing a "knee" in a plot of [α/Fe] vs. [Fe/H].

Since the location of this "knee" is sensitive to when contributions from SNe Type Ia become significant over Type II, the "knee" must also be sensitive to star formation history and efficiency of a system. Dwarf galaxies have lower star formation efficiencies than larger systems meaning SNe Type II will enrich these systems to lower [Fe/H]

than observed in the Milky Way (Tolstoy et al., 2009; Venn et al., 2004). Figure 1.3, adopted from Tolstoy et al. (2009), shows the [α/Fe] ratios for stars in nearby dwarf galaxies and in the Milky Way highlighting this effect.

Discussed further in Chapter 2.6.3, low α-ratios, where [α/Fe]< 0, are additionally observed in the dwarf galaxies but not in the Milky Way. Due to an extended star formation history, SNe Type II still occur in the Milky Way contributing new α-elements to the ISM and preventing the [α/Fe] ratio from falling much below 0 dex. Conversely, the short star formation histories in the dwarf galaxies ($< 1Gyr$ Tolstoy et al., 2009), coupled with top-light initial mass functions (IMF) (i.e., few contributions from stars over $20M_{\odot}$), as suggested by Hasselquist et al. (2017), not only result in SNe Type Ia at earlier times than in the higher mass systems (Salvadori & Ferrara, 2009), driving [α/Fe] down at lower metallicity, but the lack of SNe Type II at later times permits [α/Fe]< 0. Thus, α-challenged stars found in the Milky Way are unlikely to have formed in situ, but their discovery may serve as tracers of dwarf galaxies accreted by the Milky Way.

1.2 Stellar Spectroscopy

Understanding the chemistry of stars is vital in understanding the evolution of the elements in the Galaxy as well as the evolution of galaxies as a whole. To decipher the chemical abundances imprinted onto stellar atmospheres, techniques have been developed to decompose the light we collect with telescopes. Utilizing photometry alone, stellar metallicities can be estimated (Da Costa & Armandroff, 1990; Ramírez & Meléndez, 2005; Casagrande et al., 2010; Starkenburg et al., 2017) however spectroscopy is needed to determine precise chemical abundances.

Considering we can only probe the optically thin layers of a stellar atmosphere, we are observing light which has been produced by a blackbody and has been scattered and absorbed by the outer layers of the stellar atmosphere. The electrons, atoms, and molecules present in the stellar atmosphere will absorb light from the underlying blackbody, producing dark absorption lines in an otherwise continuous spectrum. Based on the electronic structure of the present atoms and the rotational and vibrational modes of any molecules, the wavelength of light absorbed by each element will differ producing a unique spectral fingerprint for every element. Increasing the number of atoms in an atmosphere, i.e. increasing the chemical abundance, increases the number of absorbers, thus increasing the strength of absorption, when all other

parameters are kept fixed, and darkening spectral lines though a relationship known as the Curve of Growth (Böhm-Vitense, 1989).

The stellar parameters, primarily the stellar surface temperature, are dominating factors in the profile of spectral absorption lines, however the abundance of a particular element also influence the line structure. When using stellar model atmospheres in conjunction with radiative transfer codes such as MOOG[1] to determine chemical abundances, the physical properties of interest are effective temperature T_{eff}, surface gravity $\log g$, microturbulent velocity ξ and the iron metallicity [Fe/H].

1.2.1 Effective temperature T_{eff}

The effective temperature of a star, T_{eff}, is related to the blackbody temperature at the surface of the stellar photosphere, but is more precisely defined by the optical depth of the layer where the continuum forms, which is wavelength dependent, under the assumption of local thermodynamic equilibrium (LTE). Determination of T_{eff} is possible spectroscopically by balancing the excitation potential of individual lines, which form just above the continuum, when equivalent widths (EWs)[2] can be measured or through empirical relations like the Infrared flux method (IRFM) when photometric colors and metallicities are known (Blackwell et al., 1979; Alonso et al., 1999; Ramírez & Meléndez, 2005; Casagrande et al., 2010). The effective temperatures reported in this thesis come from the IRFM unless otherwise stated.

1.2.2 Surface gravity $\log g$

The surface gravity is defined as $\log g = \log(GM/R^2)$ where M is the stellar mass and R is its radius. Measured spectroscopically by requiring the abundance derived from two ionization states of the same element, i.e. Fe I and Fe II, to be the same, surface gravity $\log g$ provides information on the gas and electron pressure in the stellar atmosphere. Denser stars have higher surface gravities which translates to increased pressure broadening of spectral lines as van der Waals forces and dipole coupling become stronger. This pressure affects the radiative transfer processes in the stellar atmosphere, ultimately governing line formation, and is sensitive to deviations from local thermodynamic equilibrium (LTE). Non-LTE effects are expressed

[1] MOOG was originally written by Chris Sneden (1973), and has been updated and maintained, with the current versions available at http://www.as.utexas.edu/ chris/moog.html.

[2] Equivalent width of a spectral line is the width of a characteristic rectangle with an area equal to the area contained by a spectral line and the continuum level

differently in various ionization states and even in different absorption lines of a particular element, with deviations in the derived chemical abundance reaching up to ± 1 dex (Mashonkina et al., 2017). This thesis assumes LTE, however this assumption should be investigated in later works as non-LTE effects are expected and observed when determining chemical abundances from RGB stars. Surface gravity may also be derived empirically if the distance to a star is known through a relationship between stellar mass, T_{eff}, and absolute bolometric magnitude. A commonly adopted metric from (Alonso et al., 1999) is given as:

$$\log g = 4.44 + \log(mass) + 4 \log 10(T_{eff}/5790) + 0.4(m_{bol} - 4.75)$$

1.2.3 Microturbulent velocity ξ

Microturbulent velocity ξ refers to the small scale surface convection features which affect gas velocities in line forming regions in a stellar atmosphere. The effect is seen through small Doppler shifts of spectral lines which will broaden the EW, resulting in a higher than expected measurement for the chemical abundance derived from the absorption line in question. By forcing the abundances measured from multiple spectral lines of the same element to be independent of line strength (EW), ξ can be determined. ξ is thought to be strongly degenerate with $\log g$ which often results in empirical scaling relations between the two. In this thesis, APOGEE stellar parameters are often utilized where ξ is derived through such scaling relations. Using a calibration sample of stars with known ξ and $\log g$ from optical analyses of Galactic red giants, (García Pérez et al., 2015) derives a scaling relation as follows:

$$\log \xi = 0.225 - 0.0228 \log g + 0.0297 (\log g)^2 - 0.0113 (\log g)^3$$

1.2.4 Metallicity [Fe/H]

The metallicity of a star is critical in understanding the stellar atmosphere as metal absorption lines strongly affect the opacity and radiative transfer processes. [Fe/H], the logarithmic ratio of the star's Fe abundance relative to the Sun, serves as a proxy for the overall metallicity and serves as a scaling point when comparing the abundances of other elements to the Sun. [Fe/H] may be determined through EW measurements or through a synthetic spectrum analysis, described in the next section.

1.2.5 Line lists

Line lists are compilations of atomic data relevant to stellar atmosphere models when simulating the strength of an absorption line. Typically, a line list will contain the species identifier, the expected wavelength at which the line will form, the line excitation potential, the oscillator strength, which describes the electronic transition probability, the van der Waals dampening factor, the dissociation energy for molecular features, and the equivalent width of a line, if measured. A "clean" line list will only contain lines with reliable atomic data that are strong enough to be measured given the signal-to-noise ratio (SNR) of the spectra at hand, lines that are not subject to blends from nearby strong lines or molecular bands, and should contain enough lines for a given species to determine a reliable abundance measurement. Unfortunately, some elements do not produce spectral lines in a given wavelength regime, such as B, Be, and P in optical wavelengths, prohibiting the determination of a chemical abundance.

1.3 Determination of Chemical Abundances

1.3.1 EW and Synthetic Spectra Analyses

Presently there are two primary methods of determining chemical abundances from stellar spectra: an EW analyses and synthetic spectra analyses. EW measurements are typically easy to make assuming absorption lines are not saturated, subject to strong Lorentzian wings, have a well defined continuum, and are free of blends from other elements or molecular bands. Combined with accurate atomic data from a line list and radiative transfer codes, EW may be directly converted to chemical abundances.

In Chapter 2, chemical abundances are derived using synthetic spectra syntheses. IR spectra probe the cooler layers of the stellar atmosphere and are subject to strong molecular bands and blends. Coupled with low SNR and poor continuum placement, an EW analysis would be inappropriate for determining chemical abundances in the IR. Using previously determined stellar parameters, synthetic spectra may be generated from stellar atmosphere models and may be degraded to the resolution of the measured spectra. By producing a grid of synthetic spectra which spans a range of abundances for a particular element, the best fit model to the measured data can be found, yielding the abundance for the element being measured. Assuming the atomic

data from the line list is reliable, this method can account for molecular blending and simulates the complete line profile, rather than estimating an EW, which is favourable when working with IR spectra.

1.4 Thesis Outline

This thesis explores new territories in the field of stellar archaeology. Chapter 2 investigates Data Release 12 from the APOGEE spectroscopic survey, analyses six new carbon-enhanced metal-poor (CEMP) star candidates found within the database, and serves as the first exploration of CEMP stars using H-band spectra. Chapter 3 highlights the first results from the spectroscopic follow-up programme of the *Pristine* survey and presents an innovative spectral analysis technique using deep neural networks, pioneering the analysis of future spectroscopic surveys.

Chapter 2

Carbon-enhanced metal-poor stars in the SDSS-APOGEE database

The following chapter has been adopted from the work of ***C. Kielty, K. A. Venn, N. B. Loewen, M. D. Shetrone, V. M. Placco, F. Jahandar, Sz. Mészáros, and S. L. Martell***

Published in MNRAS as Kielty et al. 2017

2.1 Abstract

We identify six new CEMP stars ([C/Fe]$>$ +0.7 and [Fe/H]$<$ −1.8) and another seven likely candidates within the APOGEE database following Data Release 12. These stars have chemical compositions typical of metal-poor halo stars, e.g., mean [α/Fe] = +0.24±0.24, based on the ASPCAP pipeline results. A lack of heavy element spectral lines impedes further sub-classification of these CEMP stars, however, based on radial velocity scatter, we predict most are not CEMP-*s* stars which are typically found in binary systems. Only one object, 2M15312547+4220551, may be in a binary since it exhibits a scatter in its radial velocity of 1.7 ± 0.6 km s^{-1} based on three visits over a 25.98 day baseline. Optical observations are now necessary to confirm the stellar parameters and low metallicities of these stars, to determine the heavy-element abundance ratios and improve the precision in the derived abundances, and to examine their CEMP sub-classifications.

2.2 Introduction

The arrival of large multi-object spectroscopic surveys in the past decade has accelerated the fields of stellar archaeology and near-field cosmology by providing homogeneous and precise stellar parameters and abundances for $\sim 10^5$ stars in all structural components of the Galaxy. With such large data samples and using stellar chemical abundance profiling, it is possible to probe the primary astrophysical processes responsible for early star formation, and gain insight into Galactic formation and evolution.

An early endeavour into large scale spectroscopic surveys includes the RAdial Velocity Experiment (RAVE; Steinmetz et al. (2006)). RAVE collected $R \sim 7000$ spectra, measured radial velocities and proper motions accurate to 1.5 km/s using the Calcium triplet, and determined stellar parameters and elemental abundances (Mg, Al, Si, Ca, Ti, Fe, and Ni) for $\sim 480,000$ stars with $8 < I < 12$ (Boeche et al., 2011). From this dataset, new constraints have been placed on the Galactic mass and escape velocity (Smith et al., 2007; Piffl et al., 2014b,a), the Aquarius tidal stream has been discovered (Williams et al., 2011; Wylie-de Boer et al., 2012), tidal debris around globular clusters have been identified and characterized (Kunder et al., 2014; Anguiano et al., 2015; Fernández-Trincado et al., 2015), and a plethora of studies on Galactic disc kinematics and chemical gradients have been carried out (Ruchti et al., 2010, 2011; Wilson et al., 2011; Boeche et al., 2013a,b; Williams et al., 2013; Binney et al., 2014; Boeche et al., 2014).

Exploring down to $g \geq 20$ magnitude, the SDSS/SEGUE survey (Abazajian et al., 2009; Yanny et al., 2009b) collected $R \sim 2000$ optical (3850-9200 Å) spectra for $\sim 300,000$ stars with the intent of mapping the kinematics and stellar populations of the Milky Way. The depth of the SEGUE survey has allowed for the kinematic characterization of the Galaxy (Smith et al., 2009; Carollo et al., 2010; Bond et al., 2010; Gómez et al., 2012; Bovy et al., 2012a,b), the discovery and characterization of faint substructures within the Galaxy, namely the Orphan and Sagittarius streams as well as the Segue 1 and 2 satellites, (Belokurov et al., 2007; Klement et al., 2009; Yanny et al., 2009a; Belokurov et al., 2009; Newberg et al., 2010), and the investigation of chemistry within these structures, including the discovery of chemically peculiar stars (An et al., 2009; Norris et al., 2010b,a; Martell & Grebel, 2010; Aoki et al., 2010; Simon et al., 2011; Lee et al., 2011b, 2013; Schlesinger et al., 2012; Santucci et al., 2015; Lee et al., 2017). Modern surveys such as Gaia-ESO (Gilmore et al.,

2012a), GALAH (De Silva et al., 2015), and APOGEE (Majewski et al., 2015) will critically increase the quality and depth of our understanding of the Galaxy with higher resolution, larger sample sizes, and high precision measurements.

Complimentary to these large spectroscopic surveys are more targeted surveys of metal-poor stars. McWilliam et al. (1995), Aoki et al. (2007), Yong et al. (2013a), Norris et al. (2013), and Lee et al. (2013) which have shown the presence of a large metal-poor population in the stellar halo. Within this population of metal-poor stars, a significant fraction of stars with abundance anomalies have been found. Of particular interest in the chemically peculiar star group are those with carbon-enhancement (CEMP stars; Beers & Christlieb, 2005) which represent 20% of stars with [Fe/H]< -2.0 and with a rapidly increasing fraction at lower metallicities, approaching unity for known stars with [Fe/H] < -4.5 (Christlieb, 2003; Lucatello et al., 2005; Frebel et al., 2006; Carollo et al., 2012; Aoki et al., 2013a; Lee et al., 2013; Norris et al., 2013; Yong et al., 2013a; Placco et al., 2014; Hansen et al., 2016b).

CEMP stars have been the focus of a large number of recent studies due to their importance in identifying rare processes in the context of Galactic chemical evolution. Within the population of CEMP stars several subclasses exist, defined by ratios of neutron-capture elements in the stellar spectra: CEMP-s, CEMP-r, CEMP-r/s (or CEMP-i), and CEMP-no. Each of these subtypes are described below.

The CEMP-s stars (those with slow neutron-capture, s-process, element enrichment) are proposed to be the metal-poor analogues to the Ba II, classical CH, and subgiant CH stars, based on similar abundance patterns (Preston & Sneden, 2001; Sneden et al., 2003). Likewise, CH stars demonstrate a binary frequency "consistent with unity" (McClure & Woodsworth, 1990), an observational trend shared by CEMP-s stars as shown by Lucatello et al. (2005); Starkenburg et al. (2014); Hansen et al. (2016c). The peculiar abundance patterns seen in CH stars, combined with the high observed binary fraction are indicative of the accretion of material from an intermediate-mass AGB companion, either through Roche lobe overflow or through efficient stellar winds (Han et al., 1995). The latter scenario is more likely as a result of the instability of the Roche lobe in thermally pulsing AGB stars and the typically larger spatial separations of these binary systems (Paczyński, 1965; Abate et al., 2013). Similarly, Herwig (2005); Placco et al. (2013); Hansen et al. (2016a) have shown the abundance profiles of the CEMP-s stars are consistent with enrichment from an AGB companion. The difference between these similarly natured objects currently exists only in an arbitrary cut in metallicity. An upper limit of [Fe/H]< -1.8 is

described by Lucatello et al. (2005) to separate CEMP-s stars from the more metal-rich classical Ba II, CH, and subgiant CH stars. The most metal-poor CH stars have been observed down to [Fe/H]~ -1.5 (Vanture, 1992; Goswami, 2005), and the Lucatello et al. (2005) cut seeks to establish a factor of two difference in metallicity between these systems.

CEMP-r/s stars show an enrichment of rapid neutron-capture, r-process, elements as well as elements from the s-process. The origins of these stars are currently under investigation with theories ranging from the formation of a CEMP-s star via AGB companion mass transfer in an environment previously enriched with r-process materials (Jonsell et al., 2006) to stars influenced by the intermediate neutron-capture, i-process, which may occur in a range of stellar sites (Roederer et al., 2014b; Dardelet et al., 2015; Hampel et al., 2016).

CEMP-no stars (those with no n-capture enrichments) are potentially the most informative in the context of Galactic chemical evolution since they do not appear to be closely linked with binary systems, opening doors to other carbon-enrichment mechanisms beyond mass transfer. Meynet et al. (2006); Maeder et al. (2015) have proposed fast rotating metal-poor "spinstars" experience partial mixing processes that bring CNO materials to the stellar surface. Through stellar winds, their local ISM becomes enriched with these elements and the later generations of stars to form in these regions would exhibit CEMP abundance profiles. C-enhancement of the ISM via Population III faint supernovae has also been modelled in detail by Umeda & Nomoto (2003); Umeda et al. (2006); Heger & Woosley (2010); Tominaga et al. (2014), who have shown that fined tuned levels of mixing and fallback during the supernova can result in abundance profiles consistent with those seen in the CEMP-no stars. Regardless of the exact mechanism(s) responsible for the abundances seen in CEMP-no stars, it appears these old objects may reflect the nucleosynthetic enrichment processes present in the early Universe.

Recent studies have shown that distribution of absolute C abundance A(C)= $\log \epsilon$(C) for CEMP stars splits into at least two distinct 'bands' based on their evolutionary history (Spite et al., 2013; Bonifacio et al., 2015; Hansen et al., 2015; Yoon et al., 2016). Yoon et al. (2016) identifies peaks in the A(C) distribution at A(C)=7.96 and A(C)=6.28, corresponding to the high-C and low-C regions respectively. They argue the separation of these two bands serves as an effective and astrophysically motivated metric in assessing the history, nature, and sub-class of CEMP stars, as the vast majority of known CEMP-s/rs stars are highly concentrated around the

high-C band while known CEMP-no stars are scattered around the low-C band. This separation allows for a preliminary classification of CEMP stars based solely on their A(C), rather than on the abundance ratios of neutron-capture elements. Yoon et al. (2016) successfully classified 87% (139 of 159) of the CEMP-s/rs stars and 93% (104/112) of the CEMP-no in their sample using only A(C), and treating the traditional [Ba/Fe] criterion as the standard. Additionally, Yoon et al. (2016) observe the known and likely binaries in their sample separate around the midpoint in the distribution at $A(\mathrm{C}) = 7.1$, further supporting extrinsic origins of carbon enhancement in the CEMP-s/rs stars and intrinsic origins for CEMP-no stars. An understanding of the CEMP stars may prove critical in unlocking knowledge on early Galactic astrophysical processes, pristine stellar populations, and would assist in completing the picture of Galactic evolution.

CEMP stars have been found serendipitously in spectroscopic surveys. Often, low resolution spectroscopy focused on the carbon sensitive G-band and metallicity sensitive CaII K feature in the optical is used to identify CEMP candidates (see the Hamburg/ESO (HES) survey (Christlieb et al., 2001; Rossi et al., 2005; Placco et al., 2010, 2011)). High resolution spectroscopic follow up is then used as confirmation on the nature of these stars.

Playing off large sample size statistics, the APOGEE database may serve as a useful tool in the search for these rare objects and provide us with new candidates for follow-up optical spectra. In this paper we explore the APOGEE database for new CEMP stars. In Section 2 we summarize the key elements of the APOGEE survey and the selection of our CEMP candidates, Section 3 explores the ASPCAP abundances of our candidates in detail, independent abundances are derived and cross checked in Section 4, and our discussion, concluding remarks and perspectives are gathered in sections 5 and 6.

2.3 The APOGEE Spectroscopic Survey

The APOGEE survey of the the Sloan Digital Sky Survey, SDSS-III Data Release 12 (Eisenstein et al., 2011; Alam et al., 2015) provides high resolution ($R \backsim 22,500$) IR (H-band) spectra for $\backsim$150,000 targets and derives chemical abundances for 15 elements: C, N, O, Na, Mg, Al, Si, S, K, Ca, Ti, V, Mn, Fe, and Ni using the APOGEE Stellar Parameters and Chemical Abundances Pipeline (ASPCAP; García Pérez et al., 2015). Recent studies such as the colour-T_{eff}-[M/H] relationship for cool

dwarfs (Schmidt et al., 2016), the separation, in chemical abundance space, of stellar populations and structures within the Galaxy (Bovy et al., 2016), and the discovery of halo stars with globular cluster origins via chemical tagging (Martell et al., 2016), are only now probing the surface of this rich datasets' resourcefulness. Halo fields comprise ∼25% of the total sample (Zasowski et al., 2013) making APOGEE a great resource to map chemical abundances in the metal-poor regions of the Galaxy and to search for previously unobserved CEMP stars.

Since the classification of VMP and CEMP stars is dependent solely on metallicity and [C/Fe], it is important to address the distinction between [M/H] and [Fe/H] in APOGEE. While ASPCAP can return [Fe/H] for an object, the primary derived metallicity is given as [M/H]. This overall metal abundance is scaled to the solar abundance pattern through spectral template fitting, and is derived by tracking all metals over the entire wavelength regime of the APOGEE spectrograph. By comparing the derived [M/H] metallicity of well studied clusters to the spectroscopic metallicity found in the literature, the metallicity scale was calibrated to a [Fe/H] scale (Mészáros et al., 2013; Zamora et al., 2015; Holtzman et al., 2015).

Holtzman et al. (2015) found that a difference of ∼0.2 dex between the calibrated [Fe/H] and [M/H] is seen below [M/H]=−1.0, with the discrepancy increasing as a function of decreasing metallicity, reaching $\simeq$ 0.3 dex around [M/H]= −2.0 (see their Figure 6). The ASPCAP output is limited to metallicities [M/H]> −2.4 as the Fe lines become too weak to measure at lower metallicity in infrared spectra. Stars more metal-poor than this could still be present in the survey, but ASPCAP would either return [M/H] = −2.4 (a proxy for an upper limit); alternatively, it may report the star as hotter, since RGB spectral lines would be weaker, or chemically peculiar. This restriction on metallicity, coupled with the higher associated errors in the metal-poor regime, have motivated a majority of the previous APOGEE-based studies to restrict the analysis to near-solar metallicity stars. This paper serves as a step into the metal-poor regime.

2.3.1 Uncertainties in the ASPCAP Abundances

The APOGEE team has identified issues driving uncertainty in the ASPCAP stellar parameters and abundances. Other than the known persistence problem (see Section 2.3.2), the spectral quality itself is not a significant source of uncertainty since APOGEE targets are reobserved multiple time until a $SNR > 100$ is attained in the

combined spectrum for each object. A complete discussion of the calibration process and uncertainties can be found in Mészáros et al. (2013); Nidever et al. (2015); Holtzman et al. (2015), and we highlight the issues relevant to metal-poor stars below.

The primary metallicity uncertainty in the ASPCAP output is found at low metallicity, which can be seen in the data calibration to open and globular clusters. Holtzman et al. (2015) used literature data on 20 open and globular clusters to calibrate $T_{\rm eff}, \log g$, metallicity, α, C and N for the APOGEE DR12 data. For [M/H] metallicities < -1.0, the difficulty of detecting Fe lines in IR spectra results in systematic differences between the ASPCAP results and the literature of up to 0.2 dex (see their Figure 6). This effect additionally increases with temperature as spectral lines weaken.

Mészáros et al. (2013) also examined the large errors in abundances in metal-poor stars due to the impact of molecular bands (C, N, and O particularly) in the metal-poor stars. These errors stem from the reduced number of spectral features at low metallicity and a relatively strong dependence of the line strength on the stellar parameters, particularly $T_{\rm eff}$. Additionally, a calibration of ASPCAP derived [C/Fe], [N/Fe] and [O/Fe] to literature values for globular cluster stars cannot be generally applied, since globular clusters have prominent star-to-star variations in light element abundances that are not common in the field (Holtzman et al., 2015).

CEMP stars present an intriguing challenge for ASPCAP. A CEMP star with [Fe/H]< -2.5 and [C/Fe]$> +1.0$ is near the limits of the APOGEE synthetic spectral library, and so the best-fit values for the stellar parameters can be rather different than if the analysis pipeline were able to further adjust the abundances of Fe and C. As an example, the derived $T_{\rm eff}$ may be artificially high to reproduce weak Fe lines in the observed spectrum when the true [Fe/H] is lower than allowed by the synthetic library.

In Figure 2.1, we show the ASPCAP [C/Fe] vs. $T_{\rm eff}$ and [Fe/H]. Stars with metallicities near solar ([Fe/H]$\gtrsim -0.5$) are well clustered around solar [C/Fe] and do not display any temperature dependence beyond a higher degree of scatter for $T_{\rm eff} \gtrsim 4700$ K, as expected based on the the aforementioned uncertainties in the spectral analysis. The lower metallicity stars ([Fe/H] < -1.5), however, show a very clear trend between [C/Fe] and $T_{\rm eff}$, indicating that carbon abundances are unreliable in metal-poor giants. This relationship is the combined result of the temperature sensitivity of CO molecular bands, continuum placement effects, and upper-limit abundances derived from weak lines. Upper-limit abundances are not identified or flagged by ASPCAP,

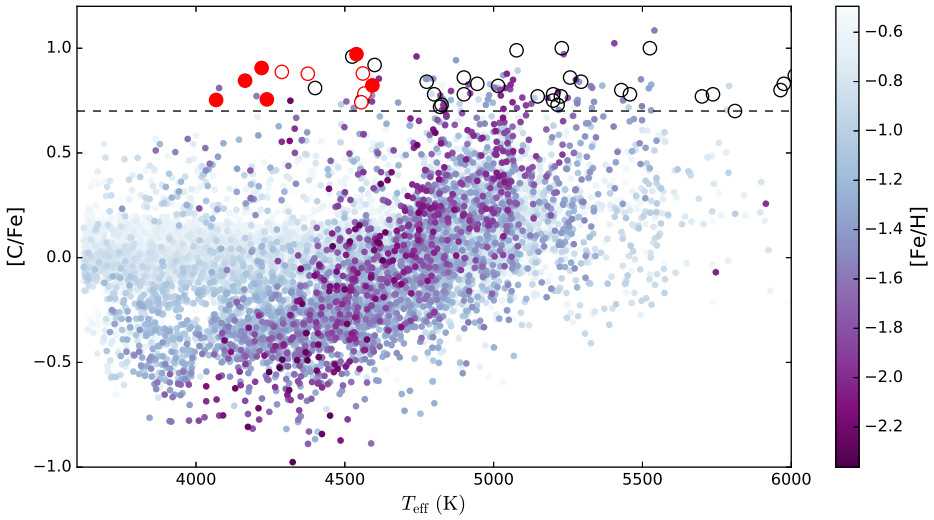

Figure 2.1 The relationship between [C/Fe] and $T_{\rm eff}$ for all metal-poor ([Fe/H< -0.5) APOGEE stars, coloured by metallicity. Filled red circles are our Group A CEMP candidates, open red circles are Group B (see Section 2.3.2 for the distinction between Group A and B) and open black circles are known CEMP stars selected from Placco et al. (2014). Stars with [Fe/H]< -1.5 demonstrate a very clear trend between [C/Fe] and $T_{\rm eff}$ suggesting a correlation between [C/Fe] and $T_{\rm eff}$. This relationship is non-physical and likely the combined result of the double-metal CO molecular bands temperature sensitivity and the inclusion of upper-limit abundances derived from weak lines.

requiring one to examine the ASPCAP spectrum and synthetic fit manually. The issue of upper-limits for the warmer stars is displayed in Figure 2.2. Three stars with similar [C/Fe] and [Fe/H], but varying $T_{\rm eff}$ were selected from APOGEE to examine the relationship between the atomic C I line strength and $T_{\rm eff}$. The atomic C I line at 16895 Å provides one of the most reliable estimates for the C abundance in the H-band (see Section 2.5.3), and thus the quality of the model fit to this feature is a critical test of the C abundance. Despite similar [Fe/H], [C/Fe], and S/N, the atomic C I line becomes indistinguishable from the noise in the spectra of stars with $T_{\rm eff} \gtrsim 4800$ K. Consequently, C abundances derived for warmer stars should be treated as upper limits, diminishing the likelihood these stars are actually carbon-enhanced. The cooler, C-poor, metal-poor stars in Figure 2.1 may be subject to similar systematic bias. In summary, low metallicity stars at both high $T_{\rm eff}$ - high [C/Fe] and low $T_{\rm eff}$ - low [C/Fe] in the APOGEE DR12 database are subject to systematics that have not been accounted for and should be handled with caution.

Previous CEMP studies often impose a selection of $T_{\rm eff} > 4800$ K, as well as $\log g \geq 1.3$. This minimizes the possibility the selected stellar sample is contaminated by cooler AGB stars, which can have very similar surface abundance profiles to CEMP stars as the result of the third dredge-up (Lucatello et al., 2005). The inclusion of previously known CEMP stars (selected from Placco et al. (2014)) in Figure 2.1 highlight this selection of CEMP stars at higher $T_{\rm eff}$, indicating that the DR12 ASPCAP abundances are not ideal for detecting the warmer CEMP stars that are typically studied in the literature, and may be biased towards cooler AGB contaminants.

2.3.2 Selected Sample from the APOGEE Database

Our sample in Figure 2.1 was collected from the SDSS Sky Server by querying all APOGEE objects with no bad data flags. Guided by the offset between [M/H] and [Fe/H] at low metallicity, and for transparency with previous studies, we adopt the calibrated [Fe/H] (`aspcapStar.fe_h`) rather than [M/H] for the remainder of the discussion. We impose an upper limit of [Fe/H]< -1.8 to our sample following Lucatello et al. (2005), reducing the complete APOGEE to 425 metal-poor candidates.

In DR12, the reported abundances for a particular species X is given as the logarithmic ratio [X/H]. Again for transparency, [X/Fe] abundances were calculated and the errors on [X/H] and [Fe/H] added in quadrature to estimate σ[X/Fe]. Without

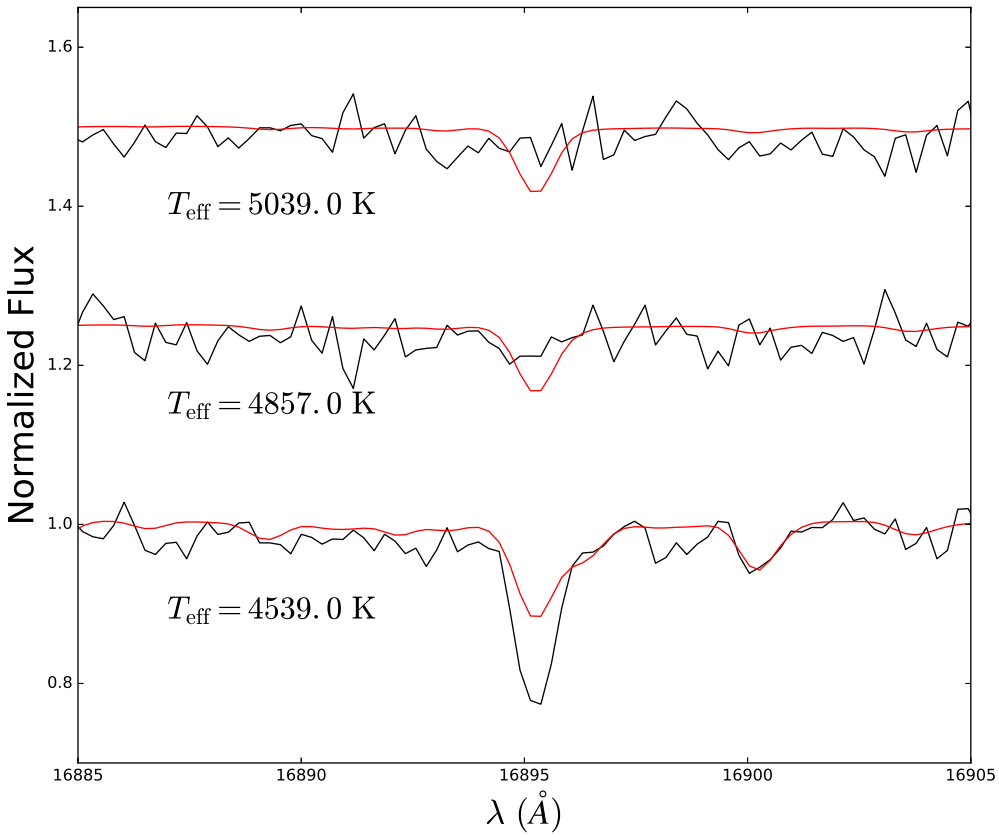

Figure 2.2 Sample APOGEE combined spectra (black) and ASPCAP synthetic spectra (red), centred on the atomic C I line, for three stars (2M21295801+1214260, 2M14442263+1350570, and 2M16300629-1252459; top to bottom) with [Fe/H]~ -1.95, [C/Fe]$\sim +0.8$, and $S/N \sim 100$, but varying $T_{\rm eff}$. The atomic C I line is not visible for metal-poor stars with $T_{\rm eff} > 4600$K indicating the reported C abundance by APOGEE should be treated as an upper-limit for these warmer objects. The poor synthetic fit of the atomic C I line in 2M16300629-1252459 suggests a higher than reported C abundance for this star.

exception and following similar arguments for Fe, [C/Fe] was calculated from [C/H] and [Fe/H], rather than directly adopting [C/M]. Applying the definition of carbon-enhancement as [C/Fe] >= +0.7 (Aoki et al., 2007), the sample was further reduced to 37 CEMP candidates.

Motivated by the observed trend in [C/Fe] vs. $T_{\rm eff}$ at low metallicity and the presence of the atomic C I line in the lower temperature stars, we reject the suggested Lucatello et al. (2005) selection cuts of $T_{\rm eff} \geq 4800$K and $\log g \geq 1.3$ and only select stars with $T_{\rm eff} \leq 4600$K and no cut in $\log g$, reducing the sample to 13 stars. These criteria were initially adopted by Lucatello et al. (2005) to minimize AGB contamination in their sample, thus the dismissal of these cuts warrants careful analysis to exclude the selection of AGB stars and is addressed in Section 2.4.1 and 2.6.1. The catalogue of CEMP stars by Placco et al. (2014) contains 15 stars with $T_{\rm eff} < 4800$K and $\log g < 1.3$, indicating CEMP stars with these uncommon stellar parameters have been previously identified.

Amongst the 13 new CEMP candidates, the spectral quality varies significantly. Majewski et al. (2015) and Nidever et al. (2015) have identified distortions in the APOGEE spectra as a result of a persistence effect where the latent charge from a previous exposure remains on the CCD chip. This results in an artificially raised level and is not consistent across all three of the APOGEE chips. Super-persistence affects only the "blue" and "green" detectors and occurs more frequently in the individual visits of fainter targets (we refer the readers to Nidever et al. (2015) for a more thorough discussion). Characterization of persistence is complicated and no attempt to correct the issue was implemented in DR12.

With these systematics in mind, we have carefully examined the individual lines and synthetic spectra from APOGEE in the database for our 13 candidates. Furthermore, DR13 included an attempt to lower the weight of individual visits when persistence is detected. While DR13 is an improvement, careful comparisons with published stars show this issue is not completely resolved (e.g. Jahandar et al., 2017). Due to the very strong signal left over from persistence, stars which suffered from this issue were easily identified. Figure 2.3 highlights this effect, showing sample spectra for stars with no apparent persistence issues, slight persistence and strong persistence issues. Based on these spectral tests, we further separate our sample of 13 CEMP candidates into three subgroups:

- *Group C*: Two stars were identified whose synthetic spectra poorly matched the

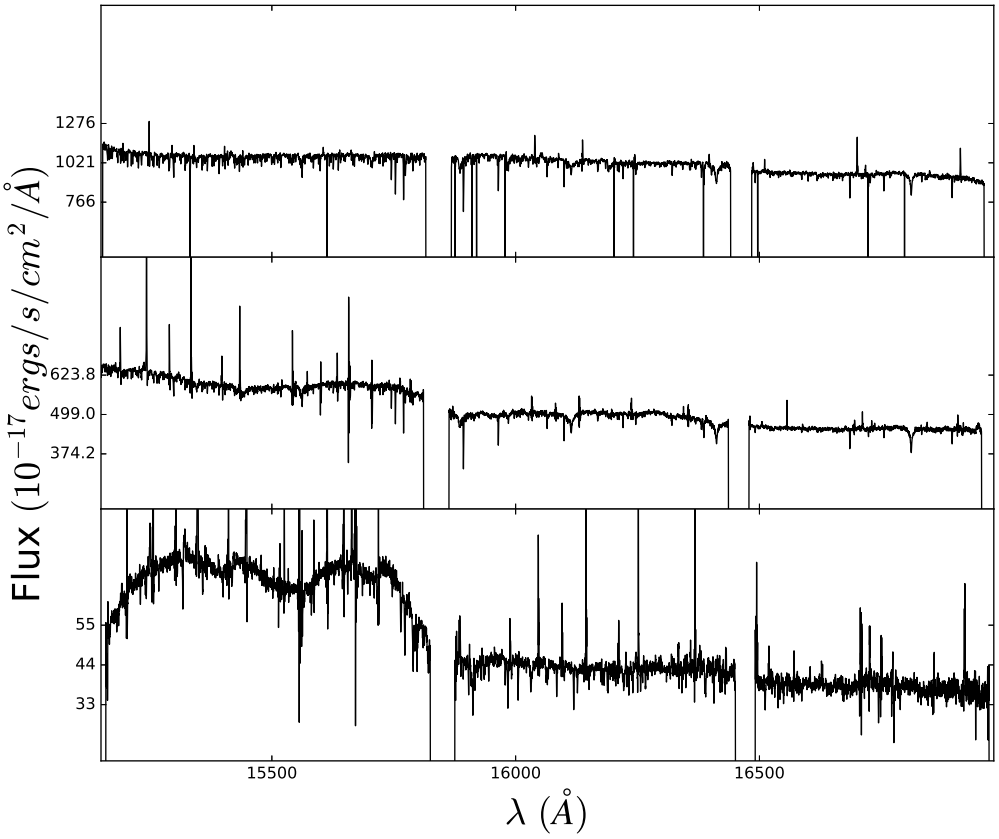

Figure 2.3 Sample APOGEE combined spectra for three objects in our sample. The upper plot shows a Group A spectrum (2M02121851+4923143) with no apparent persistence issues, middle shows a Group B spectrum (2M14010561+2820306) with slight persistence in the blue chip, and the bottom shows a Group C spectrum (2M12473823-0814340) with strong persistence.

combined spectra from APOGEE, identified as Group C in Table 2.1. For this group, persistence or flat fielding issues were a significant issue in the combined spectra and as a result, it is highly unlikely that the stellar parameters and abundances returned by ASPCAP are reliable. These stars will be removed from further discussion.

- *Group B*: Five stars have well-matched synthetic spectra that are sufficiently consistent across the three chips which suggests these are CEMP stars. However, the combined spectra show noise levels, largely in the form of persistence on the blue chip, high enough to raise questions on the reliability of the ASPCAP results. A fresh analysis after removing the spectra affected by persistence is needed for a more precise analysis of these stars. These are the Group B stars in Table 2.1

- *Group A*: The remaining six stars have excellent data, unaffected by persistence. We expect the stellar parameters and ASPCAP chemical analysis to be reliable and thus, we adopt the calibrated stellar parameters $T_{\rm eff}$, $\log g$, [Fe/H] and their corresponding uncertainties from ASPCAP. These stars are Group A in Table 2.1 and the spectra for these objects are shown in Figure 2.4. The discussion below is focused on these stars only.

Table 2.1 List of APOGEE stars with [Fe/H]< -1.8, [C/Fe]$> +0.7$, and $T_{\rm eff} < 4600$K organized by the groups outlined in Section 3.1 and ordered by descending $T_{\rm eff}$. V-band magnitudes adopted from the Zacharias et al. (2005) NOMAD Catalog.

ID	RA (deg)	Dec (deg)	V (mag)	H (mag)	Visits	v_r (km s^{-1})	σ_{v_r} (km s^{-1})	$T_{\rm eff}$ (K)	$\log g$ (dex)	[Fe/H] (dex)	[α/Fe] (dex)	[C/Fe] (dex)
Group A:												
2M15312547+4220551	232.856165	42.348644	15.23	12.71	3	-152.6	1.7	4068	-0.15	-2.08	-0.28	0.75
2M00114258+0109386	2.927455	1.160739	14.3	11.76	3	-154.1	0.1	4165	-0.14	-2.18	0.06	0.84
2M21330683+1209406	323.278461	12.161281	—	12.8	33	-294.2	0.4	4220	0.39	-2.01	0.29	0.91
2M18111704-2352577	272.821009	-23.882698	—	10.46	1	-129.1	—	4238	0.65	-1.82	0.27	0.76
2M16300629-1252459	247.526226	-12.879425	15.67	12.36	6	-296.2	0.6	4539	0.99	-1.95	0.30	0.97
2M02121851+4923143	33.07714	49.387321	13.01	10.11	4	-141.5	0.1	4593	1.61	-1.82	0.44	0.82
Group B:												
2M16334467-1343201	248.43614	-13.72225	13.8	10.18	3	19.4	0.4	4288	0.23	-2.1	0.2	0.89
2M16562103+1002085	254.087657	10.035707	12.61	9.71	4	-149.7	0.3	4376	0.93	-1.98	0.38	0.88
2M11584435+5518120	179.684833	55.303352	14.41	12.03	4	51.9	0.2	4555	1.29	-1.8	0.28	0.74
2M16385680+3635073	249.736697	36.585381	15.35	12.98	13	-317.3	0.7	4561	1.46	-1.84	0.1	0.88
2M14571988+1751501	224.332847	17.863941	13.91	11.32	3	-71.8	0.1	4566	1.35	-1.9	0.19	0.78
Group C:												
2M12473823-0814340	191.909322	-8.242799	15.66	13.56	13	-299.9	10.0	4317	0.79	-2.24	0.67	0.75
2M05352696-0510173	83.862361	-5.171481	—	10.93	4	-184.1	1.5	4591	2.34	-1.9	0.37	0.75

A search through the literature revealed that none of the Group A and B CEMP candidates have been previously identified. As a further test, we searched the complete APOGEE DR12 database for previously known CEMP stars. Stars with 2MASS identifiers in the data sampled from Lucatello et al. (2005) (16 of 19 stars), Aoki et al. (2007) (11 of 26 stars), Placco et al. (2010) (11 of 18 stars), Hansen et al. (2016b) (17 of 24) and Hansen et al. (2016c) (19 of 22 stars) were queried in the APOGEE sample, however none of those 74 objects were found in DR12.

2.4 ASPCAP elemental abundances

2.4.1 Carbon and nitrogen

The C and N abundances for the six Group A stars are presented in Table 2.2. Typical unmixed RGB halo stars with [Fe/H] ~ -2.0 show scaled-solar [C/Fe] and [N/Fe] ratios (Gratton et al., 2000; Cayrel et al., 2004; Aoki et al., 2007). However, all of our Group A stars are C-enhanced and they have super-solar [N/Fe]. The N-enhancements in our stars are consistent with the abundance profiles observed in CEMP stars by Norris et al. (2013) and Hansen et al. (2015, 2016a). Of course, N enhancement in RGB stars is not unique to CEMP stars since mixing on the upper RGB can reduce the surface ^{12}C abundance by a factor of ~ 2.5, decrease ^{12}C/^{13}C to less than 10, and increase [N/Fe] up to $\sim +0.4$ dex (Gratton et al., 2000; Cayrel et al., 2004; Spite et al., 2006; Aoki et al., 2007; Placco et al., 2014). Surface Li can additionally act as a tracer for mixing, however the Li abundance cannot be determined from the APOGEE spectra.

Addressing the possibility of mixing in our sample, Figure 2.5 shows [C/N] as a function of $T_{\rm eff}$ for our Group A stars. Spite et al. (2005) examined the effects of mixing on the evolution of C and N in EMP giants and prescribed a separation between mixed and unmixed stars at [C/N] $= -0.4$. All six Group A candidates lie above this cut at [C/N]$= -0.4$, suggesting the Group A stars are unmixed. However, this implication is unlikely considering all APOGEE targets are on the RGB or AGB where mixing processes and dredge-up are expected. The observation of unmixed abundance ratios, despite the high likelihood of mixing, is a sensible indicator that the natal carbon abundance of these stars was enhanced.

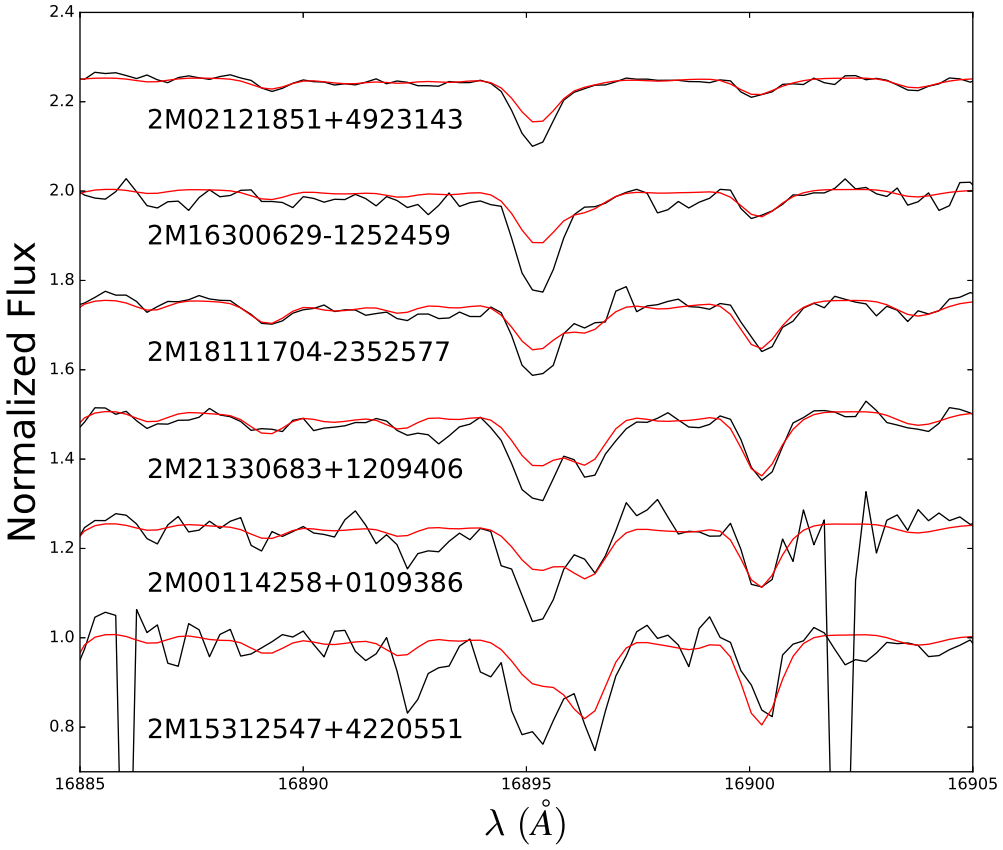

Figure 2.4 The ASPCAP normalized spectra (black) and ASPCAP synthetic spectral fit (red) for the six Group A stars centred around the atomic C I line at 16895 Å. We observe the synthetic fit for all six stars does not accurately reproduce the atomic line suggesting the carbon abundance is higher than reported by APOGEE for these stars

Table 2.2 C and N Abundances for Group A stars as in the ASPCAP database

	2M15312547 +4220551	2M00114258 +0109386	2M21330683 +1209406	2M18111704 -2352577	2M16300629 -1252459	2M02121851 +4923143
$T_{\rm eff}$ (K)	4068 ± 91	4165 ± 91	4220 ± 91	4238 ± 91	4539 ± 91	4593 ± 91
$\log g$	-0.15 ± 0.11	-0.14 ± 0.11	0.39 ± 0.11	0.65 ± 0.11	0.99 ± 0.11	1.61 ± 0.11
[Fe/H]	-2.08 ± 0.06	-2.18 ± 0.06	-2.01 ± 0.06	-1.82 ± 0.06	-1.95 ± 0.06	-1.82 ± 0.06
A(C)	7.18 ± 0.17	7.16 ± 0.19	7.4 ± 0.17	7.44 ± 0.15	7.52 ± 0.21	7.5 ± 0.19
[C/Fe]	0.75 ± 0.17	0.84 ± 0.19	0.91 ± 0.17	0.76 ± 0.15	0.97 ± 0.21	0.82 ± 0.19
A(N)	6.8 ± 0.23	6.73 ± 0.24	6.83 ± 0.22	6.73 ± 0.21	6.85 ± 0.24	6.59 ± 0.22
[N/Fe]	1.02 ± 0.21	1.05 ± 0.22	0.98 ± 0.19	0.68 ± 0.18	0.93 ± 0.21	0.56 ± 0.19
[C+N/Fe]	0.82 ± 0.16	0.89 ± 0.17	0.92 ± 0.16	0.74 ± 0.15	0.96 ± 0.19	0.78 ± 0.19

Further supporting enhanced natal carbon abundances, the four warmer stars exhibit [C/Fe] $\leq$ [N/Fe] and [N/Fe] $>$ +0.4 dex, which is unusual if CNO cycling was the only factor responsible for abundance variation. The two cooler stars, 2M15312547+4220551 and 2M00114258+0109386, have low [C/N] and [N/Fe] $>$ [C/Fe], which, coupled with their low surface temperatures and surface gravities, strongly indicate that they are evolved stars whose current abundances reflect CNO cycling on the upper RGB and potentially the third dredge-up as AGB stars. Even so, if these stars are expected to have experienced the highest degree of mixing, yet [C/N] ≥ -0.4, their natal carbon abundance must be enhanced.

Another diagnostic of mixing vs. natal abundances is the sum of C+N+O.[1] [(C+N)/Fe] is expected to remain constant during a stars' evolution on the giant branch. At [Fe/H]= -2.0, giant stars show $\langle$[(C+N)/Fe]$\rangle \sim 0$ (Spite et al., 2006; Lardo et al., 2016). As metallicity decreases, the average [(C+N)/Fe] in the giants is seen to vary from solar to higher values, e.g. at [Fe/H] ≤ -3.0, $\langle$[(C+N)/Fe]$\rangle \sim +0.5$ For all stars in our group Group A sample, [(C+N)/Fe]$>$ +0.7 with a group mean at $\langle$[(C+N)/Fe]$\rangle = +0.85 \pm 0.10$. This is much higher than expected for typical metal-poor field stars at these metallicities. In summary, the high mean [(C+N)/Fe] supports enriched natal abundances in line with other CEMP stars.

Carbon abundances may be enriched in intermediate-mass metal-poor AGB stars as a result of the third dredge-up, mimicking CEMP-s abundance profiles (Herwig, 2005; Cristallo et al., 2011; Bisterzo et al., 2012; Hansen et al., 2016a). To eliminate the possibility that our Group A stars are highly self-enriched AGB stars, their luminosities, neutron-capture element abundances, and $^{12}C/^{13}C$ are needed. Unfortunately strong ^{13}C molecular features, as well as neutron-capture lines are inaccessible in the APOGEE spectra, warranting the need for follow-up observations in the optical regime.

2.4.2 α-elements

In ASPCAP, [α/M] serves as a free parameter in the synthetic spectral grid when performing its least squares minimization process. From the global [α/M], the abundances of the α-elements O, Mg, Si, S, Ca, and Ti are derived a posteriori. Keeping all other parameters fixed, the [α/M] dimension of the spectral grid used by ASPCAP

[1]We exclude O in our discussion as O is much less affected by CNO cycling on the RGB (Yong et al., 2008; Lardo et al., 2012)

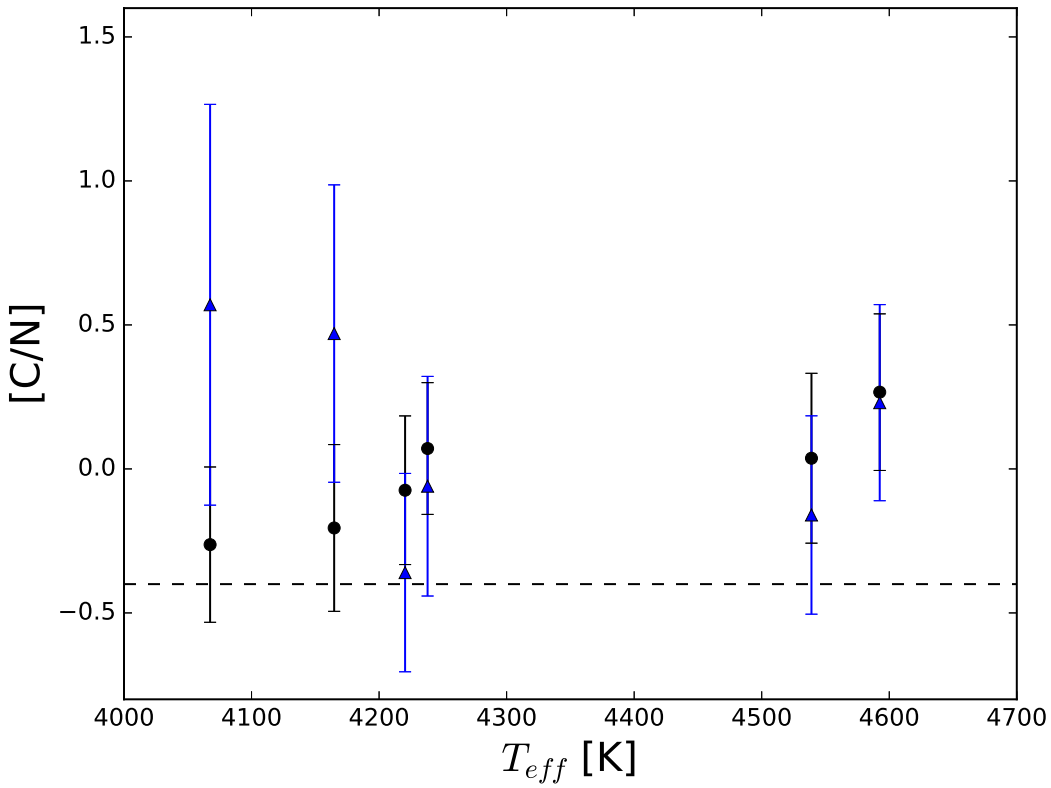

Figure 2.5 [C/N] vs. $T_{\rm eff}$ for the Group A stars. Black circles correspond to the ASPCAP abundances and blue triangles correspond to the abundances derived in this work (see sections 2.5.1, 2.5.3, and 2.6.1). The dashed line at [C/N]$= -0.4$ separates mixed ([C/N] < -0.4) and unmixed stars ([C/N] > -0.4) as prescribed by Spite et al. (2005) for extremely metal-poor giants. The large error bars on the [C/N] abundance the two coolest stars derived in this work represent the combined 2σ error as a result of difficulties in continuum placement. Despite the high likelihood of mixing in these stars considering they are on the RGB or AGB, the expression of unmixed abundance ratios is in favour of enhanced natal abundances in carbon.

is varied, and, by examining weighted spectral "windows" (regions in the spectrum sensitive to a particular species) an estimate for the individual abundance is found (García Pérez et al., 2015; Holtzman et al., 2015). As discussed in Section 2.3.2, we adopt the Fe based metallicities therefore we have calculated [α/Fe] from the [Fe/H]-[M/H] offset per star (see Table 2.3). Ti has been removed from this analysis as a result of observed deviations from the expected trend in metallicity within the APOGEE data (Holtzman et al., 2015; Hawkins et al., 2016).

Table 2.3 α-abundances for Group A stars as in the ASPCAP database. σ is from the weighted average of all *alpha*-elements here with the exception of S in 2M15312547+4220551 and Ca in 2M00114258+0109386. An empty entry means no abundance was determined by ASPCAP.

	2M15312547 +4220551	2M00114258 +0109386	2M21330683 +1209406	2M18111704 -2352577	2M16300629 -1252459	2M02121851 +4923143
[O/Fe]	-0.15 ± 0.09	-0.01 ± 0.10	0.29 ± 0.09	0.28 ± 0.08	0.32 ± 0.10	0.45 ± 0.09
[Mg/Fe]	-0.08 ± 0.16	0.19 ± 0.16	0.17 ± 0.12	0.22 ± 0.12	0.05 ± 0.14	0.21 ± 0.12
[Si/Fe]	-0.39 ± 0.09	0.05 ± 0.09	0.27 ± 0.08	0.26 ± 0.08	0.30 ± 0.09	0.47 ± 0.08
[S/Fe]	0.69 ± 0.16	0.29 ± 0.16	0.36 ± 0.12	0.37 ± 0.12	0.49 ± 0.16	0.63 ± 0.13
[Ca/Fe]	-0.67 ± 0.24	—	0.50 ± 0.15	0.23 ± 0.15	0.37 ± 0.20	0.35 ± 0.14
[α/Fe]	-0.28 ± 0.13	0.06 ± 0.09	0.29 ± 0.08	0.27 ± 0.06	0.3 ± 0.09	0.44 ± 0.09

Examining the CEMP candidates against background field stars, we compare [α/Fe] for Groups A and B to the α abundances of bulk APOGEE field stars and to metal-poor stars in the Galactic halo and disk summarized by Venn et al. (2004) and Frebel et al. (2010) in Figure 2.6. The weighted average for the Group A stars is [α/Fe] = $+0.23 \pm 0.23$, consistent with the expected enrichment of [α/Fe]$\sim +0.30$ dex for stars in the halo, indicating the majority of our sample are typical Galactic halo stars.

Two stars, 2M15312547+4220551 and 2M00114258+0109386, display α-abundances substantially lower than typical values found for halo stars at [Fe/H]~ -2.0 ([α/Fe] = -0.28 ± 0.13 and 0.06 ± 0.09, respectively). The individual α-abundances for these objects can be examined in Table 2.3. The abundances of O, Mg, Si, and Ca for 2M15312547+4220551 are all sub-solar with the exception of [S/Fe] = $+0.69 \pm 0.16$, which we expect this is the result of an unrecognised blend (see Section 2.4.3) and have ignored it here. The S abundance of 2M00114258+0109386 is also affected by nearby blends and a Ca could not be determined by ASPCAP, however the abundances of O, Mg, and Si suggest this star is α-challenged. The discovery of α-challenged stars within the Galaxy may serve as a link to the remnants of accreted dwarf galaxies in the context of Galactic evolution (see Section 2.6.3 for further discussion.)

2.4.3 ASPCAP/FERRE Limitations

Using the APOGEE-specific implementation of FERRE from Bovy (2016)[2] which includes the renormalized synthetic spectra and model atmospheres used by ASPCAP, we examine the abundances of individual spectral features and their ASPCAP weighting kernels. We also investigate nearby line contamination, upper limits, and unreported data quality issues. FERRE and ASPCAP give each spectral line a relative weighting kernel determined through a combination of methods including comparison to the solar spectrum, to the Arcturus spectrum, and by line fitting across the complete APOGEE sample (Shetrone et al., 2015).

For nearly every star in Group A, we found that the weighting scheme was not ideal, based on the spectral quality and other poor synthetic fits. As an example, the spectral windows used by ASPCAP/FERRE to estimate the S abundance for 2M15312547+4220551 are shown in Figure 2.7. Based on the width of the S I weighting kernel, nearby lines of Fe and OH are captured by the S weighting kernel. This

[2]This package is available at https://github.com/jobovy/apogee

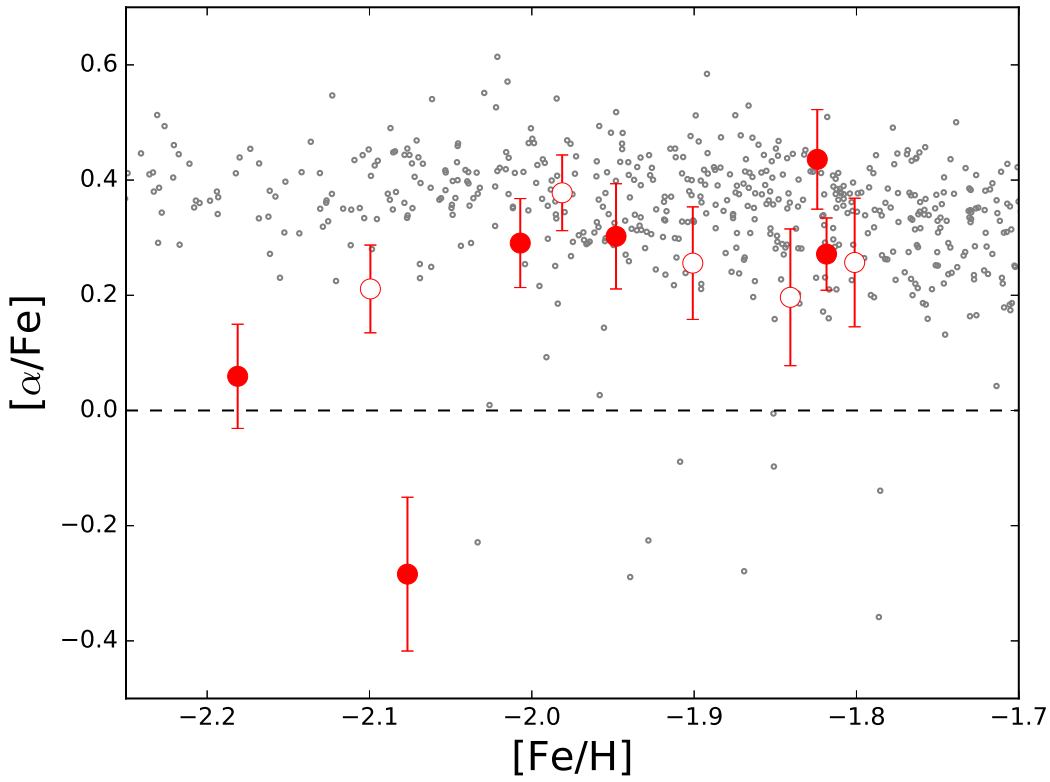

Figure 2.6 [α/Fe] vs. [Fe/H] for the Group A and Group B CEMP candidates. [α/Fe] is calculated as the uncertainty weighted average of the calibrated ASPCAP abundances for Mg, Si, S, and Ca (with the exception of S in 2M15312547+4220551 and Ca in 2M00114258+0109386.) Grey dots correspond to typical metal-poor stars from APOGEE and normal field and halo stars (Venn et al., 2004; Frebel et al., 2010), solid red circles correspond to our Group A candidates and open red circles to Group B. The dashed line at [α/Fe] = 0.0 separates the α-poor stars from the bulk of the sample.

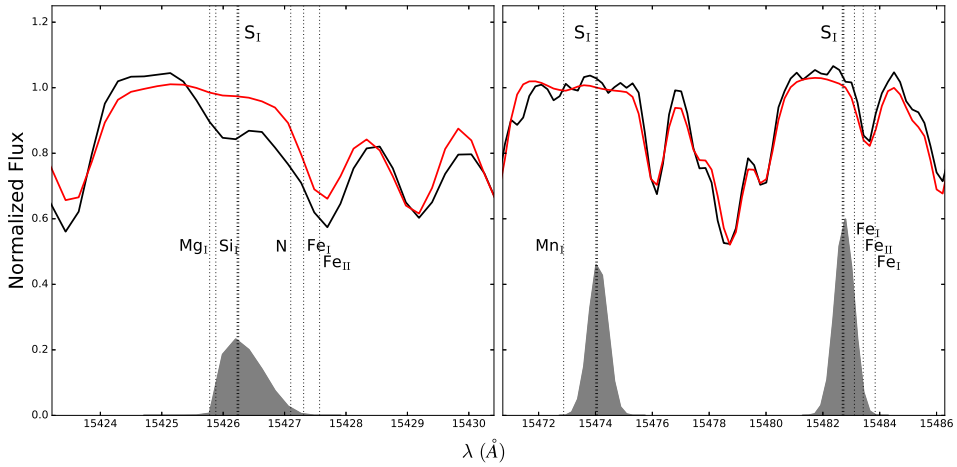

Figure 2.7 FERRE windows of the S features used to estimate a S abundance for the α-poor star 2M15312547+4220551 ([Fe/H] = -2.08 ± 0.06, [α/Fe] = -0.28 ± 0.13, [S/Fe] = $+0.69 \pm 0.16$). The APOGEE combined spectrum is in black and the ASPCAP synthetic spectrum in red. The weighing kernels used by ASPCAP/FERRE to assign a relative weight to each spectral feature when determining an overall abundance are shown in filled grey. The kernel width often results in nearby lines contributing to the perceived strength of the line of interest, increasing the estimated abundance. The width of the weighting kernel allows nearby metal lines to add to the estimated S abundance. The lack of a S line at 15,474 Å is in favour of a lower than reported S abundance.

results in a lower apparent flux in that spectral region than if the S line was the only dominant species which, in turn, forces a stronger line depth in the synthetic spectral fit. The lack of a S I line at 15,746 Å further supports a lower S abundance.

The challenge of analysing metal-poor and chemically peculiar stars with ASPCAP is not unexpected. ASPCAP covers a large multi-dimensional parameter space which is unavoidably subject to edge effects. CEMP stars exist not only at this edge, but in a parameter space that is still weakly constrained by existing data. The ASPCAP weighting scheme is a compromise to fit the features of stars over a wide range of stellar parameters, but it does not appear to apply to the most metal-poor stars, even those with the highest data quality. Consequently, we suspect all the elemental abundances in the DR12 ASPCAP database for the carbon-enhanced stars with [Fe/H]$\lesssim -2.0$ are poorly determined.

In the next section, we explore an independent model atmospheres analysis of our Group A CEMP candidates.

2.5 MOOG Spectrum Synthesis

For the six Group A CEMP candidates, we carry out a detailed model atmospheres analysis of the APOGEE spectra using the MOOG radiative transfer code[3]. The APOGEE DR12 linelist (Shetrone et al., 2015) was used for the LTE radiative transfer calculations. Spherically-symmetric, moderately CN-cycled and α-enriched ([C/Fe]= -0.13, [N/Fe]= $+0.31$, [O/Fe]= $+0.40$) model atmospheres were adopted from the MARCS grid (Gustafsson et al., 2008). Solar abundance ratios were adopted from Asplund et al. (2009) however solar C, N, and O were taken from Caffau et al. (2011). As with the ATLAS9 models used by APOGEE, the MARCS models have limited coverage for carbon-enhanced atmospheres and thus the carbon abundances were increased in MOOG to resemble a CEMP atmosphere.

The calibrated `aspcapStar` stellar parameters $T_{\rm eff}$, $\log g$, microturbulence, and [Fe/H] are required for a model atmospheres analysis and have been adopted directly from the ASPCAP pipeline. Furthermore, we do not have distances to these stars in order to use the color-temperature-metallicity calibrations, e.g. Casagrande et al. (2010) to independently derive stellar parameters.

The results of our synthesis for all Group A stars are shown in Figure 2.8, centred around the atomic C I line at 16895 Åand the derived abundances versus those returned by ASPCAP for all Group A stars are compared in Table 2.6. The following sections discuss the measured abundances for Fe, C, N, O, and the α-elements Mg, Si, S, and Ca and their comparisons to the ASPCAP results.

2.5.1 Abundance uncertainties

The abundance uncertainties in this work reflect both the systematic errors introduced through uncertainties in the adopted stellar parameters, as well as the random intrinsic errors associated with line-to-line abundance variations. Typical reported uncertainties in the ASPCAP stellar parameters $T_{\rm eff}$, $\log g$, microturbulent velocity ξ, and [Fe/H] are on the order of $\pm$100K, $\pm$0.1dex, $\pm$0.2km/s [4],and $\pm$0.1dex, respectively. The effect of these model atmosphere uncertainties on the derived abundances is shown in Table 2.4 with the total systematic uncertainty determined by adding the sensitivities from each stellar parameter in quadrature (ignoring covari-

[3]MOOG was originally written by Chris Sneden (1973), and has been updated and maintained, with the current versions available at http://www.as.utexas.edu/~chris/moog.html.

[4]Holtzman et al. (2015) shows an rms scatter in ξ vs. $\log g$ of 0.22 km s^{-1} for stars with $\log g < 3.8$.

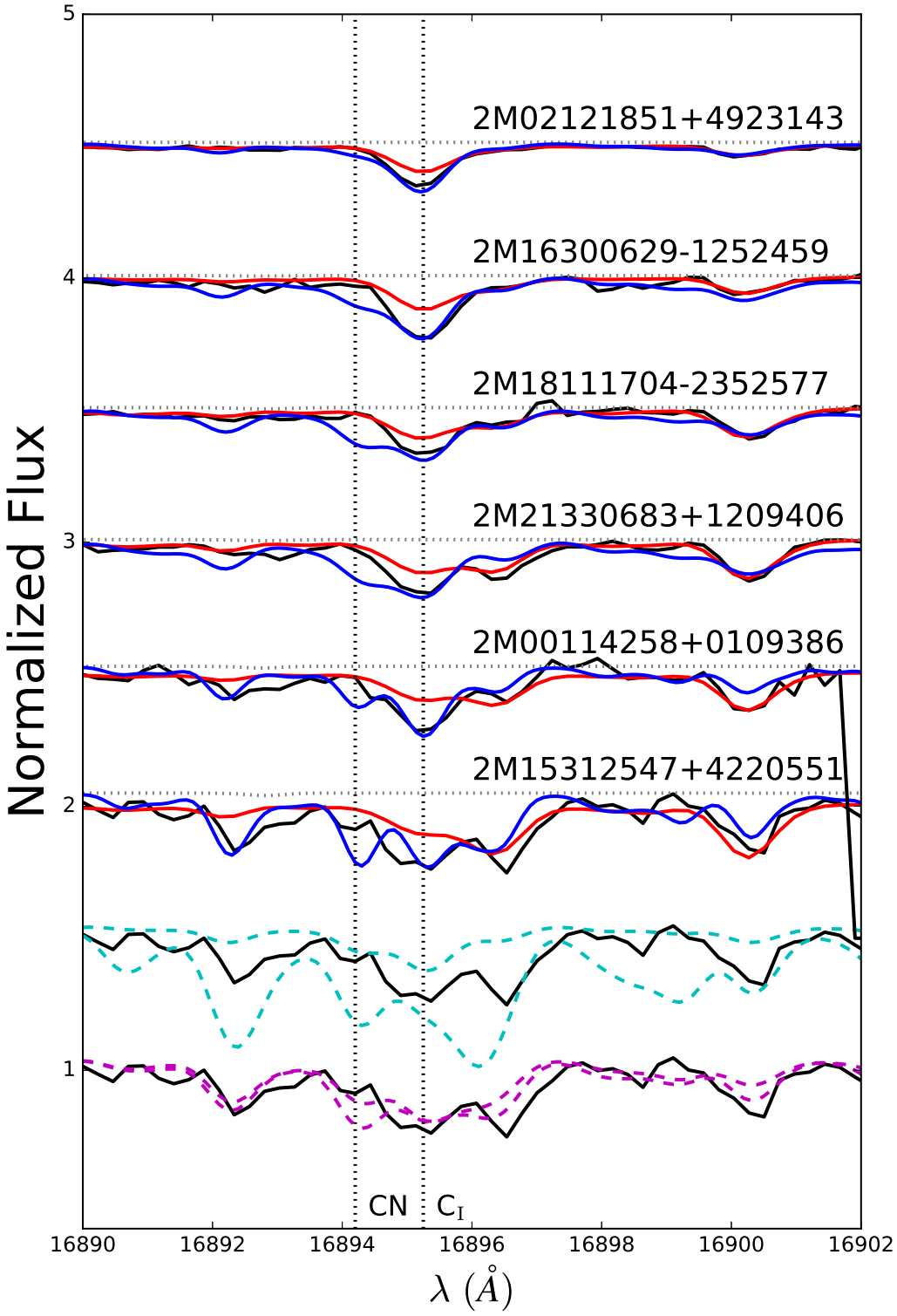

Figure 2.8 Spectra of Group A stars centred around the atomic C I line. The APOGEE combined spectrum (black) with the ASPCAP synthetic spectrum (red) is shown

Table 2.4 Systematic Abundance Sensitivities. Errors shown here were added in quadrature to calculate the total systematic uncertainty and do not reflect the uncertainty introduced by line-to-line scatter. See Table 2.6 for line-to-line measurement errors. Since S and Ca abundances could not be determined for 2M15312547+4220551, systematic errors were not investigated.

	$\Delta T_{\rm eff}$ +100 K	Δ logg +0.1 dex	$\Delta\xi$ +0.5 km s^{-1}	Δ[Fe/H] +0.1 dex	Total
2M15312547+4220551 ($T_{\rm eff}$ = 4068 K)					
[C/Fe]	0.20	-0.05	-0.04	-0.04	0.21
[N/Fe]	-0.14	-0.03	-0.02	-0.04	0.15
[O/Fe]	-0.16	-0.11	-0.02	0.10	0.22
[Mg/Fe]	-0.25	-0.11	-0.06	-0.08	0.29
[Si/Fe]	-0.20	0.15	0.08	0.08	0.27
2M02121851+4923143 ($T_{\rm eff}$ = 4593 K)					
[C/Fe]	0.20	-0.05	-0.04	-0.03	0.21
[N/Fe]	0.17	-0.06	0.02	-0.02	0.18
[O/Fe]	-0.13	-0.10	-0.01	-0.02	0.16
[Mg/Fe]	0.05	-0.07	-0.02	0.02	0.09
[Si/Fe]	0.08	0.09	0.05	-0.04	0.14
[S/Fe]	-0.20	-0.05	-0.04	-0.04	0.21
[Ca/Fe]	-0.10	-0.10	-0.08	-0.06	0.17

ances). The effect of these uncertainties was investigated for two stars in our sample, 2M15312547+4220551 and 2M02121851+4923143, to span our full temperature range. Systematic errors are higher for the cooler star by $\sim$ 0.1dex which is reasonable considering the stronger effects of molecular blends and subsequent difficulty in continuum placement at lower temperature. Owing to similar temperatures and SNR, the systematic abundance uncertainties found for 2M15312547+4220551 ($T_{\rm eff}$ = 4068K) were also applied to 2M00114258+0109386 ($T_{\rm eff}$ = 4165K). The systematic uncertainties for 2M02121851+4923143 ($T_{\rm eff}$ = 4593K) were applied to the remaining three stars in our sample.

Intrinsic abundance uncertainties were determined for each spectral line by first calculating the *observed - synthetic* residual over a spectral feature, and by then adjusting the abundance until this residual was comparable in magnitude to deviations in the continuum noise. The total intrinsic measurement error for a species X was then determined as the mean in the line-to-line scatter $\sigma_X/\sqrt{N_X}$. These abundance uncertainties are reflected in Table 2.6. The systematic uncertainties and intrinsic

uncertainties are added in quadrature to calculate the total abundance uncertainty used in the discussion and Figures 2.5 and 2.8.

2.5.2 Fe abundances

Initially, we examined the ASPCAP synthetic spectra and found the general fits to the Fe lines to quite good, and therefore we expect the FERRE stellar parameters ($T_{\rm eff}$, $\log g$, and [Fe/H]) to be in fair agreement. As an iteration on this, we also examined isolated Fe I lines in each Group A star by-eye. Averaging over the 54 Fe I lines used by ASPCAP to determine the abundance of Fe, we still did not observe any sign of deviation in the spectra or the synthetic fits. We adopt [Fe/H] from ASPCAP as an initial stellar parameter in our synthetic synthesis.

Testing this further, the isolated Fe I features were synthesized in MOOG for a sample star, 2M02121851+4923143. This star was selected as its temperature is the highest in our sample ($T_{\rm eff} = 4593$K) and we would expect the degeneracy between $T_{\rm eff}$ and [Fe/H] to be the most prominent in this spectrum as high $T_{\rm eff}$ and low metallicity produce similar observed effects in the spectra (i.e. weak Fe lines). In Table 2.5, individual Fe I abundances are shown and the mean Fe abundance was determined through a weighted average of all the individual line, with the weights given by $1/\sigma_i^2$ where σ_i is the abundance uncertainty on each line (see Section 2.5.1). The metallicity from MOOG was determined as [Fe/H] $= -1.7 \pm 0.1$ based on 21 FeI lines. ASPCAP reports [Fe/H] $= -1.82 \pm 0.06$ for this star, consistent within the 1σ measurement errors to the results of this work.

2.5.3 Carbon, Nitrogen, and Oxygen

ASPCAP determines C and N abundances by simultaneously fitting multiple CN and CO molecular features over the full spectral range. Oxygen is later determined from the α-abundance as discussed in Section 2.4.2 and 2.5.4. Since multiple metals contribute to the strength and structure of these molecular bands, the method employed by ASPCAP to determine the abundances of C, N, and O is not sensitive to the degeneracies that may exist in the abundances of these three species.

To break these possible degeneracies, we follow the process established by Smith et al. (2013) and Lamb et al. (2015) and use a line-by-line procedure to derive the C, N, and O abundances. Isolated atomic and molecular features were synthesized and the model atmosphere was updated to incorporate the new abundance estimate.

Table 2.5 Fe I lines measured in 2M02121851+4923143

Wavelength (Å)	χ(eV)	log gf	Log abundance
15211.75	6.323	-2.285	5.83
15223.78	5.587	-0.082	5.93
15298.74	5.308	0.65	5.88
15595.76	6.364	0.659	5.83
15625.92	5.539	0.253	5.78
15636.22	5.351	-0.114	5.93
15681.81	6.246	0.157	5.98
15727.88	5.62	-0.03	5.98
15899.57	6.258	0.222	5.68
15969.23	5.921	-0.128	5.48
16045.04	5.874	0.066	5.68
16106.81	5.874	0.196	5.88
16130.31	6.351	0.624	5.78
16157.66	5.351	-0.743	5.68
16169.45	6.319	0.723	5.83
16320.78	6.28	0.871	5.88
16521.74	6.286	0.5	5.78
16528.98	6.336	0.577	5.63
16566.29	5.978	0.065	5.78

Using the atomic C I line at 16895 Å an initial carbon abundance was found and used as a seed for an O abundance estimate. OH lines with no CN contamination were then synthesized to measure the oxygen abundance. Adopting mean O abundance, C was re-determined from the C I line alone. This process was iterated until the C and O abundances converged, typically requiring two iterations. Finally, using the best C estimate, N was measured via CN lines between 15100 and 16100 Å. The complete line list is given in Table 2.9. The mean abundance and final error for each species was calculated in similar fashion to the iron lines in Section 2.5.2.

We chose to focus only on the atomic C I line for a few reasons. At high C, N, and O abundances, like those expected in the CEMP stars, the structure of the CO and CN molecular features is highly degenerate, prohibitive in determining abundances with any reasonable uncertainty. Temperature effects magnify these issues as well: at low $T_{\rm eff}$ ($\lesssim$ 4000K) these molecular features dominate the spectra resulting in strong molecular blends, making it exceptionally difficult to separate the effects each species has on the spectral features as well as complicating the placement of the continuum. In stars with temperatures greater than $\sim$ 4600K, these molecular features disappear as discussed in Section 2.3.1. The atomic line is solely dependent on the C abundance and thus the effects of N, O, and $T_{\rm eff}$ seen in the molecular bands is not observed. [5] High $T_{\rm eff} > 4600$ K remains an issue, however these stars have been removed from our sample as discussed in sections 2.3.1 and 2.3.2.

Further supporting our choice of using the atomic line alone, in their analysis of four metal-poor giant stars in globular clusters, Lamb et al. (2015) incorporated the atomic C I line into their determination of [C/Fe]. Comparing the C abundance derived from the atomic line alone (see their supplementary atomic and molecular line list) to their global, non-NLTE corrected C abundance for each star (their Table 7, adjusted for a -0.1 dex NLTE offset in [Fe/H]), the differences are on the order of 0.1 dex or less. While this is a small sample, these results suggest the atomic line alone may provide an accurate estimation of the global C abundance when the degeneracy between C, N, and O is properly handled.

Finally, the atomic C Iline is not used by APOGEE when estimating a C abundance, presumably due to the typically lower SNR at this wavelength in the APOGEE spectra. While the SNR around this line in our candidate spectra provides the source

[5] The atomic data available for the C I transition is high fidelity and has been assigned a 90% confidence rating by NIST. Manually changing $\log gf$ in our linelist by 10%, to account for the small uncertainty in atomic data, results in variations in the derived C abundance that are imperceivable ($\lesssim$ 0.05 dex) considering the quality of our spectra.

for our large uncertainties in our reported C abundance, we are able to clearly see this line in our Group A spectra, allowing us to determine a C abundance through a method independent of APOGEE.

The carbon abundances derived through MOOG were found to be within the uncertainties of the C-abundance reported by ASPCAP for the four warmer stars in our sample. Typical deviations in $[C/Fe]_{ThisWork} - [C/Fe]_{ASPCAP}$ for these four stars were on the order of 0.1 dex, half of the standard error reported for this abundance. The two cooler stars show much larger deviations in [C/Fe] which we attribute to the difficulty in continuuum placement at these lower temperatures and thus we chose to adopt the 2σ errors for abundances of these stars. The agreement between our work and the ASPCAP results cautiously supports the reliability of the reported abundance for our Group A stars.

Oxygen abundances were determined using 25 OH lines per star, spanning the full range of the APOGEE spectra. Again, owing to the degeneracies between C, N, and O, the molecular CO bands were avoided when possible while measuring O. The O abundances reported in this work are systematically higher than the ASPCAP abundances, with differences up to 0.5 dex. We suspect this discrepancy is a consequence of continuum placement and the simultaneous estimations of C, N, and O by ASPCAP, rather than following the iterative procedure of Smith et al. (2013). Lamb et al. (2015) highlights the sensitivity of the abundances derived for these species when analysing infrared spectra.

Nitrogen abundances were determined through synthetic spectral fits of the CN electronic transition lines, primarily in the "blue" chip, after the C and O abundances were determined. The N abundances measured for the warmest Group A stars are consistent with the ASPCAP values to within the 1σ uncertainties, however a systematic increase in our measured abundance is observed for the two coolest stars. At lower temperatures, the degeneracy between C and N in these CN lines becomes stronger. Despite a reportedly high SNR and no visible persistence issues, the spectral quality over the "blue" chip for these two cooler stars is poor ($SNR \sim 20$) and the measured abundances may also be affected by issues in normalization and placement of the continuum. We additionally note the poor synthetic fit to the CN band at 16894 Å in Figure 2.8 for all Group A stars. This implies the reported N abundance is too high, however this is presumably due to poor atomic data for this particular transition. The small degree of line-to-line scatter in the N abundance derived by the multiple CN lines in the 'blue' chip supports higher fidelity atomic data for those

transitions and supports the reliability of the reported abundance.

Table 2.6 Comparison of Group A abundances derived from ASPCAP and MOOG spectrum syntheses. Abundance errors shown here reflect the measurement error $\sigma/\sqrt{N}$ where σ is the standard deviation of the line-to-line scatter and N is the number of lines used in calculating an average abundance. Systematic errors as a result of uncertainties in the stellar parameters are shown in Table 2.4. A blank entry means no abundance could be reliably determined as a result of the quality of the spectra.

Species	Source	2M15312547 +4220551	2M00114258 +0109386	2M21330683 +1209406	2M18111704 -2352577	2M16300629 -1252459	2M02121851 +4923143
[Fe/H]	ASPCAP	-2.08 ± 0.06	-2.18 ± 0.06	-2.01 ± 0.06	-1.82 ± 0.06	-1.95 ± 0.06	-1.82 ± 0.06
[C/Fe]	ASPCAP	0.75 ± 0.17	0.84 ± 0.19	0.91 ± 0.17	0.76 ± 0.15	0.97 ± 0.21	0.82 ± 0.19
	This Work	1.25 ± 0.30	1.06 ± 0.20	0.98 ± 0.15	0.77 ± 0.20	1.11 ± 0.15	0.75 ± 0.13
[N/Fe]	ASPCAP	1.02 ± 0.21	1.05 ± 0.22	0.98 ± 0.19	0.68 ± 0.18	0.93 ± 0.21	0.56 ± 0.19
	This Work	0.67 ± 0.12	0.59 ± 0.10	1.34 ± 0.14	0.83 ± 0.17	1.27 ± 0.14	0.52 ± 0.15
[O/Fe]	ASPCAP	-0.15 ± 0.09	-0.01 ± 0.10	0.29 ± 0.09	0.28 ± 0.08	0.32 ± 0.10	0.45 ± 0.09
	This Work	0.15 ± 0.14	0.24 ± 0.12	0.79 ± 0.10	0.82 ± 0.13	0.89 ± 0.08	0.42 ± 0.10
[Mg/Fe]	ASPCAP	-0.08 ± 0.16	0.19 ± 0.16	0.17 ± 0.12	0.22 ± 0.12	0.05 ± 0.14	0.21 ± 0.12
	This Work	-0.57 ± 0.22	-0.48 ± 0.18	-0.19 ± 0.14	-0.05 ± 0.15	-0.10 ± 0.15	0.00 ± 0.13
[Si/Fe]	ASPCAP	-0.39 ± 0.09	0.05 ± 0.09	0.27 ± 0.08	0.26 ± 0.08	0.3 ± 0.09	0.47 ± 0.08
	This Work	< 0.33	-0.39 ± 0.24	0.14 ± 0.17	0.12 ± 0.17	0.05 ± 0.14	0.08 ± 0.13
[S/Fe]	ASPCAP	0.69 ± 0.16	0.29 ± 0.16	0.36 ± 0.12	0.37 ± 0.12	0.49 ± 0.16	0.63 ± 0.13
	This Work	—	—	—	—	—	< 0.17
[Ca/Fe]	ASPCAP	-0.67 ± 0.24	—	0.50 ± 0.15	0.23 ± 0.15	0.37 ± 0.20	0.35 ± 0.14
	This Work	—	—	—	—	—	< 0.07

2.5.4 α-elements

Abundances for the *alpha*-elements Mg, Si, S, and Ca were determined through the MOOG synthetic spectrum analysis. Similar to O, much larger variations between the ASPCAP abundances and those determined in this work are observed than for C and N. The primary source for these discrepancies resides in the method ASPCAP uses to determine the abundances for the *alpha*-elements. As discussed in Section 2.4.2, ASPCAP uses [α/M] as a free parameter to generate a model spectrum and then scales the abundance of each *alpha*-element based on the line-list and weighting windows for each element. This process works well if the abundance of a particular α-element does not vary from the overall α-abundance and if the weighting kernels are dominated by the species of interest (however we have shown that even this can fail, e.g. the isolated S I lines in 2M15312547+4220551.) By treating each line and each species individually, we arrive at a less biased abundance estimate. We are also able to determine upper limits in our process and identify when the ASPCAP abundance is not a determination, but likely an upper limit. The line list for these species is given in Table 2.8.

Magnesium: Mg abundances were determined using three lines between 15745 Åand 15770 Å. These lines were also used to set the Gaussian broadening parameter in our synthetic spectra and provided a clear estimate for the placement of the continuum. Comparing the ASPCAP abundances to our MOOG results shows that ours are typically lower by $\sim$ 0.3 dex. We suggests this reflects issues in the continuum normalization of the ASPCAP spectra or under-represented systematic errors when adopting the ASPCAP stellar parameters (see Section 2.5.1 for typical errors reported by ASPCAP).

Silicon: Six lines spanning the "green" and "red" chips were used to determine the Si abundance for our Group A stars. Si was found to be lower than what was reported by APOGEE by $\sim$ 0.3 dex and only an upper limit could be determined for 2M1531257+4220551. Large line-to-line scatter up to 0.5 dex were observed, particularly in the cooler stars where continuum placement became more spurious as a result of numerous molecular features.

Sulphur and Calcium: The abundances of S and Ca could not be reliably determined for any of the Group A stars. Low SNR, weak spectral features, poor normalization of the combined spectra, and blending with nearby Fe lines were prohibitive in identifying the presence of a line. With the exception of 2M02121851+4923143,

even upper limits could not be determined for the Group A stars as spectral fluxes well above the continuum identified by nearby strong lines.

2.6 Discussion

2.6.1 CEMP stars confirmed

Through our synthetic spectrum analysis, carbon-enhancement has been verified for the Group A candidates to within the precision of the stellar parameters and model atmospheres used by APOGEE. Since the N abundances determined in this work have undergone a shift to higher [N/Fe] than reported by ASPCAP, and since the interpretation of the nature of CEMP stars is heavily reliant on understanding natal vs. evolved abundances as explored in Section 2.4.1, we re-examine the possibility of mixing within our sample. Figure 2.5 includes the [C/N] ratios derived in this work for the Group A stars. Following the discussion in Section 2.4.1, the four warmer objects in our sample appear to remain as unmixed giants, despite the high likelihood of mixing on the RGB. This strongly supports a high natal carbon abundance in these stars. The nature of the two cooler stars however is less clear. As suggested in Section 2.5.3, molecular blends obfuscate the spectra at low temperature, making it exceedingly difficult to accurately place the continuum when comparing synthetic spectra to data. While the abundances of C, N, and [C/N] are still higher than expected for typical mixed metal-poor giants, the consequences of mixing are difficult to interpret until higher precision abundances are available.

We have additionally estimated the carbon corrections of our Group A stars following the procedure developed by Placco et al. (2014). These corrections work to account for CN processing on the upper RGB and return a natal carbon abundance based on stellar parameters. Using their online calculator[6], we find the carbon corrections for the Group A stars are typically δ[C/Fe]= +0.2dex. While this further supports the assertion the Group A stars are truly carbon-enhanced, the corrections are within our combined errors on [C/Fe]. Since we are limited by systematics when attempting to determine more precise abundances, to remain consistent with the ASPCAP labels we choose to not adopt the carbon corrections in our current discussion. It is worth noting more CEMP stars are likely to be found within APOGEE if these corrections are applied homogeneously across the database. As an example, stars

[6]http://www3.nd.edu/∼vplacco/carbon-cor-input.html

with $\log g = 1.0$, [Fe/H]$= -2.0$, and [C/Fe]$_{ASPCAP} = +0.5$ can be corrected up to a natal [C/Fe]$= +0.9$ using the carbon correction calculator which would classify them as CEMP stars. We leave this as an exercise for later data releases when higher precision abundances become available.

2.6.2 Radial velocity variations and binarity

Since neutron capture spectral lines are not available in the wavelength regime covered by APOGEE, it is impossible to classify CEMP candidates into the subclasses (CEMP-s, CEMP-r/s, CEMP-no), however other indicators towards the nature of these stars exist. As mentioned in the introduction, a high binary fraction has been observed for CEMP-s stars. Lucatello et al. (2005) inspected the binary frequency among 19 CEMP-s stars by investigating radial velocity (RV) variations with a minimum baseline of $\sim$200 days. They found a binary fraction $\sim$ 68%, higher than the expected detection fraction of $\sim$ 36% assuming a true binary fraction of 100%, suggesting all CEMP-s are found in binaries. Starkenburg et al. (2014) also constrained the binary fraction and periods using tailored Monte Carlo simulations and a maximum-likelihood analysis. Their results reinforce the conclusions made by Lucatello et al. (2005), that a binary fraction of $\sim$ 100% and period distribution $\leq 20,000$ days best represent the RV variations seen within the CEMP-s and classical CH star data groups. Conversely, only two stars in their CEMP-no sample show evidence of short-period radial velocity variations, lightly comparable to observed solar neighbourhood binary fraction ($\sim$ 45%), but highly discrepant to the observed binary properties of the CEMP-s stars. More recently, Hansen et al. (2016a,b,c) sought to determine the frequency of binary systems among CEMP stars in a precise and homogeneous manner, with the goal of testing the statistical viability of AGB binary companion mass transfer as a mechanism for carbon enhancement. Nearly a decade of observations on 22 previously identified CEMP-s and CEMP-r/s stars revealed a binary fraction of 82$\pm$10%.

Aoki et al. (2007); Norris et al. (2013); Carollo et al. (2014); Bonifacio et al. (2015); Hansen et al. (2016a); Yoon et al. (2016) have demonstrated that CEMP-s stars dominate at [Fe/H]> -3, meaning the higher metallicity CEMP-s stars should be visible to APOGEE, and with such a high binary fraction, binaries should be evident in our sample, which we can explore from the multiple visits of each star carried out by the APOGEE survey.

We examine the RV reported by APOGEE per visit. The APOGEE radial velocities come in two flavours: relative and synthetic. Relative RV's are iteratively determined by comparing the individual visit spectra to a template (the visit spectrum with the highest S/N is used as the template in the first iteration), shifting the visit spectra to a mean velocity wavelength scale, and creating a combined spectrum to be used as the new template. This process is repeated until the shifted and resampled visit spectra converge with the combined spectrum. In order to determine the synthetic RV's, a best-fitting synthetic spectrum is needed. By matching the combined spectrum to a synthetic spectrum from a grid of 538 synthetic spectra, the best-fit synthetic template can be found. From this best-fit synthetic template, the visit spectra are cross-correlated to determine synthetic radial velocities. Nidever et al. (2015) suggest the relative velocities should be preferred since they do not depend on the integrity of synthetic library and thus, we adopt relative radial velocity for our analysis.

As a result of the uncertainties in the RV determination, the APOGEE pipeline is unable to directly flag binary systems, however the parameter `apogeeStar.vscatter` (σ_{v_r}), the standard deviation of visit spectra RV's relative to the mean, provides the most insight on potential binary status. Nidever et al. (2015) investigated the dependence of σ_{v_r} as a function of $T_{\rm eff}$, S/N, and [Fe/H] and found a peak scatter $\sim$ 100-150m/s, characterizing the intrinsic RV uncertainty in the APOGEE spectra. The authors suggest that if $\sigma_{v_r} > 1$ km/s (an order of magnitude larger than the typical uncertainties), then the star is likely a binary. While this assertion is not currently supported in a statistical manner, work is being done to establish a dependable binary identification method (Troup et al., in preparation).

Figure 2.9 summarizes the scatter in RV for the six Group A stars. Only one star in the group, 2M15312547+4220552, has RV scatter greater than 1 km/s. This scatter seen is in agreement with the radial velocity variations seen by Hansen et al. (2016c) in their sample of CEMP-s stars ($\sigma_{RV} = 5.6 \pm 5.0$ km/s) and are larger than the mean variations measured by Starkenburg et al. (2014) ($\sigma_{RV} = 0.7 \pm 0.8$ km/s). The remaining five candidates show little to no variation, and one star, 2M18111704-2352577, only had one visit.

This implies a binary fraction for our sample of 16%. If all our candidates were CEMP-s, following the binary fraction by Hansen et al. (2016c) of 82$\pm$10%, we would expect to to find $\sim 5\pm 1$ binaries in our sample. Although it is admittedly difficult to comment statistically on such small sample sizes, perhaps our sample is comprised

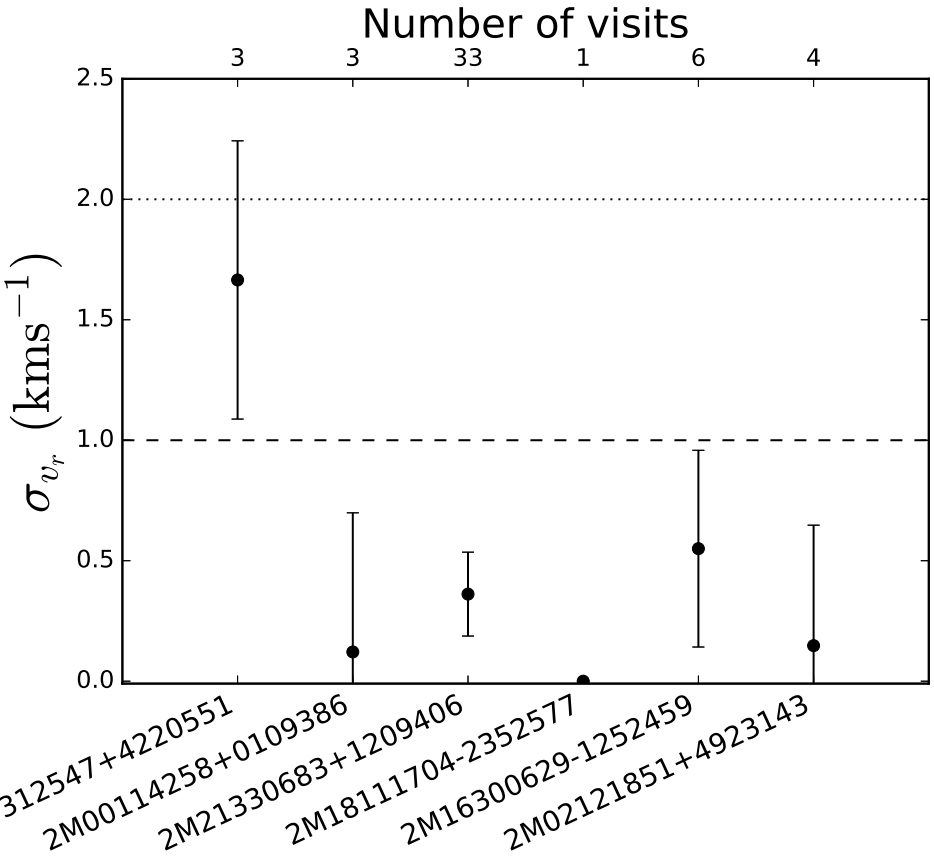

Figure 2.9 Scatter in radial velocity (σ_{v_r}) for the six Group A stars sorted by $T_{\rm eff}$ (ascending left to right), error bars represent $1/\sqrt{N_{visits}}$. The line at 1 km/s represents our 1σ cut for binarity consideration as suggested by the APOGEE team; the dashed line signifying the 2σ. 2M18111704-2352577 has been included in the figure for completeness, however only one visit makes it impossible to determine variation in the radial velocity.

of other CEMP subtypes and/or the presence of binary systems with RV scatter less than 1 km/s like those found in Starkenburg et al. (2014) and Hansen et al. (2016c). If our sample includes CEMP-no stars, a lower binary fraction is expected. CEMP-no stars do not exhibit a statistically significant binary fraction (Starkenburg et al., 2014; Hansen et al., 2016b). Following the CEMP-no binary fraction of 17±9% found by Hansen et al. (2016b), for a sample comprised only of CEMP-no stars, we would expect $\sim 1 \pm 1$ binaries within our sample, as found, however similar numbers are expected from the binary fraction (16±4%) seen in typical field red giants (Carney et al., 2003).

(Spite et al., 2013; Bonifacio et al., 2015; Hansen et al., 2015; Yoon et al., 2016) have additionally shown that the nature of these stars may be unlocked through an analysis of the A(C) alone. Examining Table 2.2, all of our Group A stars have $7.1 < A(\mathrm{C}) \lesssim 7.5$, based on the calibrated [C/H] from ASPCAP. This range of A(C) is higher than the mid-point of the peaks in the Yoon et al. (2016) distribution, placing our stars in the high-C band. This has two primary implications: the Group A stars are more likely to be CEMP-s or CEMP-r/s and they are most likely in binary systems. This second point contradicts our radial velocity analysis, especially for 2M15312547+4220552 which has the lowest A(C) in our sample but is also the strongest candidate for a binary system, however the possibility remains our candidates are long period binaries with radial velocity variations that are too small over the duration of the APOGEE observations. A small number of CEMP-no stars and single star systems are found in the high-C band as well, especially at the 'intermediate' C-abundances seen in Group A, sustaining the claim Group A is composed of multiple CEMP subtypes. Follow-up optical analysis with access to the CH G-band would strengthen the reliability of the carbon abundances derived for the Group A stars and would grant access to neutron-capture spectral lines, allowing for a two direction approach on the classification of these stars.

2.6.3 CEMP-no stars in dwarf galaxies

CEMP-no stars have been identified in dwarf galaxies surrounding the Milky Way (Lai et al., 2011; Honda et al., 2011; Norris et al., 2013; Gilmore et al., 2013; Skúladóttir et al., 2015; Salvadori et al., 2015). Salvadori et al. (2015) examined the frequency of CEMP-no stars in the dwarf galaxies and concluded CEMP-no stars are expected in all dwarf galaxies with the relative fraction of these stars increasing at lower metallicities,

as seen in the Milky Way. However, they also predict the probability to detect these objects scales strongly with the luminosity and the metallicity distribution function (MDF) of the dwarf galaxy. In the more luminous, classical dSph galaxies, CEMP-no stars are expected to be observed at higher metallicities[7], on average, with an overall detection probability $P \leq 0.02$ In the ultra-faint systems, a broader MDF and lower luminosity increases the probability of detection to $P \sim 0.1$ with an increased likelihood of observing these stars at lower metallicity.

Congruently, sub-solar α-ratios are observed for stars in the Local Group dwarf galaxies as a result of differing star formation histories (e.g. see Venn et al. (2004); Tolstoy et al. (2009); Frebel & Norris (2015)). Highlighted in Section 2.4.2, two of the Group A stars, 2M15312547+4220551 and 2M00114258+0109386, have sub-solar α-ratios based on their calibrated ASPCAP abundances. Despite large error bars, these low α-ratios were confirmed in Section 2.5.4. α-challenged stars are an uncommon observation at the metallicity of 2M15312547+4220551 and 2M00114258+0109386 ([Fe/H]≤ -2.0) indicating these are unique objects more similar to stars in the faint dwarf galaxies than to Galactic field stars.

Furthermore, Shetrone et al. (2001, 2003); Cayrel et al. (2004); Letarte et al. (2010); North et al. (2012); Venn et al. (2003) have identified sub-solar abundance patterns of odd-Z elements for individual stars in the dwarf galaxies. The ASPCAP DR12 database shows the abundances of the odd-Z elements Na, K, and V for 2M15312547+4220551 and 2M00114258+0109386 are within 1σ of scaled solar and do not show any unusual abundance trends. [Mn/Fe] is reported at -0.27 ± 0.15 and -0.23 ± 0.15 for 2M15312547+4220551 and 2M00114258+0109386, respectively, however Mn is subject to strong HFS effects and must be examined more carefully with optical data. While the positions of these stars do not overlap with the position of any known dSphs in the Local Group, finding new α-poor/odd-Z-poor/metal-poor stars that are also C-rich could point towards objects with origins in an accreted dwarf galaxy. High resolution optical analysis is needed to confirm the nature of these seemingly high interest stars.

2.6.4 Comparison to Data Release 13

[7]The CEMP-no detection likelihood peaks at [Fe/H]≈ -2 for a Sculptor-like dSph galaxy.

Table 2.7: Comparison of stellar parameters and abundances between DR12 and DR13. The first line for an object shows the DR12 results with the following line containing the DR13 results. An empty entry means no abundance was determined by ASPCAP.

ID	$T_{\rm eff}$ (K)	$\log g$ (dex)	ξ (km s^{-1})	[Fe/H] (dex)	[C/Fe] (dex)	[N/Fe] (dex)	[O/Fe] (dex)	[α/Fe] (dex)	Group
DR12 and DR13:									
2M11584435+5518120 (DR12)	4555	1.29	1.94	-1.80 ± 0.06	0.74 ± 0.19	0.40 ± 0.20	0.24 ± 0.10	0.28 ± 0.21	B
2M11584435+5518120 (DR13)	4502	1.34	1.67	-1.80 ± 0.05	0.78 ± 0.12	0.59 ± 0.12	0.31 ± 0.11	0.34 ± 0.16	
2M14571988+1751501 (DR12)	4566	1.35	1.92	-1.90 ± 0.06	0.78 ± 0.2	0.67 ± 0.20	0.28 ± 0.10	0.19 ± 0.17	B
2M14571988+1751501 (DR13)	4516	1.37	1.67	-1.86 ± 0.06	0.78 ± 0.18	0.83 ± 0.16	0.4 ± 0.16	0.32 ± 0.11	
2M02121851+4923143 (DR12)	4593	1.61	1.85	-1.82 ± 0.06	0.82 ± 0.19	0.56 ± 0.19	0.45 ± 0.09	0.42 ± 0.14	A
2M02121851+4923143 (DR13)	4517	1.65	1.65	-1.82 ± 0.05	0.84 ± 0.17	0.67 ± 0.16	0.49 ± 0.15	0.47 ± 0.17	
DR12 Only:									
2M15312547+4220551	4068	-0.15	2.38	-2.08 ± 0.06	0.75 ± 0.17	1.02 ± 0.21	-0.15 ± 0.09	-0.12 ± 0.45	A
	—	—	—	—	—	—	—	—	
2M00114258+0109386	4165	-0.14	2.38	-2.18 ± 0.06	0.84 ± 0.19	1.05 ± 0.22	-0.01 ± 0.1	0.13 ± 0.12	A
	4161	1.15	1.67	-1.67 ± 0.05	0.66 ± 0.10	—	-0.06 ± 0.07	-0.15 ± 0.08	
2M21330683+1209406	4220	0.39	2.21	-2.01 ± 0.06	0.91 ± 0.17	0.98 ± 0.19	0.29 ± 0.09	0.32 ± 0.11	A
	4271	1.1	1.67	-1.6 ± 0.05	0.92 ± 0.12	—	0.19 ± 0.09	0.10 ± 0.14	
2M18111704-2352577	4238	0.65	2.13	-1.82 ± 0.06	0.76 ± 0.15	0.68 ± 0.18	0.28 ± 0.08	0.27 ± 0.05	A
	4298	1.2	1.67	-1.61 ± 0.05	0.82 ± 0.10	0.91 ± 0.11	0.28 ± 0.08	0.16 ± 0.07	
2M16334467-1343201	4288	0.23	2.26	-2.1 ± 0.06	0.89 ± 0.19	1.02 ± 0.2	0.19 ± 0.09	0.20 ± 0.1	B
	4349	1.02	1.67	-1.7 ± 0.05	0.86 ± 0.08	—	0.08 ± 0.07	0.03 ± 0.11	
2M12473823-0814340	4317	0.79	2.08	-2.24 ± 0.06	0.75 ± 0.20	-0.14 ± 0.22	0.87 ± 0.10	0.67 ± 0.35	C

	4681	3.1	1.24	-0.63 ± 0.03	0.12 ± 0.07	0.14 ± 0.09	0.42 ± 0.07	0.36 ± 0.24	
2M16562103+1002085	4376	0.93	2.05	-1.98 ± 0.06	0.88 ± 0.18	0.95 ± 0.20	0.41 ± 0.09	0.38 ± 0.06	B
	4368	1.23	1.67	-1.76 ± 0.05	0.84 ± 0.05	0.95 ± 0.06	0.25 ± 0.05	0.18 ± 0.07	
2M16300629-1252459	4539	0.99	2.03	-1.95 ± 0.06	0.97 ± 0.21	0.93 ± 0.21	0.32 ± 0.10	0.31 ± 0.15	A
	4537	1.22	1.67	-1.78 ± 0.05	0.97 ± 0.09	—	0.21 ± 0.10	0.27 ± 0.21	
2M16385680+3635073	4561	1.46	1.89	-1.84 ± 0.06	0.88 ± 0.20	0.29 ± 0.20	0.23 ± 0.10	0.10 ± 0.23	B
	4589	1.57	1.66	-1.73 ± 0.05	0.95 ± 0.18	0.53 ± 0.17	0.49 ± 0.16	0.21 ± 0.20	
2M05352696-0510173	4591	2.34	1.64	-1.9 ± 0.06	0.75 ± 0.22	-0.48 ± 0.23	0.25 ± 0.11	0.37 ± 0.19	C
	—	—	—	—	—	—	—	—	
DR13 Only:									
2M10331492+2936548	4332	0.76	2.10	-1.95 ± 0.06	0.62 ± 0.17	0.74 ± 0.19	0.30 ± 0.09	0.22 ± 0.13	
	4357	1.18	1.67	-1.83 ± 0.05	0.73 ± 0.05	0.87 ± 0.06	0.35 ± 0.05	0.31 ± 0.09	
2M16235550-1323093	4614	1.34	1.93	-1.97 ± 0.06	0.85 ± 0.24	-0.32 ± 0.23	0.34 ± 0.11	0.58 ± 0.24	
	4538	1.19	1.67	-1.90 ± 0.06	0.71 ± 0.12	0.07 ± 0.11	0.68 ± 0.12	0.47 ± 0.20	
2M10095022+0159202	4827	1.61	1.85	-1.84 ± 0.07	0.71 ± 0.28	0.28 ± 0.25	0.08 ± 0.13	0.27 ± 0.22	
	4569	1.31	1.67	-2.07 ± 0.06	0.76 ± 0.22	0.41 ± 0.18	0.50 ± 0.20	0.41 ± 0.24	
2M21300316+1213286	4834	1.27	1.95	-2.07 ± 0.07	0.71 ± 0.28	0.58 ± 0.25	0.58 ± 0.12	0.35 ± 0.21	
	4573	0.89	1.67	-2.24 ± 0.06	0.80 ± 0.23	0.63 ± 0.18	0.36 ± 0.21	0.41 ± 0.45	
2M14055319+5227233	4862	1.82	1.79	-1.97 ± 0.07	0.30 ± 0.29	0.64 ± 0.25	0.51 ± 0.13	0.38 ± 0.14	
	4506	1.17	1.67	-2.22 ± 0.06	0.80 ± 0.19	0.58 ± 0.16	0.57 ± 0.18	0.40 ± 0.22	
2M18225322+0113105	4915	3.18	1.4	-1.78 ± 0.06	0.83 ± 0.25	-0.15 ± 0.22	0.50 ± 0.12	0.42 ± 0.17	
	4512	2.43	1.54	-2.11 ± 0.06	0.75 ± 0.19	0.01 ± 0.16	0.18 ± 0.17	0.32 ± 0.26	
2M13205580+1231196	5033	2.04	1.73	-2.03 ± 0.07	0.71 ± 0.34	0.88 ± 0.26	0.55 ± 0.14	0.43 ± 0.11	
	4510	1.06	1.67	-2.37 ± 0.06	0.81 ± 0.22	0.48 ± 0.18	0.56 ± 0.20	0.59 ± 0.26	

2M15144943-0141354	5267	2.66	1.55	-1.68 ± 0.06	0.68 ± 0.33	0.56 ± 0.24	0.34 ± 0.14	0.05 ± 0.32
	4457	1.21	1.67	-2.22 ± 0.06	0.76 ± 0.10	0.12 ± 0.10	0.50 ± 0.11	0.32 ± 0.31
2M12221630+1407311	5315	2.34	1.64	—	—	—	—	—
	4596	1.18	1.67	-1.98 ± 0.06	0.76 ± 0.19	0.52 ± 0.16	—	0.28 ± 0.33
2M07573998+4038029	5351	2.76	1.52	—	—	—	—	—
	4466	1.15	1.67	-2.37 ± 0.06	0.84 ± 0.02	0.42 ± 0.02	0.46 ± 0.04	0.28 ± 0.12
2M17172331+4256556	5448	2.93	1.47	—	—	—	—	—
	4511	1.36	1.67	-2.27 ± 0.06	0.95 ± 0.21	0.20 ± 0.17	0.09 ± 0.19	0.36 ± 0.37
2M17175037+4313460	5604	3.21	1.39	—	—	—	—	—
	4597	1.42	1.66	-2.28 ± 0.06	0.84 ± 0.22	0.47 ± 0.18	0.57 ± 0.21	0.57 ± 0.30
2M11464977+2746407	6180	3.79	1.23	—	—	—	—	—
	4435	0.77	1.66	-2.35 ± 0.06	0.79 ± 0.14	0.55 ± 0.12	0.60 ± 0.14	0.16 ± 0.32
2M14514157+1623464	—	—	—	—	—	—	—	—
	4381	0.72	1.66	-2.25 ± 0.07	0.75 ± 0.25	0.43 ± 0.19	0.72 ± 0.19	0.44 ± 0.21
2M16563200+1024306	—	—	—	—	—	—	—	—
	4542	1.27	1.67	-2.15 ± 0.06	0.95 ± 0.07	0.91 ± 0.08	0.40 ± 0.09	0.38 ± 0.11
2M13091378-0230485	—	—	—	—	—	—	—	—
	4581	1.34	1.67	-2.34 ± 0.07	0.86 ± 0.25	0.68 ± 0.19	0.62 ± 0.23	0.53 ± 0.23

The bulk of this analysis has focused on the data available through DR12, however the recent release of DR13 (SDSS Collaboration et al., 2016) allows us to internally compare the ASPCAP results. DR13 uses the same data from DR12 but with improved data reduction techniques, an updated linelist, new spectral grids for dwarfs and giants, as well as an updated calibration of abundances (García Pérez et al., 2016, others in prep.). All cool CEMP candidates ($T_{\rm eff} < 4600$K, [Fe/H]< -1.8, and [C/Fe]$> +0.7$) from DR13 were selected and cross-matched with our initial sample of 13 CEMP candidates from DR12 in Table 2.7. Three stars, 2M02121851+4923143 (Group A), 2M11584435+5518120 (Group B), and 2M14571988+1751501 (Group B) were identified by ASPCAP as CEMP candidates in both DR12 and DR13. The stellar parameters, as well as the abundances of Fe and C for these three stars are in excellent agreement between DR12 and DR13. The N and O abundances are additionally consistent to within the error bars, however a small degree of scatter in the abundances is seen for the two Group B stars. Since our Group B stars were affected by persistence in DR12 and that DR13 sought to address the persistence problem, this variance is likely the result of the new analysis. Examining the individual visit spectra from DR13, we note the persistence appears to be corrected for three of the six Group B targets, including 2M11584435+5518120 and 2M14571988+1751501. The higher data quality in DR13 makes these two stars prime candidates for follow up analysis.

The 10 remaining DR12 CEMP candidates between Groups A, B, and C are not identified as CEMP in DR13. With the exception of the two coolest Group A stars, 2M15312547+4220551 and 2M00114258+0109386, the remaining Group A and Group B candidates remain classified as carbon-enhanced in DR13, but their DR13 metallicities are above the [Fe/H]≤ -1.8 limit imposed for CEMP. Offsets in metallicity on the order of 0.2 dex appears typical between DR12 and DR13 for this selected sample. Similar offsets in [O/Fe] are observed suggesting the [O/H] abundance between DR12 and DR13 is robust, however the the derivation of the N abundance is suffering from pipeline limitations in DR13.

We identify 16 new CEMP candidates in DR13 that were not included in our sample from DR12. Eight of these stars have $T_{\rm eff} > 4600K$ or fail to meet the metallicity or carbonicity requirements for the CEMP classification when adopting their DR12 stellar parameters and abundances. Abundances and/or stellar parameters were not reported in DR12 for the remaining eight stars identified as CEMP by DR13. A future study into the nature of the DR13 CEMP candidates is warranted.

2.7 Conclusions

This work serves as the first exploration of CEMP stars using H-band spectra. Investigation of the DR12 APOGEE ASPCAP database for CEMP candidates has resulted in 13 stars with [C/Fe]> 0.7 and [Fe/H]< -1.8. Within this sample, six stars (Group A) were identified to have "clean" spectra, free of flat fielding and persistence, and well matched synthetic spectra. The remaining seven stars showed moderate to strong evidence of persistence and/or poorly matched synthetic spectra, decreasing the likelihood that ASPCAP can identify the CEMP signatures. Temperature effects, abundance upper-limits, molecular blends, and other systematics have additionally complicated the accuracy of the ASPCAP abundances. These stars serve as a caution when inspecting the APOGEE database for metal-poor and chemically peculiar stars. A model atmospheres analysis and MOOG spectrum syntheses were performed for each of the Group A candidates, confirming their CEMP classification, but raising further questions on their nitrogen and α-element enrichments and the reliability of the ASPCAP abundances at low metallicity.

The extent of the ASPCAP data has additionally allowed for a preliminary study into the nature of these stars. Low α-abundances are observed for two Group A stars, encouraging the possibility their origins are in an accreted dwarf galaxy, and a binary fraction of 16% (one star) was determined for Group A by exploring the radial velocity variations between individual visits. A higher binary fraction was expected if the dataset was comprised solely of CEMP-s stars (Carney et al., 2003; Starkenburg et al., 2014; Hansen et al., 2016b), indicating our sample may contain a more diverse and revealing group of stars in the framework of Galactic chemical evolution. Follow up observations of these objects are required to determine the $s-$ and $r-$ process abundances necessary for further sub-classification. An inceptive look into DR13 has additionally uncovered up to 16 CEMP candidates worth investigating with similar methods presented here for the DR12 spectra.

The depth of information accessible through APOGEE spectra exceeds what is currently available in the ASPCAP database. Careful and targeted analyses of this large database have and will continue to yield new insight into both fundamental and unique astrophysical processes, Galactic structure, chemistry, and evolution.

2.8 Line Lists

Table 2.8 Atomic lines and derived log abundances for the α-elements Mg, Si, S, and Ca

Element	Wavelength (Å)	χ(eV)	log gf	2M153...	2M001...	2M213...	2M181...	2M163...	2M021...
Mg I	15745.017	5.931	-0.262	—	—	—	—	—	5.93
	15753.189	5.932	-0.388	5.0	4.8	5.4	5.8	5.6	5.9
	15770.055	5.933	-0.387	4.8	5.0	5.4	5.7	5.6	5.9
Si I	15893.2	7.125	-2.49	—	5.2	—	5.4	5.2	—
	15963.99	7.029	-2.319	—	4.7	—	5.9	5.7	—
	16064.4	5.954	-0.566	—	4.7	5.7	5.9	5.7	6.1
	16099.18	5.964	-0.168	—	—	5.6	5.8	5.6	5.9
	16168	5.954	-0.937	<5.5	4.9	5.8	5.9	5.7	6.0
	16685.33	5.94	-0.14	5.0	5.2	5.5	5.7	5.6	5.9
S I	15426.48	8.7	-0.238	—	—	—	—	—	<5.6
Ca II	16201.5	4.535	0.092	—	—	—	—	—	<4.7

Table 2.9: Molecular features and log abundances used to derive C, N, and O.

Element	Wavelength Interval (Å)	2M153...	2M001...	2M213...	2M181...	2M163...	2M021...
C from atomic C I line	16895.03	7.7	7.6	7.5	7.5	7.7	7.4
O from OH lines	15283-15287	—	—	—	7.9	—	7.7
	15560-15570	—	—	—	8.0	—	—
	15571-15578	—	—	7.4	—	—	7.5
	15721	—	—	—	8.2	—	7.9
	15724	—	—	—	7.7	—	7.1
	15731	—	—	—	8.1	—	7.9
	15735	—	—	—	7.9	—	7.6
	15760	—	—	—	—	—	7.3
	15777-15780	7.0	7.2	—	7.2	7.4	7.2
	15783	—	—	—	—	—	7.4
	15895-15899	—	—	—	7.7	8.1	7.6
	15913-15919	6.8	—	—	7.9	7.6	7.6
	16057	7.0	—	7.6	—	7.6	7.4
	16060	7.2	—	7.6	—	—	7.4
	16069	6.6	—	—	—	—	7.6
	16074	7.0	—	—	—	—	7.4
	16079	—	—	—	—	—	7.6
	16184	—	—	7.9	7.9	—	—
	16187-16200	—	—	—	7.9	—	7.3
	16208	—	—	7.6	7.6	7.7	7.5

	16224	—	—	7.6	7.6	—	7.6
	16235-16238	—	—	—	—	—	7.7
	16270	—	—	—	—	—	7.3
	16362-16384	—	6.8	—	—	—	7.0
	16523-16533	—	6.8	—	—	—	7.3
	16616-16650	—	7.1	7.3	7.3	—	7.2
	16653-16677	—	7.2	—	—	—	7.5
	16706-16716	—	7.2	—	—	—	7.5
	16731-16739	—	—	—	—	—	7.4
	16758-16761	—	—	—	—	7.8	—
	16763-16766	—	—	—	—	7.4	7.1
	16770	—	6.8	—	—	8.0	7.3
	16836-16847	7.2	7.2	—	—	—	7.3
	16875-16880	—	7.0	—	—	—	7.4
	16888-16893	6.6	7.0	—	—	—	7.3
	16897-16911	—	—	—	—	7.5	7.5
N from CN lines	15193	—	—	7.4	6.9	7.4	—
	15186-15206	—	6.5	—	—	—	6.6
	15220	—	6.6	7.3	6.9	7.3	6.7
	15226	—	6.8	—	—	7.3	6.9
	15229-15234	—	6.7	—	—	7.3	6.8
	15252-15261	—	6.6	7.0	6.8	7.0	6.7
	15263-15270	—	—	7.3	6.9	—	—
	15301	—	6.5	7.4	7.0	7.3	6.7

15320-15336	—	6.6	7.2	6.9	7.2	6.7
15365-15372	6.3	—	7.4	7.0	7.4	—
15377	6.2	—	7.2	—	7.2	—
15399	6.9	—	7.2	—	7.2	—
15401	6.5	—	7.1	6.9	7.1	6.7
15404	6.5	—	7.3	—	7.3	—
15414	6.7	—	7.4	—	7.4	—
15426-15432	6.2	—	7.2	—	7.2	—
15438	6.5	6.2	6.9	7.0	6.9	6.6
15440	6.5	6.2	6.9	—	6.9	6.6
15443	6.5	—	7.4	—	7.4	—
15451	—	—	7.2	—	7.2	—
15453-15459	—	—	6.8	—	6.8	—
15480-15484	—	—	6.8	—	6.8	—
15486	—	—	7.2	—	7.2	—
15512	—	6.4	7.4	—	7.4	6.8
15534	—	—	7.1	—	7.1	—
15543-15553	—	—	7.2	—	7.2	—
15598	—	6.5	—	6.9	—	6.8
15617	—	6.6	—		—	6.8
15669	—	6.4	—	7.0	—	6.8
15699-15713	—	—	—	7.0	7.1	—
15674-15687	—	6.4	—	—	7.2	6.7
15727-15731	—	—	—	6.9	—	—

15738-15743	—	—	—	6.9	—	—
15771-15787	—	6.6	—	6.4	—	—
15896-15899	—	6.2	—	—	—	6.4
15907-15927	—	6.4	—	—	—	6.7

Chapter 3

New Frontiers: The *Pristine* Survey and StarNet

3.1 Introduction

The field of Galactic archaeology is rapidly expanding as new technologies, observational and computational, emerge, allowing us to reach fainter magnitudes, probe the chemistry of new regions of the Galaxy, analyse data faster, determine higher precision abundances, and develop more complete GCE models.

Large sky surveys like the Wide-Field Infrared Survey Explorer (WISE, Wright et al., 2010), the Two Micron All-Sky Survey (2MASS, Skrutskie et al., 2006a), the HK survey (Beers et al., 1985), the Hamburg ESO survey (HES Christlieb et al., 2002), and the narrow-band *Skymapper* survey (Keller et al., 2007) have generated large samples of metal-poor stars ((e.g., Schlaufman & Casey, 2014; Aoki et al., 2013a; Yong et al., 2013a; Casey & Schlaufman, 2015; Matsuno et al., 2017) which provide observational constraint on the nucleosynthetic yields of Type II supernovae (SNe) (Ishigaki et al., 2014), on the primordial IMF (Susa et al., 2014), on early galactic chemical evolution (GCE) processes (Sneden et al., 2008; Roederer et al., 2014a; Yoon et al., 2016), and highlight the chemical properties of EMP stars based on their present-day location in the Galaxy (Cayrel et al., 2004; Frebel et al., 2006; Bonifacio et al., 2009; Carollo et al., 2010, 2012; An et al., 2013; Starkenburg et al., 2013; Skúladóttir et al., 2015; Howes et al., 2015, 2016; Koch et al., 2016; Lamb et al., 2017).

An emergent new large sky survey is the *Pristine* survey (Starkenburg et al.,

2017). *Pristine* is a narrow-band, photometric survey focused around the metallicity sensitive Ca II H & K absorption lines, conducted with the MegaCam imager at the Canada-France-Hawaii Telescope (CFHT). Photometric metallicities are derived though an empirical relationship which compares the flux from the CaHK filter to SDSS colors. The most metal-poor candidates selected from photometry are then targeted with medium resolution ($R \sim 3500$) optical spectroscopy at the 2.5-meter INT and 4.2-meter WHT, with spectroscopic metallicities and carbonicities derived by the FERRE code (Allende Prieto et al., 2006). This process has been found to be remarkably efficient with success rates of 70% for finding stars with [Fe/H]< -2.5 and 22% for stars with [Fe/H]< -3.0 (Youakim et al., 2017), compared to previous studies like HES and *Skymapper* which have recovery fractions of EMP stars on the order of a few percent. The most exciting objects found though medium-resolution observations are then re-observed with high-resolution, high-SNR spectroscopy to determine detailed chemical abundances. Through *Pristine* it is expected to find one star with [Fe/H] ≤ -4.0 for every ~ 100 stars with [Fe/H] ≤ -3.0 or roughly ~ 15 UMP stars over the ~ 1000 deg^2 footprint, vastly increasing the sample of known stars with [Fe/H] ≤ -4.0.

While these spectroscopic surveys provide a rich homogeneous database of stellar spectra, fast and robust data analysis pipelines are needed to process these large samples. Pipelines like FERRE rely on least squares fitting routines which compare an observed spectrum (i.e. from the APOGEE survey) to a grid of synthetic spectra generated from detailed stellar model atmospheres and radiative line transfer calculations (e.g., Koesterke et al., 2008; Mészáros et al., 2012), ultimately estimating stellar parameters ($T_{\rm eff}$, $\log(g)$, [Fe/H]) and chemical abundances (Mészáros et al., 2015; Cunha et al., 2015; Pérez et al., 2016). Other pipelines such as the Cannon (Ness et al., 2015) and Cannon-2 (Casey et al., 2016) are data-driven generative models which use a quadratic polynomial function to translate input stellar parameters into spectra through least-squares fitting to a training set of stellar spectra with known stellar parameters. The Cannon was originally trained on APOGEE DR10 spectra and was able to derive stellar parameters to similar precision as the APOGEE data.

The homogeneity of these large spectroscopic surveys make them ideal for machine learning applications. Von Hippel et al. (1994) and Singh et al. (1998) were the first to apply artificial neural networks to stellar classification; Bailer-Jones et al. (1997) and Bailer-Jones (2000) later developed a neural network to use synthetic stellar spectra to derive stellar parameters. While these projects were successful, limited

training sets and computational limitations at the time were prohibitive in advancing these tools as viable data analysis options. Modern computing resources coupled with improvements in the usability and performance of machine learning software has led to more robust architectures.

StarNet (see Appendix A; Fabbro et al. in prep.) is a novel deep neural network model developed to analyse SDSS-III APOGEE DR13 spectra. StarNet can produce stellar parameters (temperature, gravity, and metallicity) with similar or better precision as the APOGEE pipeline when trained on APOGEE spectra. Unique to StarNet is the ability to derive stellar parameters when trained on synthetic stellar spectra to similar or better precision as the APOGEE pipeline. Additionally, the residuals between StarNet and APOGEE parameters are smaller than differences between APOGEE parameters and those derived from optical high resolution spectral analyses (see Figure A.13). When compared to other data-driven methods like the Cannon and Cannon-2, StarNet is able to achieve the same level of precision as the other methods with the benefit of highly decreased computing time. StarNet can process the complete APOGEE DR10 dataset in less than a day while the Cannon requires a few weeks of computing time. The exceptional precision and efficiency of StarNet when trained on real or synthetic data is encouraging in the prospect of applying this tool to other spectral surveys like *Pristine*.

Throughout my MSc program, I have been an active member in both the *Pristine* survey and the StarNet project. A magnificent attribute to these projects is that they are multi-institutional and multinational collaborations, allowing for a diverse set of individuals to actively contribute, cultivating a rich environment of unique ideas, methodologies, and skill sets which as translated to well-rounded and comprehensive works. However, during this process, it is possible that individual contributions are concealed and obscured, making it difficult to assign credit where credit is due. The following sections outline my personal contributions to these projects, as well as establish a framework for future work.

3.2 Contributions to the *Pristine* Survey

The success of the *Pristine* survey can be attributed to the performance of the survey's photometric metallicity estimations, coupled with the target selection for the spectroscopic follow-up programme. When carrying out the spectroscopic observations, the most interesting targets must be identified from the thousands of objects

with estimated photometric metallicities to optimize the use of telescope time and to maximize the potential scientific return. In the current structure of the *Pristine* programme, this responsibility of target selection is left to the telescope operator.

The medium resolution ($R \sim 3500$) spectroscopic campaign for *Pristine* has largely been fulfilled at the 2.5m Isaac Newton Telescope (INT) located at the Roque de Los Muchachos Observatory ORM) in La Palma, Canary Islands, using the blue sensitive EEV10 detector on the Intermediate Dispersion Spectrograph (IDS). Through two observing runs at the INT, spanning a total of 15 nights in May 2016 and May 2017, I selected and observed 110 and 117 targets, respectively. The 110 stars observed in May 2016 comprise 53% of the 210 star sample used by Youakim et al. (2017) to perform the first refinement of the *Pristine* selection criteria for finding extremely metal-poor stars ([Fe/H] ≤ -3.0). The 117 targets observed in May 2017 have been analysed by FERRE and will contribute to the continued calibration of the *Pristine* selection criteria. A preliminary analysis of these stars show that 55 stars (47%) have confirmed spectroscopic [Fe/H]< -2.5 and 6 stars (5%) have confirmed spectroscopic [Fe/H]< -3.5.

The six new EMP stars are strong candidates for high-resolution spectroscopic observations as these stars sample the metal-poor tail of the Galactic halo metallicity distribution function (An et al., 2013; Fernández-Alvar et al., 2017) which has shown a variety of interesting element ratios in previous studies (e.g., Cohen et al., 2013; Roederer et al., 2014b, 2016). High-resolution spectra are required to determine their detailed chemical abundances, including the alpha, odd-Z, and especially the neutron capture elements, enabling the classification of the CEMP stars, and opening the possibility of identifying new members from other chemically peculiar groups like $i-$process enhanced (Dardelet et al., 2015; Roederer et al., 2016) and $r-$process rich stars (Aoki et al., 2010; Roederer et al., 2014a; Hill et al., 2016). Furthermore, detailed abundances allow for comparison to predicted yields from SNe Type II, provide constraint on the variety of progenitor masses, fall-back models, explosion energies and Galactic chemical evolution models (e.g., Cohen et al., 2004; Norris et al., 2007; Heger & Woosley, 2010; Tominaga et al., 2014; Côté et al., 2016a,b; Choplin et al., 2017).

3.3 Contributions to StarNet

The accuracy of the parameters returned by StarNet is limited in the quality of the training data. When StarNet is trained on the ASPCAP stellar parameters, intrinsic errors in the ASPCAP pipeline are implicitly propagated throughout the results. One option to examine the fidelity of the APOGEE StarNet results is to compare them to optical analyses. Stellar parameters and abundances for individual stars derived through optical analysis typically have higher fidelity due to the availability of high resolution optical spectrographs, access to more spectral lines, and higher confidence in optical atmosphere models (see Sneden et al., 2004; Gilmore et al., 2012b; Venn, 2012; Aoki et al., 2013b; Yong et al., 2013b; Howes et al., 2014; Roederer et al., 2014c; Lamb et al., 2015).

Investigating the ability of StarNet to reproduce the optical parameters for the APOGEE benchmarks, all stars from the APOGEE DR13 database with the "Calibration-Cluster" and "Standard Star" flags were selected to create a group of benchmark stars with ASPCAP parameters. Optical parameters were obtained through direct matching of the APOGEE identifier/2MASS identifier (Skrutskie et al., 2006b) to stars in the Pastel 2016 catalog (Soubiran et al., 2016), supplemented with the available data from the references in Mészáros et al. (2013) and Holtzman et al. (2015). A systematic investigation of the collected data revealed numerous stars with incomplete optical parameters in the literature (e.g., missing $T_{\rm eff}$, $\log g$, or [Fe/H]), or incomplete IR parameters in the ASPCAP database (e.g., presumably due to data acquisition issues such as low S/N or persistence). These stars were removed from our benchmark sample, as well as targets in the APOGEE database with a high RV scatter between individual visits (which usually indicates a potential binary system). Figure A.13 compares the stellar parameters for our final sample of 103 optical benchmark stars (tabulated in Appendix B with references).

Examining Figure A.13, there are small offsets between the DR13 ASPCAP and the optical values for all three stellar parameters. However, the offsets are similar to the standard deviation of the errors in the optical analyses. We consider this very good agreement, and do not investigate these intrinsic dispersions further. On the other hand, an examination of Fig.s A.3, A.10, and A.13 suggests that the scatter in the StarNet stellar parameters is much smaller than the systematic errors between the ASPCAP FERRE and optical analyses. Comparing the DR13 ASPCAP results to the StarNet predictions generated from high S/N APOGEE spectra (Figure A.3)

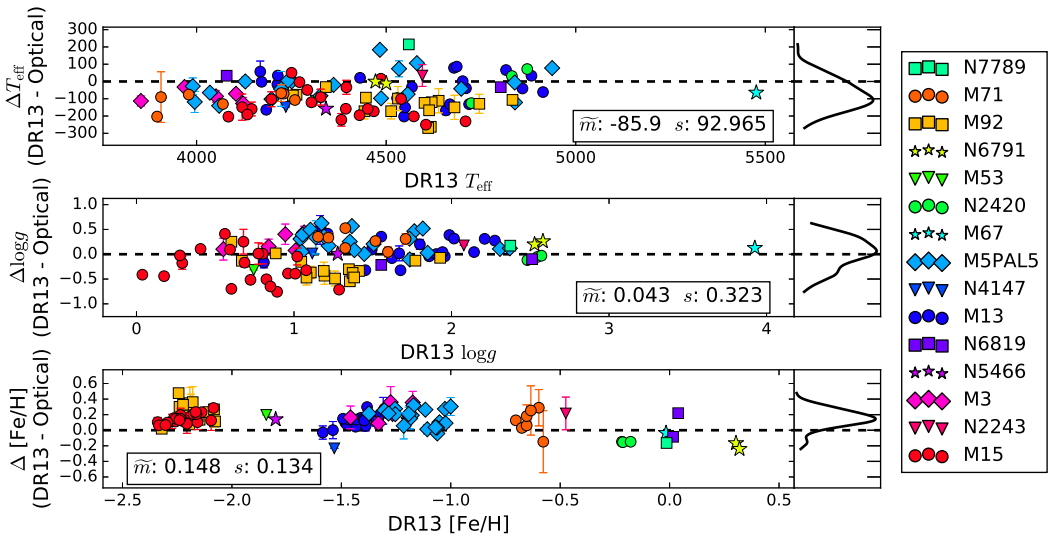

Figure 3.1 Comparison of DR13 stellar parameters for 103 stars in clusters to their corresponding optical parameters sourced from the literature. When multiple literature sources are available for a particular star, the average of the reported parameters is shown with the error bars defined by the standard deviation of the optical data. See Table B.1 for a list of the literature references. The mean value ($\tilde{\rm m}$) and standard deviation (s) are calculated in each panel, as in Fig. A.2.

and to the values from optical analyses (Figure A.13), suggests the precision in the StarNet results is a factor of ~ 3 better for $T_{\rm eff}$, $\log(g)$, and [Fe/H]. When StarNet is trained on synthetic spectra and compared to DR12 (Figure A.10), the scatter shows a factor of ~ 2 improvement over the DR13 vs. optical analyses. While a component of this improvement may reside in higher quality of DR13 analysis over DR12, the comparison of Figures A.10 and A.13 demonstrates that when StarNet is trained on synthetic spectra it is capable of reproducing, if not improving on, the accuracy of an optical analysis.

Regardless of whether StarNet is trained and tested on observed or synthetic data, the scatter in our residuals is well within the intrinsic systematic errors of the ASPCAP or optical stellar parameters. This indicates that StarNet model is sufficient at this time, and can provide a new and exciting tool for the efficient analyses of existing and future spectroscopic surveys. My objective for future projects is to expand StarNet by training on optical synthetic spectra as a contribution to the analysis of the *Pristine* survey. This work will ideally be applied to future spectroscopic surveys as well, such as WEAVE (WHT Enhanced Area Velocity Explorer, Dalton et al., 2012, 2014, 2016), 4MOST (4-metre Multi-Object Spectroscopic Telescope, de Jong et al., 2016), PFS (Subaru Prime Focus spectrograph, Takada et al., 2014), and MSE (Maunakea Spectroscopic Explorer, McConnachie et al., 2016), significantly increasing the robustness, efficiency, and scientific impact of these projects.

Appendix A

Stellar Spectral Analysis with Deep Neural Networks

The following sections are the working draft of Stellar Spectral Analysis with Deep Neural Networks *by S. Fabbro, T. O'Briain, S. Bialek, K.A. Venn, C. Kielty, F. Jahandar, and S. Monty which has been submitted to the Monthly Notices of the Royal Astronomical Society. Please refer to Chaper 3 for a discussion of my personal contributions to this work.*

A.1 Abstract

Spectroscopic surveys like *Pristine* require fast and efficient analysis methods to maximize scientific impact. Here we apply a deep neural network architecture to analyze both SDSS-III APOGEE DR13 and synthetic stellar spectra. We devise a neural network model (StarNet) that can produce the stellar parameters (temperature, gravity, and metallicity) with similar or better precision as the APOGEE pipeline when trained on APOGEE spectra. When trained on synthetic data, StarNet can reproduce the stellar parameters for both synthetic and APOGEE spectra, over all signal-to-noise, with similar precision to training on APOGEE spectra. Parameter uncertainties are consistent with the scatter in the predictions when predicted errors for individual visit spectra are compared to the scatter in the residuals between predictions on individual visits and the combined spectra for the same objects. Furthermore, the residuals between StarNet and APOGEE parameters are no greater than the differences between APOGEE results and optical high resolution spectral

analyses for a subset of benchmark stars. StarNet is additionally compared against other data-driven methods. When trained on similar datasets, StarNet and the Cannon 2 show similar behaviour, however StarNet performs poorly on small training sets, like those used by the original Cannon. We examine the predictive power of spectral features that contribute to the stellar parameter determinations via partial derivatives of the StarNet model, for both observed and synthetic spectra. While StarNet was developed using the APOGEE database (observed spectra and corresponding ASSET synthetic data with similar normalization functions), we suggest that this technique should be applicable to other spectral surveys.

A.2 Introduction

Spectroscopic surveys provide a homogeneous database of stellar spectra that are ideal for machine learning applications. A variety of techniques have been studied in the past two decades, ranging from the SDSS SEGUE stellar parameter pipeline using a decision tree architecture between spectral matching to a synthetic grid and line index measurements (e.g., Lee et al., 2008; Allende-Prieto et al., 2008; Yanny et al., 2009; Lee et al., 2011a), to the detailed algorithms employed for analysis of the Gaia spectroscopic data (e.g., Smiljanic et al., 2014; Recio-Blanco, 2016, 2017; Pancino et al., 2017).

The use of artificial neural networks in astrophysical applications has a history going back more than 30 years, with pioneering research in stellar classification by authors such as Von Hippel et al. (1994) and Singh et al. (1998). In Bailer-Jones et al. (1997) and Bailer-Jones (2000), a neural network was applied to synthetic stellar spectra to predict the effective temperature $T_{\rm eff}$, surface gravity $\log(g)$, and metallicity [Fe/H], similar to the goals of this paper. More recently, dramatic improvements have occurred in the usability and performance of algorithms implemented in machine learning software. Combined with increased computing resources and the availability of large data sets, this has led to more complex neural network architectures that have proven to be pivotal in difficult image recognition tasks and natural language processing. The earlier attempts at neural networks for stellar spectra analyses (e.g., Bailer-Jones, 2000; Manteiga et al., 2010) would train the neural network weights on synthetic spectra, and test the model on synthetic spectra. In this paper, we examine several cases of training on synthetic spectra and predicting stellar parameters on both synthetic and observed spectra, or training and predicting on only observed

spectra in a purely data-driven approach.

The methods we use follow the supervised learning approach, where a representative subset of stellar spectra (either synthetic or observed) with known stellar parameters is selected. This subset can be further divided into a "reference set", where the neural network learns the mapping function from spectra to stellar parameters, and a "test set" used for ensuring the accuracy of predictions. Once the network model is trained (i.e. with fixed network parameters), the stellar parameters can be predicted for the rest of the sample. The stellar parameters we consider for this spectral analysis are the effective temperature ($T_{\rm eff}$), surface gravity ($\log(g)$), and metallicity ([Fe/H]).

In this paper we present StarNet: a convolutional neural network model applied to the analysis of stellar spectra. We introduce our machine learning methods in Section 2, and evaluate our model for a set of synthetic data in Section 3. As an exercise of its effectiveness, we apply StarNet to the APOGEE survey in Section 4 (DR13 and earlier data releases when appropriate), and compare the stellar parameters to those from the APOGEE pipeline(s). In Section 5, we discuss the success of our StarNet results to other stellar analyses, and confirm that neural networks can significantly increase the robustness, efficiency, and scientific impact of spectroscopic surveys.

A.3 Machine Learning Methodology

Supervised learning is an interesting approach for the prediction of stellar parameters from spectra. It is necessary to have a "training set" in which, for each input spectrum, there are known stellar parameters. A supervised learning model is then capable of developing a function that transforms the input spectra to the output values. The learned function can then ideally be used to predict the output values of a different dataset. The particular form of this function and how it is learned depends on the model used; we focused our efforts on implementing a neural network model.

A.3.1 Neural Networks

A Neural Network (NN) consists of a collection of interconnected nodes arranged in layers: an *input layer* (i.e. the input data), a number of *hidden layers*, and an *output layer* (i.e. the prediction). The hidden layers are able to form non-linear combinations of an input vector, $\mathbf{x}$, to produce an output vector, $\mathbf{y} = h(\mathbf{x}; \mathbf{w}, \mathbf{b})$. At each layer l,

the output in function of the previous layer is given by:

$$\mathbf{y}^l = g(\mathbf{w}^l \mathbf{y}^{l-1} + \mathbf{b}^l)$$

where g is an *activation function*, $\mathbf{w}$ is a matrix of trainable weights representing the connections between the nodes in two adjacent layers, and $\mathbf{b}$ is a bias vector. The first layer input is simply the initial input: $\mathbf{y}^0 = \mathbf{x}$. Depending on the architecture of the NN, there may be several hidden layers, each composed of multiple nodes that receive the output from the previous layer and compute input values for the following layer. The more hidden layers a NN is composed of, the deeper the model is.

Common activation functions include the sigmoid function and the Rectified Linear Unit (ReLU):

$$g(z) = \max(0, z)$$

which allow for the weights to be adjusted to complex non-linear data (Chen et al., 1990). The ReLU function was used in this implementation for all layers except for the last output layer.

A.3.2 Convolutional Neural Networks for Stellar Spectra

Inspired from recent studies of deep neural networks on stellar spectra (Li et al., 2017; Wang et al., 2017), we have focused our analysis on deep learning methods. The selected architecture for our StarNet model is a Convolutional Neural Network (CNN) and is shown schematically in Fig. A.1. This architecture is composed of a combination of fully connected layers and 1-dimensional convolutional layers. Fully connected layers are the classical neural network layers that apply weights to each input value to compute an output. In the case of a convolutional layer, a series of filters are convolved across the length of the input data and would give more importance of local features. Throughout the training phase the network learns filters that are activated most strongly when detecting specific features, thus producing a collection of *feature maps*. Using two successive convolutional layers allows the second of the two to convolve across the previous layer's feature map and enables the model to learn higher order features.

Maxpooling layers are a non-linear down-sampling technique typically used in CNNs to decrease the number of free parameters and to extract the strongest features from a feature map. In a maxpooling layer, a window moves along the feature map

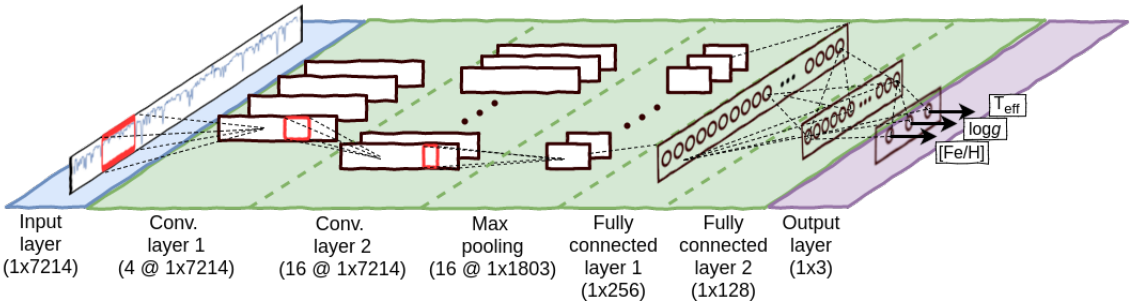

Figure A.1 The current StarNet CNN model composed of 7 layers. The first layer is solely the input data followed by two convolutional layers with 4 and 16 filters (in successive order), then a max pooling layer with a window length of 4 units followed by 3 fully connected layers with 256, 128, and 3 nodes (again, in successive order). The last layer is the output layer.

generated by each of the filters in the previous convolutional layer in strides of length equal to the length of the window, extracting the maximum value from each sub-region. These pools of maxima are then passed on to the following layer. The use of maxpooling layers allows the model to extract the most important features in the input data while ignoring sections that do not hold useful information. This reduces the amount of time required for each forward propagation as well as the time required for the model to reach convergence.

The combination of convolutional and fully connected layers allows the model to find relationships between individual flux values in a spectrum and the output stellar parameters as well as correlations between sections of the spectrum and the stellar parameters. This technique strengthens StarNet's ability to generalize its predictions on spectra of a wide range of signal-to-noise (S/N) and across a larger stellar parameter space. Details of the StarNet model itself are further discussion in Section A.5.3.

A.3.3 Training and testing of the Model

Before training the model, the reference set is split into a training set and a "cross-validation" set. To improve the prediction abilities of a NN, training is performed through a series of forward and back propagation iterations, using "batches" of the training set. The forward propagation is the model function itself: at each layer, weights are applied to all of the input values, and at the output layer, a prediction is computed. These predictions are then compared to the target values through a *loss function*. In our StarNet model, a mean-squared-error loss function computes the loss between predictions and target values.

The purpose of the back-propagation is to minimize the loss function and therefore reduce the error between the prediction and target values. This minimization is often a variant of a gradient descent algorithm. The optimization technique used in StarNet is the Adaptive Moment Estimation (ADAM) optimizer (Kingma & Ba, 2014), a stochastic gradient descent algorithm with adaptive individual learning rates based on the gradient moments. The model weights are updated following each batch forward propagation. Therefore, the weights are adjusted multiple times per iteration, which is defined as the forward and back propagation done over the entire training set.

Following each iteration, the cross-validation set is sent through a single forward

Table A.1 Stellar parameter distribution of the ASSET synthetic spectra grid

Class		T_{eff}	$\log(g)$	**[M/H]**	**[C/M]**	**[N/M]**	**[α/M]**
GK	Min.	3500	0	-2.5	-1	-1	-1
	Max.	6000	5	0.5	1	1	1
	Step	250	0.5	0.5	0.25	0.5	0.25
F	Min.	5500	1	-2.5	-1	-1	-1
	Max.	8000	5	0.5	1	1	1
	Step	250	0.5	0.5	0.25	0.55	0.25

propagation where the outputs are predicted and compared against the target values. This set is not used for training, but only to ensure that the model is not over-fitting the training set. When the cross-validation predictions stop improving, the training will be stopped. Using a cross-validation set to avoid over-fitting is common practice in machine learning applications (Gurney, 1997).

For our models, the loss function minimum is usually reached after 20-25 iterations, although this can vary greatly depending on the complexity of the model used. The training of the StarNet model reached convergence in an amount of time that depended on the size of the training set and the model architecture: for ∼41,000 spectra it converged in 30 minutes, using a 16 cores Virtual Machine.

When the training stage reaches convergence, the weight values are frozen. The estimated model is evaluated on a test set of spectra with a wide range of S/N. All tests of StarNet are quantified with location (mean, median) and spread (standard deviation, mean absolute difference) summary statistics on the residuals with a test set of known parameters.

A.4 Training and testing StarNet with simulated spectra

As previously mentioned, machine learning methods have been applied to stellar spectra in the past (Bailer-Jones, 2000) using synthetic data for training and testing. Synthetic spectra provide an extremely useful initial application to evaluate the StarNet model. Since we later evaluate StarNet on the APOGEE observed data sets, we applied StarNet to synthetic spectra generated by the APOGEE collaboration.

The synthetic spectra used by the APOGEE consortium have been generated using

MARCS and ATLAS9 model atmospheres, as described in Mészáros et al. (2012), and the radiative transfer code "ASSET" (Koesterke et al., 2008). These synthetic spectra were continuum normalized in the same way as the observed APOGEE spectra to facilitate a closer match between synthetic and observed spectra. Provided in a publicly available 6D spectral grid compressed with Principal Components Analysis (see Table A.1 for parameter distribution), we have used these synthetic spectra as a first test of StarNet. To sample at any desired location within the grid, we used a third order interpolation.

In all instances of training StarNet on synthetic data, we added Gaussian noise to try to match S/N $\approx$ 30 up to noiseless spectra. Each spectrum was used several times in a particular training process and therefore different amounts of noise were added to match the multiple visit behaviour. The addition of noise was necessary to secure a flat behaviour of the residuals when testing on observed spectra (see Section 4.5). We found that StarNet did not overfit the high S/N data, and thus we could generalize its predictive capabilities to lower S/N spectra.

As a first test, we generated 300,000 synthetic spectra via random sampling of the stellar parameters within the limits of the ASSET grid. Of these spectra, 260,000 were randomly selected as the reference set. A subset of these (224,000 or 86% of the reference set) were used to train StarNet. The remaining 36,000 spectra from the reference set were used to cross-validate the model following each training iteration.

The remaining 40,000 spectra were used as a test set, and the residuals between StarNet's predictions and the generated parameters are shown in Fig. A.2. For all three predicted stellar parameters, the variances of the residual distributions are inversely proportional to the S/N. At [Fe/H]<-1.9 and lower S/N there is a distinct trend where absorption features are not as prominent and the noise effectively cause StarNet's predictions to be similar for all of these stars.

A.4.1 Stellar Parameters Prediction Precision

To evaluate the errors in StarNet's predictions, it is necessary to understand how the output of the model is affected by the uncertainties in the input spectra ($\mathbf{x}$). Treating the entire network as a vector valued function $\mathbf{h}(\mathbf{x}, \mathbf{w}) = (h_{\mathrm{T_{eff}}} h_{\log g} h_{\mathrm{[Fe/H]}})$, the Jacobian matrix of a given star, fixed StarNet model, and stellar parameter j is given by:

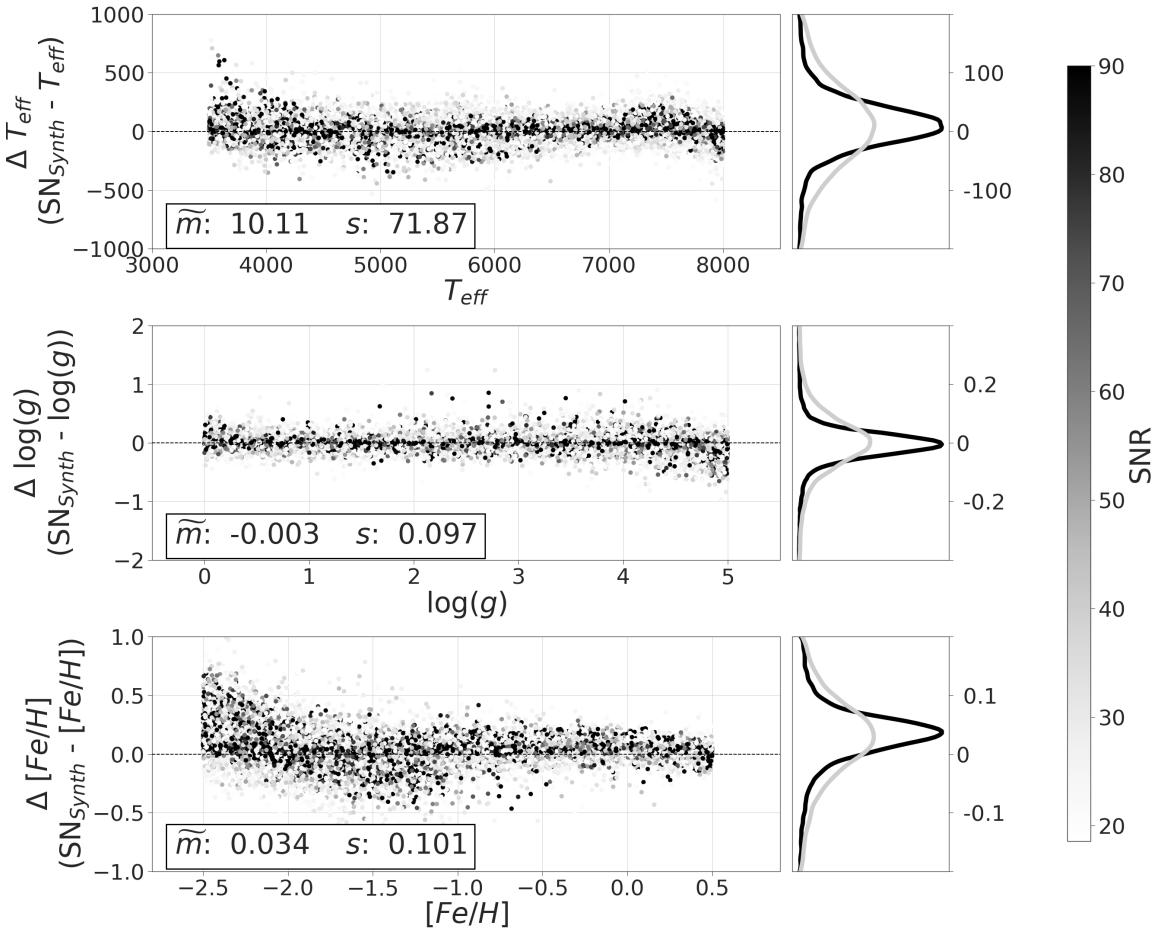

Figure A.2 StarNet predictions residuals with the generated stellar parameters for a test set of 40,000 ASSET synthetic spectra (Koesterke et al., 2008). StarNet was trained with 224,000 synthetic spectra randomly sampled from the ASSET synthetic grid. Distributions of the residuals are shown on the right (black for synthetic spectra with S/N $>$ 80, gray for S/N $<$ 60). The mean value ($\tilde{m}$) and standard deviation (s) are calculated in each panel.

$$\mathbf{J}(\mathbf{x}, \mathbf{w}) = \left(\frac{\partial h_j}{\partial x_1} ... \frac{\partial h_j}{\partial x_n} \right) (\mathbf{x}, \mathbf{w})$$

Here we assume that each spectrum is accompanied by a corresponding error spectrum, $\mathbf{e_x}$ (of the same length). Propagating the error spectrum with the Jacobian of that spectrum results in an approximation of the statistical uncertainty, σ_{prop}, of the output prediction for each stellar parameter computed as the dot product:

$$\sigma^2_{\text{prop}} \approx \mathbf{J}^2 \cdot {\mathbf{e_x}}^2$$

Besides restricting our approximation to the small error domain, we do not compute the error propagated from the StarNet CNN model training for practical reason. To compensate for this deficit, we derived an empirical intrinsic scatter on the synthetic test data which we add in quadrature with the propagated uncertainty, giving us our total estimated uncertainty:

$$\sigma = \sqrt{\sigma^2_{\text{prop}} + \sigma^2_{\text{int}}} \tag{A.1}$$

This intrinsic scatter term is slightly dependent on the region of the parameter-space in which the predicted parameter lies, reflecting the capacity of the physical model to match observed spectral features.

A.5 StarNet Applications to APOGEE spectra

The survey has been carried out at the 2.5-m Sloan Foundation Telescope in New Mexico, and covers the wavelength range from 1.5 to 1.7 microns in the H band, with spectral resolution R = 22,500. Targets are revisited several times until S/N $\geq$ 50 is reached. All visits are processed with a data reduction pipeline to 1-D, and wavelength calibrated before being combined. The individual visits, unnormalized combined spectra, and normalized combined spectra are all recorded into the publicly-available APOGEE database.

The APOGEE Stellar Parameters and Chemical Abundances Pipeline (ASPCAP) is a post data reduction pipeline tool for advanced science products. This pipeline relies on the nonlinear least squares fitting routine FERRE (Pérez et al., 2016), which compares an observed spectrum to a grid of synthetic spectra generated from detailed stellar model atmospheres and radiative line transfer calculations. This fitting process

estimates stellar parameters ($T_{\rm eff}$, $\log(g)$, [Fe/H]) and abundances for 15 different elements (C, N, O, Na, Mg, Al, Si, S, K, Ca, Ti, V, Mn, Fe and Ni), further calibrated with comparisons of these stellar parameters to those from optical spectral analyses of individual stars in a wide variety of star clusters (Mészáros et al., 2015; Cunha et al., 2015): see Appendix for more details.

A.5.1 Pre-processing of the Input Data

Table A.2 Cuts applied to APOGEE DR13 for the training and test set

Cut	**Visit Spectra**	**Combined Spectra**
No cuts	559484	143482
`ASPCAPFLAG`	327594	92983
`STARFLAG`	142875	45474
4000K $<$ T_{eff} $<$ 5500K	127357	39017
$v_{scatter}$ $<$ 1km/s	120879	37311
[Fe/H] $>$ -3	120879	37311
log(g) != -9999	113956	35591
Combined SNR $>$ 200	53135	Not applicable
Partition into reference and test sets	**Training set**	**Cross-Validation Set**	**Test set**
	41000	3784	21037

To test StarNet's ability on observed spectra, StarNet was trained using the APOGEE spectra and ASPCAP DR13 stellar parameters. Due to the fact that supervised learning methods can only be as accurate as their training set, then any errors in the stellar parameters used in the training set will impact the model's ability to determine the parameters in the test set. Thus, to minimize the propagation of the FERRE errors on our StarNet results, we limit the range of our datasets. As an example, Holtzman et al. (2015) advise caution when using stellar parameters of stars at cooler temperatures, $T_{\rm eff} < 4000$K, due to a higher degree of uncertainty, as well as hotter stars, where the spectral features are less defined. For this reason, the dataset was reduced to stars with $4000\text{K} \leq T_{\rm eff} \leq 5500\text{K}$. The APOGEE team have also flagged specific stars and visits for a variety of other reasons. Stars from the DR13 dataset with either a `STARFLAG` or `ASPCAPFLAG` were removed from the dataset, which includes stars contaminated with persistence (see Jahandar et al., 2017; Nidever et al., 2015), stars that were flagged for having a bright neighbour, or having parameters near the parameter grid edge of the synthetic models. Furthermore, stars with a radial velocity scatter, $v_{\rm scatter}$, greater than 1 $\mathrm{km\,s^{-1}}$ or [Fe/H] < -3 dex were also removed.

Implementing these restrictions to the *reference set* allowed the neural network to be trained on a cleaner dataset and learn from more accurate stellar parameters, while placing these restrictions on the *test set* was an attempt to maximize the validity of ASPCAP stellar parameters to be used when comparing with StarNet predictions. All of these cuts to the APOGEE dataset are summarized in Table A.2.

In addition to the restrictions mentioned above, the reference set only included visit spectra from stars where the combined visit spectrum S/N > 200. ASPCAP stellar parameter accuracy is known to degrade with S/N (Ness et al., 2015; Casey et al., 2016). However, using high S/N combined spectra as the training input resulted in over-fitting spectra with high S/N. To compensate for this issue, StarNet was trained with the individual visit spectra, while using the stellar parameters obtained from the combined spectra as the targets. This step allowed the model to be trained on and predict with the lower S/N spectra with higher precision. Limiting our training sample to higher S/N spectra was also practical; currently StarNet is not able to weight the input spectra according to the noise properties of the spectra at training. When combining various data sets, which we will address in future work, it might become more critical, but is less relevant for the current analysis.

The last phase of the data pre-processing was normalizing the spectra. Both

The Cannon 2 (Casey et al., 2016) and ASPCAP have implemented independent continuum normalization techniques, and in addition the APOGEE DR13 spectra were continuum normalized in particular spectral regions. The theoretical spectra are similarly normalized to facilitate proper matching with the data. StarNet adopts a simple and linear normalization when training and testing on APOGEE individual visit spectra, i.e., the spectra were split into blue, green, and red chips, and each chip was divided by the median flux value in that chip. The three chips were then combined to create a single spectrum vector. Given that normalization procedures usually do not need external information, our simple approach is also testing the NN's capacity compared to a more physically-driven continuum analysis.

It has been suggested (e.g., Casey et al., 2016) that the ASPCAP continuum normalization techniques will produce inconsistently normalized spectra at lower S/N. This is a potential limitation of StarNet when it has been trained on synthetic ASSET spectra, since these spectra were similarly normalized without the addition of noise beforehand. Any non-linearities in continuum normalization would be excluded from the synthetic spectra dataset. If this inconsistent normalization is indeed a problem it could create an inherent mismatch between a synthetic spectrum and a low S/N APOGEE spectrum of identical stellar parameters, thereby leading to erroneous stellar parameter estimates. Note that this would also be a limitation of the analysis carried out by ASPCAP.

This potential continuum removal bias was the reason StarNet adopted a simple normalization method. Further analysis is required to determine the full impact of continuum normalization in this NN approach.

A.5.2 Training and testing StarNet with APOGEE spectra

StarNet has been trained and tested on the ASPCAP stellar parameters ($T_{\rm eff}$, $\log(g)$, [Fe/H]) corresponding to individual visit spectra and combined spectra, respectively. As discussed previously, this included stars from the APOGEE DR13 dataset with the cuts outlined in Table A.2. There were 17,149 stars with S/N $>$ 200 that met these requirements, of which 2651 were used as part of the test set and 14,498 stars - containing 44,784 individual visits - were used as StarNet's reference set; this is slightly less than 10% of the total APOGEE DR13 dataset. A subset of these individual visits (41,000 or 92% of the reference set) were randomly selected for the training set. The remaining 3,784 visit spectra were used to cross-validate the model

following every forward propagation during training. No significant deviations were found between random selections for training and cross-validation samples.

Once trained, StarNet was applied to the test set containing both high and low S/N combined spectra for prediction. StarNet's predictions are compared to ASPCAP parameters in Fig. A.3. For the high S/N spectra, StarNet predictions show excellent agreement. For the lower S/N spectra, there are more a deviations between StarNet predictions and ASPCAP parameters. For example, at high temperatures, StarNet is predicting lower effective temperatures. The quality of the model predictions depend on the number of stars spanning the parameter space of the training set, and we note that there are fewer stars with $T_{\rm eff}$> 5200K. Similarly, there are few stars at low metallicities, [Fe/H] < -1.7, and therefore applying StarNet to the most metal-poor stars results in a larger amount of scatter. This "sample size bias", as seen in these two regions, reinforces the need for large training samples.

Another potential source of error in the predictions at high temperatures and low metallicities lies in the spectra themselves. In these regions, the spectral features are less defined which can result in inaccurate predictions for two reasons: the neural network may not be able to locate the most important features it has been trained to find, and the ASPCAP training parameters have a larger degree of uncertainty.

StarNet was then applied to 148,724 stars in the APOGEE DR13 database. This inference step is very fast, taking about 1 minute of CPU for the whole data set. The short amount of time required to make these predictions is a huge advantage for rapid data reduction of large spectral surveys.

StarNet predictions for 99,211 spectra are shown in Fig. A.4, where stars with ASPCAP $T_{\rm eff}$, $\log(g)$, or [Fe/H] values of -9999 are presumed to be M dwarf stars and were removed (see Section A.6.2). StarNet predictions were compared against each other along with being over-plotted with isochrones to show the expected trend in the parameter relationships. Four isochrones with different metallicities ([Fe/H] = $0.25, -0.25, -0.75$ and -1.75) were generated from the Dartmouth Stellar Evolution Database (Dotter et al., 2008) with an age of 10 Gyr and [α/Fe]=0. Also found in Fig. A.4 is StarNet's reference set of 14,498 stars highlighted to show the spread and abundance of these training stars across the parameter space.

To analyze the StarNet model self-consistency, we predicted both from the individual visits spectra, and combined spectra from each object. These results were compared against each other in Fig. A.5. Objects with four or more individual visits were selected and the scatter was calculated in the residuals between StarNet

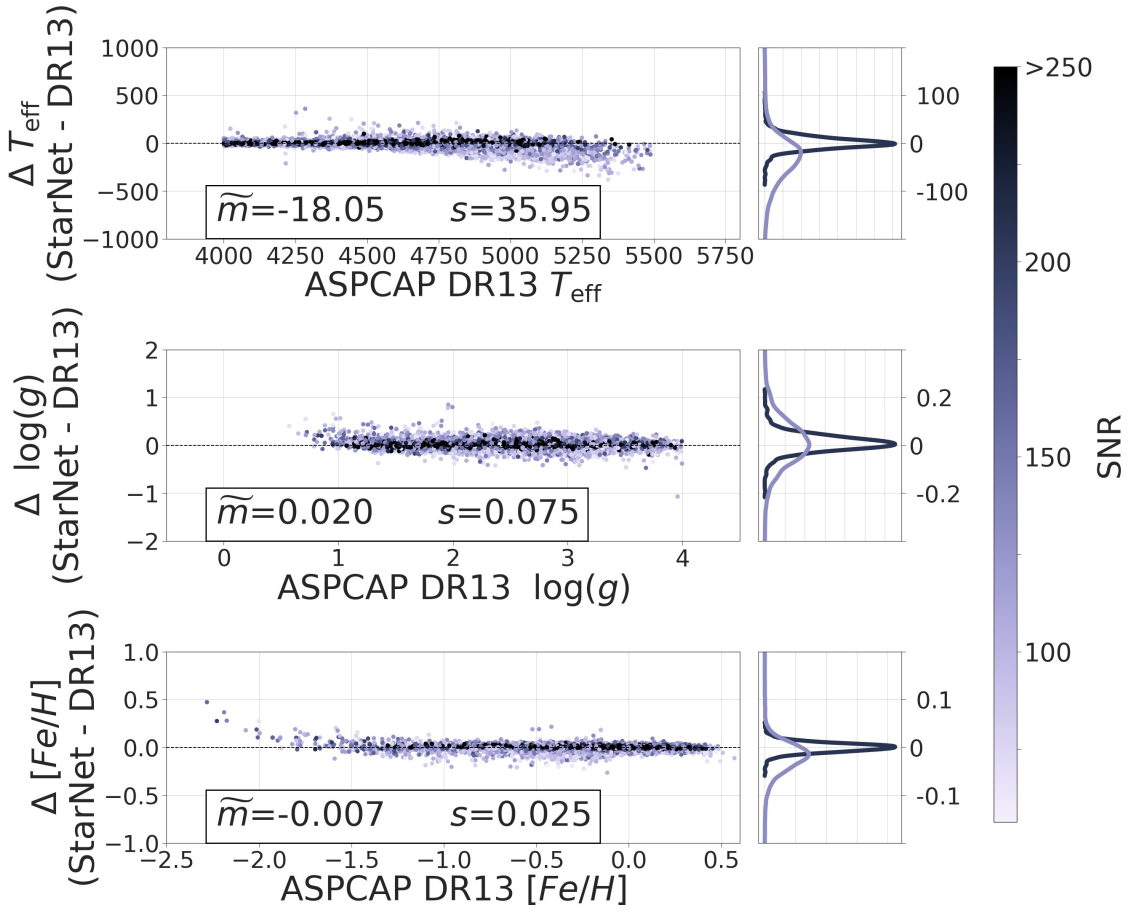

Figure A.3 Residuals of StarNet predictions and ASPCAP parameters for a test set of 21,037 combined spectra over a large range of S/N. StarNet was trained on 41,000 individual visit spectra from the APOGEE DR13 dataset, with no bad flags. As the S/N decreases, small deviations are seen for the hotter stars, stars at the lower end of the surface gravity range, and the most metal-poor stars, which are likely due to a sample size bias in the training set. The mean value ($\tilde{m}$) and standard deviation (s) are calculated in each panel, as in Fig. A.2.

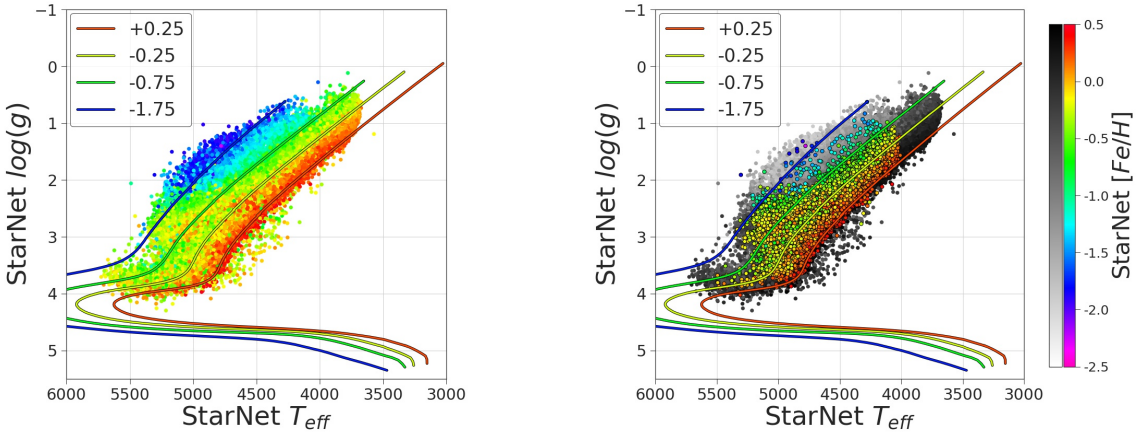

Figure A.4 Stellar parameters of StarNet predictions for 99,211 stars, showing log(g) parameters against T_{eff} across a wide range of [Fe/H] (left panel). StarNet's reference set of 14,498 stars is highlighted on top of the 99,211 stars (right panel). Over-plotted are 10Gyr isochrones (using Dotter et al., 2008) with [Fe/H] values found in the upper left corner of the figure.

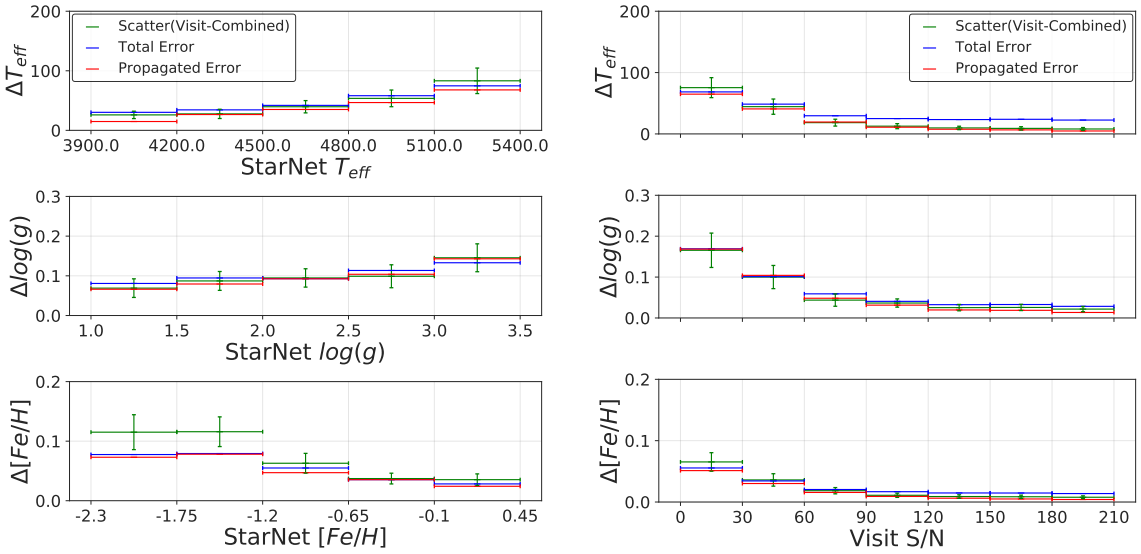

Figure A.5 Comparison of StarNet predictions on individual visits against StarNet predictions for the corresponding combined spectra. In the left panel the comparisons are made against the parameter-space and for each parameter bin, 100 spectra were randomly selected. At low metallicities and higher T_{eff}, larger deviations are found between the predictions for the individual visits and combined spectra. In the right panel the comparisons were made against the S/N of the individual visits, where each S/N bin contained 230 spectra. In both plots the "Scatter (Visit-Combined)" is the standard deviation in the residuals between the predictions for the individual visits and combined spectra for objects with more than 4 individual visits. The "Propagated Errors" are the error terms due to the error spectrum, whereas the "Total Errors" are the propagated error and "Intrinsic Scatter" terms (see Section A.4.1) added in quadrature. StarNet was trained on 41,000 individual visit spectra from the ASPCAP DR13 dataset, with no bad flags.

predictions for the individual visits and combined spectra of the same object.

For each stellar parameter bin, the mean value for 100 objects is shown in Fig. A.5 (left panel), whereas there were 230 objects in each S/N bin (right panel). The propagated and total errors shown are discussed in Section A.4.1. When comparing StarNet predictions for the individual visits to those for the combined spectra, the results are quite consistent across the majority of the parameter-space, though as discussed previously, there is a noticeable increase in the deviations at lower metallicities ([Fe/H] $<$ -1.2 dex) and higher temperatures ($T_{eff} >$ 5100K). Also as expected, the scatter increases at lower S/N, although only marginally until S/N$\lesssim$60. Even at the lowest values (S/N $\sim$ 15) the results are quite good. The ability to predict well on lower

S/N spectra is largely due to the fact that StarNet was trained on individual visits - rather than combined spectra - with high validity stellar parameters.

A.5.3 Model Selection

Deep learning architectures, such as StarNet, typically involve experimentation and tuning of hyper-parameters neither related to the physical model or the NN model, in order to converge to an effective model. We tried to automate the final selection of hyper-parameters as follows: to select the optimal model architecture, a hyper-parameter optimization was run in two stages. During the first stage, the number of convolutional layers, fully connected layers, filters, and nodes were varied randomly along with the length of the filters, the pooling window size, and the learning rate. This allowed the optimizer to test different combinations of the number of convolutional and fully-connected layers with a variety of other hyper-parameters to ensure that each combination could reach its maximum predictive potential. The same training and cross-validation sets as described in Section A.5.1 were used during the training of these models, and the same test set (discussed in Section A.5.2) was used to test each model. The metric used for model comparisons was the "Mean Squared Error" (MSE) between the target and predicted parameters. To have each parameter weighted equally, the parameters were normalized to have approximately zero-mean and unit variance. An example of the best performing models, evaluated for each combination of layers, were then compared as shown in Fig. A.6.

It was found that increasing the number of layers improved the model predictions, but that there was a plateau in performance when combining two convolutional layers with two fully connected layers. The addition of more layers onto this architecture does not clearly improve the prediction results, while fewer layers led to significantly worse MSE.

A second hyper-parameter optimization was tested, where the number of convolutional and fully-connected layers were fixed at two each, while the remaining hyper-parameters were varied and optimized using a Tree-structured Parzen Estimator (TPE, Bergstra et al., 2011). The model selected by this second stage of hyper-parameter optimization was similar to that shown in Fig. A.1, and therefore this was used as the starting point for our model architecture selection. Small improvements were made until the StarNet model architecture performed consistently with good results.

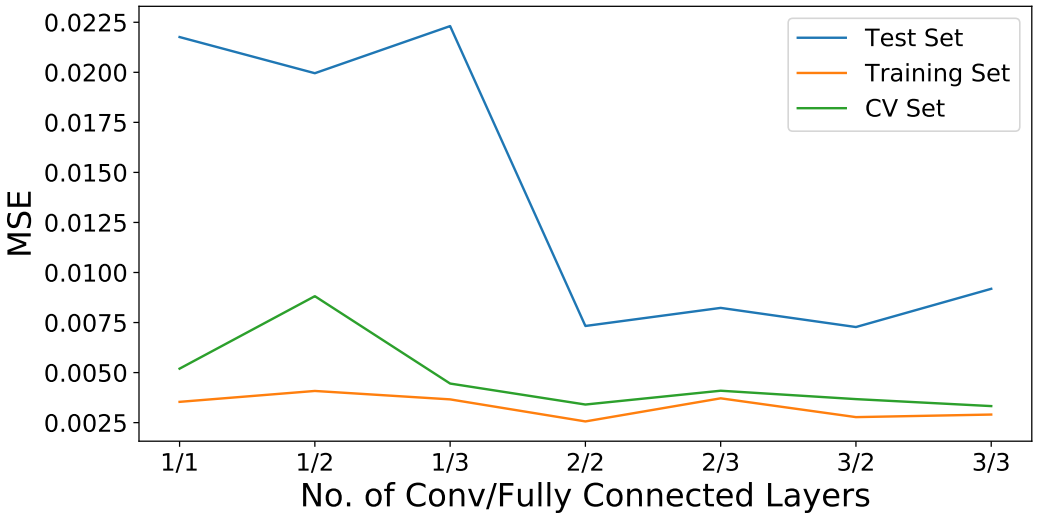

Figure A.6 The Mean Squared Error (MSE) between the normalized target parameters and predictions are plotted against the different combinations of convolutional and fully connected layers during the StarNet model selecting testing.

While simpler models could perform comparably well to the StarNet architecture when trained on synthetic data, it was decided that a single model architecture should be used to train on both synthetic data and APOGEE spectra.

Earlier studies found that applying neural networks to stellar spectra only necessitates at most two hidden layers with fewer nodes than the amount used in StarNet (Bailer-Jones, 2000), but these were applied to a much smaller data sets. Current machine learning methods allow for more complex models to improve performance while still avoiding over-fitting on larger samples. The max pooling layer reduces the degrees of freedom of the model by minimizing the impact of unnecessary weights and therefore simplifying the model function. To speed up convergence for the StarNet model fit, we use the *He Normal* (He et al., 2015) weight initialization, also permitting for convergence of deeper models and eventually enabling the neural network to find more complex features. In short, the *He Normal* initializer and ADAM optimizer allow for a deeper model to reach convergence, while the ReLU activation and max pooling layer simplify the model to an optimal rank of complexity. The use of a cross-validation set is another technique implemented in StarNet to mitigate over-fitting.

A.5.4 Comparisons with The Cannon

The Cannon (Ness et al., 2015) is a data-driven generative model: using stellar parameters as the inputs and the spectra as outputs. It has the same limitations as a traditional supervised learning models, i.e., relying on a reference data set. The Cannon uses a quadratic polynomial function to translate the parameters into spectra and the best-fitting coefficients of the function are found through least-squares fitting. During the test phase, the stellar parameters are determined with another regression step, where the stellar parameters are varied while The Cannon model is fixed, until they produce a spectrum that best matches the observed spectrum.

The Cannon was originally trained on APOGEE DR10 combined spectra from 542 stars in 19 clusters. Using much fewer training examples than the StarNet uses on DR13, The Cannon was still able to predict stellar parameters for the DR10 spectra extremely well. In an effort to compare the two techniques, we trained the same StarNet architecture, labeled StarNet$_{C1}$, on the same 542 stars from DR10. We then applied StarNet$_{C1}$ to 29,891 combined spectra that had both ASPCAP and The Cannon predictions for stellar parameters. These are compared in Fig. A.7, where

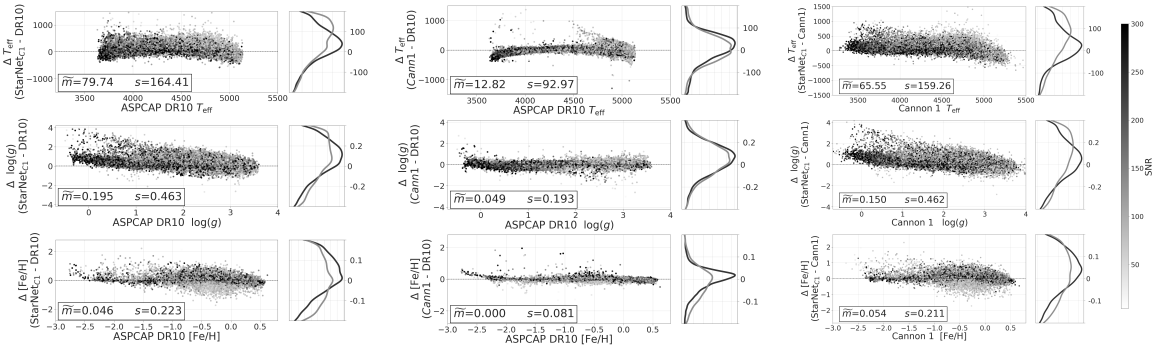

Figure A.7 Comparison of StarNet$_{C1}$ results with ASPCAP (left panel) and StarNet$_{C1}$ results with The Cannon 1 (right panel), as well as comparisons between The Cannon and ASPCAP (center panel). StarNet$_{C1}$ was trained on APOGEE DR10 combined spectra from the same 542 stars that the Cannon used for training. The test set includes combined DR10 spectra that had both ASPCAP and Cannon 1 predictions. Note: axes ranges differ in these plots compared to others in the paper. The mean value (m̃) and standard deviation (s) are calculated in each panel, as in Fig. A.2.

the limitations of the StarNet$_{C1}$ model are clearly seen.

The machine learning method used for StarNet requires a *large* training sample that spans a wide parameter space. Training on 542 combined spectra did not span enough of the parameter range at an accumulated S/N to fit the complex StarNet convolutional neural network. This can also be seen in the large residuals when comparing StarNet$_{C1}$ predictions and ASPCAP DR10 FERRE parameters. Predictions for low S/N spectra show the most significant scatter.

The requirement of large training sets that adequately represent the test set is a limitation of many deep learning method, such as StarNet. However, as larger data sets become available, then these methods can be extremely effective, as discussed in the next Section.

A.5.5 Comparisons with The Cannon 2

The Cannon 2 (Casey et al., 2016) is the continuation of The Cannon project. In addition to the three stellar parameters predicted in StarNet and The Cannon, The Cannon 2 predicts 14 additional stellar labels associated with chemical abundances. The Cannon 2 is also trained on combined visit spectra, but it trains on a larger number of stars. One other difference between the two Cannon methods is the addition of a regularization term in the function at training. This reduces the likelihood of the

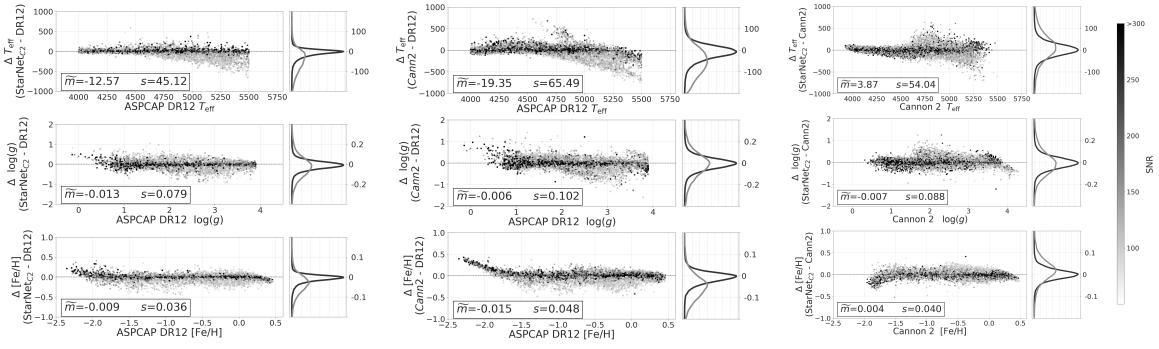

Figure A.8 Comparison of StarNet$_{C2}$ results with ASPCAP (left panel) and StarNet$_{C2}$ results with The Cannon 2 predictions (right panel), as well as comparisons between The Cannon 2 and ASPCAP (center panel), all of them on APOGEE DR12. StarNet was trained on individual visits from similar stars as those used for training The Cannon 2. The test set used to compare the two methods was also similar to that used as The Cannon 2's test set. The mean value (m̃) and standard deviation (s) are calculated in each panel, as in Fig. A.2.

Table A.3 Comparison of StarNet$_{C2}$ and The Cannon 2 for a test set of 85,341 combined spectra from APOGEE DR12. Metrics used are the mean absolute error (MAE), and root mean squared error (RMSE) all with respect to the same stars.

Metric	Parameter	StarNet	Cannon 2
MAE	$T_{\rm eff}$	31.2	46.8
	$\log(g)$	0.053	0.066
	[Fe/H]	0.025	0.036
RMSE	$T_{\rm eff}$	51.2	71.6
	$\log(g)$	0.081	0.102
	[Fe/H]	0.040	0.053

model over-fitting to the training data.

The Cannon 2's training set consisted of stars with $200 < \mathrm{S/N} < 300$, $[\mathrm{Fe/H}] > 3$, $[\mathrm{X/Fe}] < 2$, $[\alpha/\mathrm{Fe}] > -0.1$, $[\mathrm{V/Fe}] > -0.6$, $V_{\rm scatter} < 1$ km s^{-1}, and excluded stars flagged with the APOGEE `ASPCAPFLAG`. These cuts remove stars that have parameter values near the grid edge of the synthetic models - along with other sources of error resulting in poorer ASPCAP parameter determination - but it does not take into account spectra flagged with persistence. The Cannon 2 training set consisted of visits from 12,681 stars.

To make adequate comparisons between the two models, we trained StarNet$_{C2}$ on 39,098 visits from 12,681 stars of DR12 that met similar restrictions as set by The Cannon 2 DR12 training set. The test set used to compare the two methods was made up of 85,341 combined spectra with $T_{\rm eff}$ between 4000K and 5500K and had a $\log(g) < 3.9$, also similar restrictions in The Cannon 2.

We compile the Root Mean Square Error (RMSE) and the Mean Absolute Error (MAE) for an identical test set for both The Cannon 2 and StarNet$_{C2}$ in Table A.3 and they confirm the visual inspections of the residuals in Fig. A.2: StarNet$_{C2}$ is capable of predicting values closer to the ASPCAP stellar parameters.

As seen in Fig. A.2, StarNet$_{C2}$ struggles with accurately predicting the parameters for stars with low metallicity, and hotter stars if the S/N of the spectra is lower. These effects are also seen in The Cannon 2 predictions though. In fact, a comparison of StarNet$_{C2}$ to The Cannon 2 shows that the effect is larger in The Cannon 2, implying that the Cannon 2 is over-predicting at low metallicities even more than StarNet$_{C2}$.

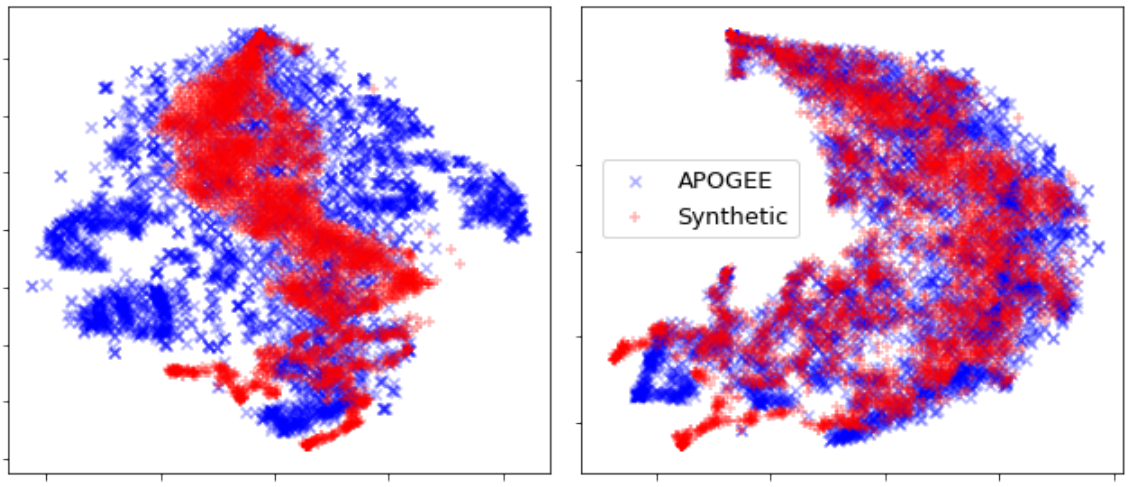

Figure A.9 t-SNE visualization of the synthetic and APOGEE spectra before zero-flux substitution through nearest neighbour interpolation (left) and after (right).

A.5.6 Training with Synthetic Data and Testing on APOGEE Data

Synthetic Gap

Differences in feature distributions between synthetic and observed spectra is usually referred as the *synthetic gap*. To probe the feasibility of training StarNet on synthetic spectra and accurately predicting parameters of observed spectra, it was necessary to secure that the synthetic gap was relatively small. Since each spectrum consists of 7214 data points and represents a point in 7214-dimensional space, one would expect a synthetic and observed spectrum with the same parameters to occupy approximately the same region in this space if the gap was indeed small. Visualizing this space is possible only through dimensionality reduction, so we employed the t-Distributed Stochastic Neighbour Embedding (t-SNE, Maaten & Hinton, 2008), a technique often used in machine learning to find clusters of similar data in a two dimensions.

We randomly selected a subset of 4000 APOGEE DR13 spectra with S/N>200 and known ASPCAP parameters, and 4000 synthetic ASSET spectra generated with those same parameters. After applying t-SNE, a distinct separation could be seen between the synthetic and APOGEE spectra (left image in Figure A.9). Examination the most mismatched spectra showed that there were zero-flux values in wavelength bins along the spectra, a method used in the APOGEE pipeline to flag bad pixels. Unfortunately it is not possible to mask these values at the testing stage with the

current implementation of StarNet, thus a nearest-neighbour interpolation was carried out to smooth over the zeros. Another round of t-SNE revealed closer agreement between synthetic and APOGEE spectra (right image in Figure A.9). These zero-flux values for all APOGEE spectra were fixed before predicting their stellar parameters in subsequent StarNet applications.

While interpolating the zero-point values results in more accurate predictions, it may not be an ideal solution given that we are modifying the data in a way that may not resemble a spectrum without the zero-point values. An alternative method to deal with this issue would be to artificially inject zero-point values in the synthetic spectra during training. This could allow StarNet to learn to give very little weight to these values in the spectrum, mimicking the training process on observed spectra. This method is being explored further; we note that this is not an issue when StarNet is trained on real APOGEE spectra that inherently have these zero-flux values.

Predictions

Using the same method for training StarNet with synthetic spectra from the ASSET code (as described in Section 3), we tested on a dataset of 21,787 APOGEE DR12 spectra containing no bad flags. Comparisons are made to the DR12 results since those were also determined using this ASSET spectral grid (unlike the DR13 results). The results are shown in Fig. A.10.

The distribution in the stellar parameters is similar to the accuracies from the ASPCAP pipeline. For spectra with S/N $>$ 150, the 1σ uncertainties are 51 K in $T_{\rm eff}$, 0.06 in $\log(g)$, and 0.08 in [Fe/H]. For the entire data set of all S/N spectra, the mean errors are only $\sim$2x larger. Unlike training on the observed spectra, there are no significant deviations due to limited training data samples in certain grid regimes.

The addition of noise to the training set allowed StarNet to learn the features of the spectra that impacted the stellar parameter estimates most heavily, and to discount the smaller features in the noiseless synthetic spectra that would not be detectable in noisy APOGEE spectra (but which noise would otherwise trick StarNet into thinking were there). Tests were conducted varying the maximum levels of noise added to the training set, and it was found that a minimum S/N of 20 decreased the residuals in predictions as much as possible before plateauing. Noise addition to the model at the training stage is a first tentative to include the uncertainties in the physical model, as well as limiting the degrees of freedom in the NN model.

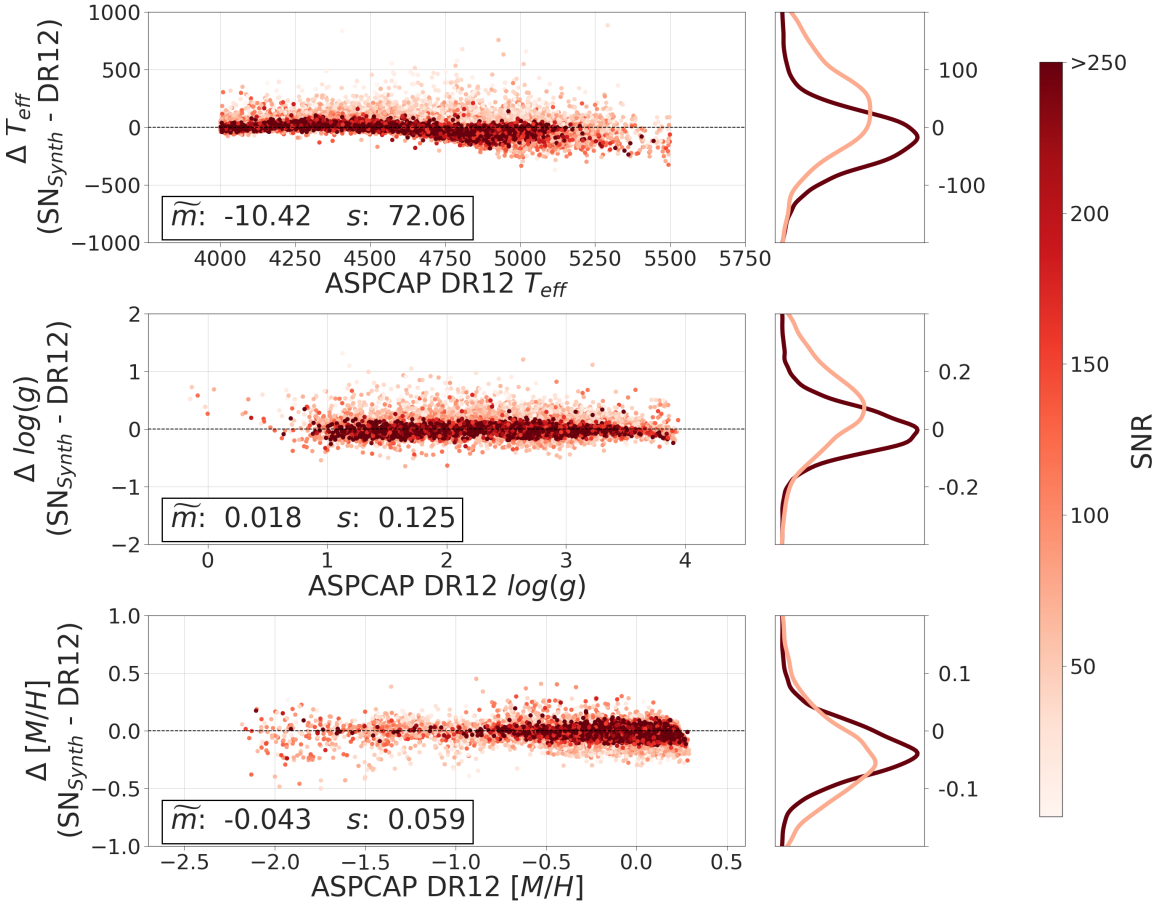

Figure A.10 Residuals of StarNet predictions and ASPCAP parameters for a test set of 21,787 combined spectra from APOGEE without flags. Comparisons were made to DR12 for consistency with our tests using the ASSET synthetic grid (not used for DR13). StarNet was trained on 224,000 synthetic spectra randomly sampled from the ASSET synthetic grid. Distributions about the mean are shown on the right (dark red for observational spectra with S/N > 150, light red for S/N < 100). The mean value (m̃) and standard deviation (s) are calculated in each panel, as in Fig. A.2.

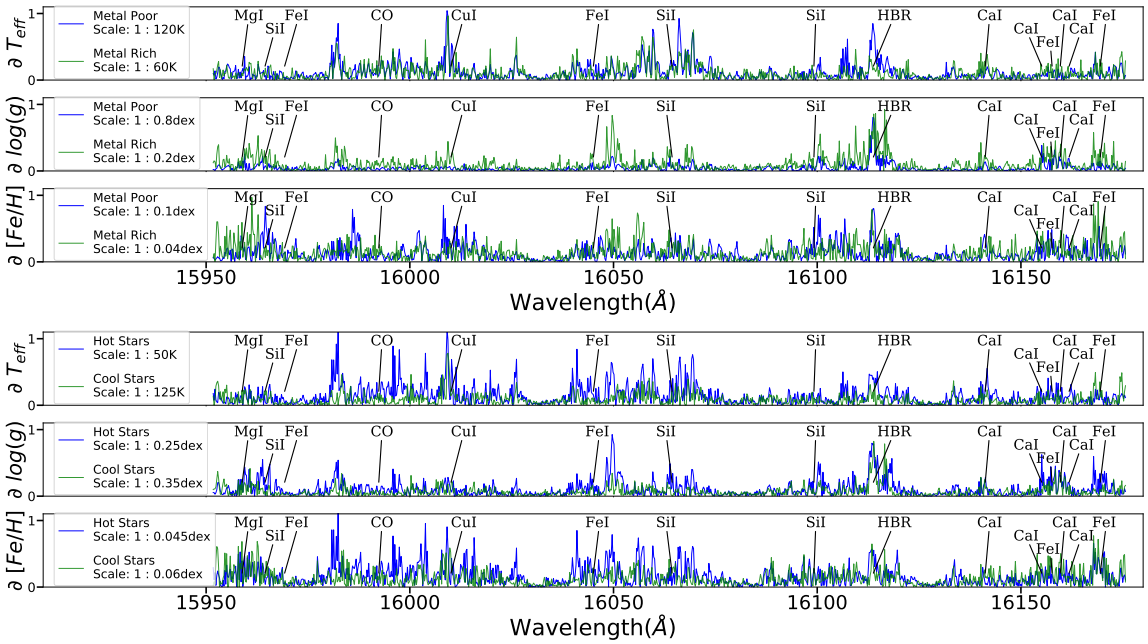

Figure A.11 Partial derivatives of the three stellar output parameters from the StarNet model - trained on APOGEE spectra - with respect to input wavelength bins for a section of the green chip. The partial derivatives of stars from different ranges of the parameter space were compared against each other. Stars with [Fe/H] $>$ 0.0 were compared to those with [Fe/H] $<$ -1.2 (top). Similarly stars with $T_{eff}>$ 5000K were compare to those with $T_{eff}<$ 4300K (bottom). An average Jacobian was calculated from 2000 stars in each parameter range. Note the scale differences when comparing the partial derivatives.

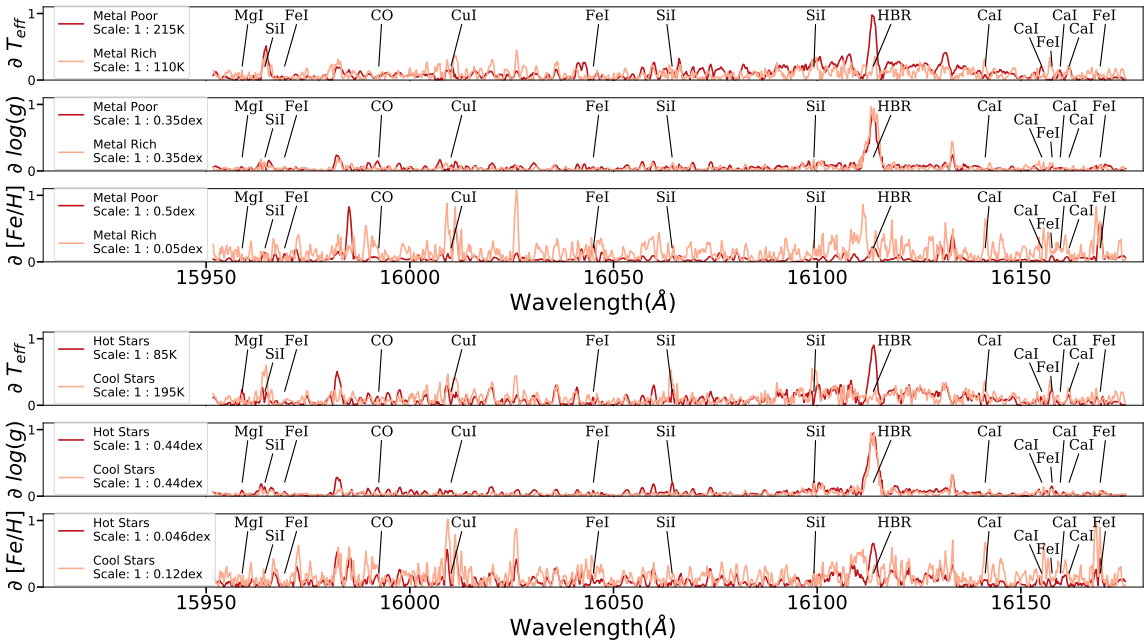

Figure A.12 Partial derivatives of the three stellar output parameters from the StarNet model - trained on synthetic data - with respect to input wavelength bins for a section of the green chip. The partial derivatives of stars from different ranges of the parameter space were compared against each other. Stars with [Fe/H] $>$ 0.0 were compared to those with [Fe/H] $<$ -1.2 (top). Similarly stars with $T_{eff}>$ 5000K were compare to those with $T_{eff}<$ 4300K (bottom). An average Jacobian was calculated from 2000 stars in each parameter range. Note the scale differences when comparing the partial derivatives.

A.5.7 Partial Derivatives

It is possible to examine the spectra to determine which features the neural network is weighting when predicting stellar parameters. We do this by calculating the partial derivatives of each of the outputs (T_{eff}, $\log(g)$, and [Fe/H]) with respect to every input flux value of a particular spectrum to obtain the Jacobian (as described in Section A.4.1).

In Figures A.11 and A.12 - for both StarNet trained on APOGEE DR13 spectra and synthetic spectra, respectively - we show an average of the Jacobian absolute value from 2000 stars located in particular ranges of the parameter space. The Jacobian from metal poor stars were compared against those from metal rich stars. Comparisons were also made between hot and cool stars. We focus on a subsection of the green chip from 15950Å to 16180Å. Some features are labeled from the APOGEE input line list. A few notable features include:

1. Hydrogen Bracket (HBR) lines, which play a significant role in the determination of gravity, but also in the determination of temperature in metal-poor stars

2. Atomic metal lines (e.g., FeI, CaI, CuI) that a play significant role in the determination of temperature and metallicity throughout our stellar parameter range

3. The difference in the role of the atomic metal lines in the synthetic grid, e.g., SiI appears more and CaI appears less significant in the determination of temperature when StarNet is trained on synthetic spectra

4. The importance of unidentified or weaker lines in this spectral region that are not used in the APOGEE window functions and yet play an important role in the determination of all of the stellar parameters from observed spectra

5. The importance of unidentified or weaker lines that play a significant role only in the determination of metallicity for cool stars and metal-rich stars when StarNet is trained on synthetic spectra

None of these features were pre-selected or externally weighted before the neural network was trained. We also compared the partial derivatives for subsets of stars with S/N<60 versus S/N>200, but found no notable differences in the predictive

power. Similar results are seen in the other wavelength regions across the whole APOGEE spectral range.

A.6 Discussion

A.6.1 Optical Benchmark Stars

The accuracy of the parameters returned by StarNet is limited in the quality of the training data. When StarNet is trained on the ASPCAP stellar parameters, intrinsic errors in the ASPCAP pipeline are implicitly propagated throughout the results. One option to examine the fidelity of the APOGEE StarNet results is to compare them to optical analyses. Stellar parameters and abundances for individual stars derived through optical analysis typically have higher fidelity due to the availability of high resolution optical spectrographs, access to more spectral lines, and higher confidence in optical atmosphere models (see Sneden et al., 2004; Gilmore et al., 2012b; Venn, 2012; Aoki et al., 2013b; Yong et al., 2013b; Howes et al., 2014; Roederer et al., 2014c; Lamb et al., 2015).

Investigating the ability of StarNet to reproduce the optical parameters for the APOGEE benchmarks, all stars from the APOGEE DR13 database with the "Calibration-Cluster" and "Standard Star" flags were selected to create a group of benchmark stars with ASPCAP parameters. Optical parameters were obtained through direct matching of the APOGEE identifier/2MASS identifier (Skrutskie et al., 2006b) to stars in the Pastel 2016 catalog (Soubiran et al., 2016), supplemented with the available data from the references in Mészáros et al. (2013) and Holtzman et al. (2015). Figure A.13 compares the ASPCAP DR13 parameters to the optical parameters for these 103 benchmark stars (tabulated in the Appendix with references).

Examining Figure A.13, there are small offsets between the DR13 ASPCAP and the optical values for all three stellar parameters. However, the offsets are similar to the standard deviation of the errors in the optical analyses. We consider this very good agreement, and do not investigate these intrinsic dispersions further. On the other hand, an examination of Fig.s A.3, A.10, and A.13 suggests that the scatter in the StarNet stellar parameters is much smaller than the systematic errors between the ASPCAP FERRE and optical analyses. Comparing the DR13 ASPCAP results to the StarNet predictions generated from high S/N APOGEE spectra (Figure A.3) and to the values from optical analyses (Figure A.13), suggests the precision in the

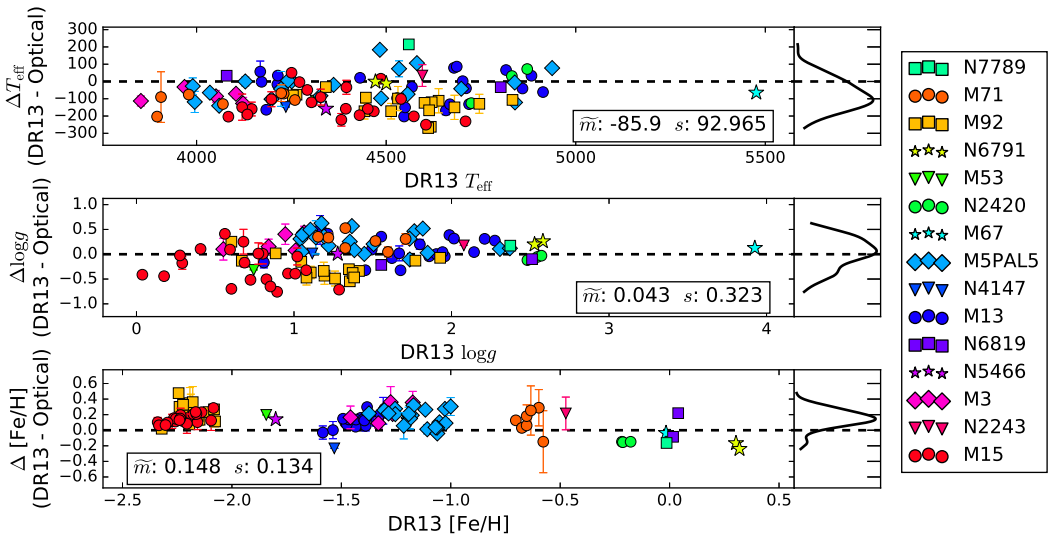

Figure A.13 Comparison of DR13 stellar parameters for 103 stars in clusters to their corresponding optical parameters sourced from the literature. When multiple literature sources are available for a particular star, the average of the reported parameters is shown with the error bars defined by the standard deviation of the optical data. See Table B.1 for a list of the literature references. The mean value ($\tilde{\rm m}$) and standard deviation (s) are calculated in each panel, as in Fig. A.2.

StarNet results is a factor of ~ 3 better for $T_{\rm eff}$, $\log(g)$, and [Fe/H]. When StarNet is trained on synthetic spectra and compared to DR12 (Figure A.10), the scatter shows a factor of ~ 2 improvement over the DR13 vs. optical analyses. While a component of this improvement may reside in higher quality of DR13 analysis over DR12, the comparison of Figures A.10 and A.13 demonstrates that when StarNet is trained on synthetic spectra it is capable of reproducing, if not improving on, the accuracy of an optical analysis.

Regardless of whether StarNet is trained and tested on observed or synthetic data, the scatter in our residuals is well within the intrinsic systematic errors of the ASPCAP or optical stellar parameters. This indicates that StarNet model is sufficient at this time, and can provide a new and exciting tool for the efficient analyses of spectroscopic surveys.

A.6.2 M Dwarfs in DR13

While APOGEE has primarily observed red giant and subgiant stars, DR13 includes spectra for known M dwarfs. These stars are accompanied with a specific Target Flag: "APOGEE MDWARF". Initially, we had not removed these stars from the dataset, and found obvious discrepancies between StarNet results and those provided by ASPCAP DR13. Upon closer examination, we found approximately 5900 stars that resembled a similar trend between StarNet predictions and ASPCAP parameters to the known M dwarfs, but that had not been flagged as M dwarfs. Therefore - for the work in this paper - these stars were removed as well using the following cuts:

((-0.9 < ASPCAP [Fe/H] < 1.0) AND ((StarNet [Fe/H] - ASPCAP [Fe/H]) < -0.4))
OR
((ASPCAP $\log(g)$ > 3.6) AND ((StarNet $\log(g)$ - ASPCAP $\log(g)$) < -0.3))

The ASSET grid that we are using from the DR12 data release does not include synthetic spectra for M dwarfs, and therefore StarNet cannot be trained on synthetic spectra for those stars. StarNet also cannot be trained on the observed spectra at this time since there are too few M dwarf stars in the APOGEE dataset (<1000 flagged, thus similar to the StarNet_{C1} results reported in Section 4.4). We note that our method for flagging M dwarfs is not robust, such that a small amount of RGB stars may have been removed in the process, while some (a few) M dwarfs may still be in our dataset.

A.6.3 Neural Network Considerations

One limitation for neural networks is the necessity of large training sets spanning a wide range of parameter space. The distribution of the stellar parameters in the training set are shown in Figure A.14. From these plots it is quite evident that the amount of stars at high T_{eff}, low metallicities, and small $\log(g)$ are limited compared to those elsewhere in the APOGEE parameter space. As seen in Figs. A.3 and A.7, having fewer stars to train on in these regions results in less accurate predictions when testing on stars in those regions of the parameter space. The model does not have a large enough basis to determine a function that converts spectra into stellar parameters in these regions.

Not only are the number of stars limited in certain ranges of a single parameter, but stars with certain combinations of the three parameters in StarNet's training set have been found to be extremely scarce. As seen in Figure A.4, when StarNet was trained on APOGEE DR13 spectra, there were very few stars with 4500K $\leq T_{eff} \leq$ 5200K, $1 \leq \log(g) \leq 2$, and [Fe/H] $\leq$ -1.6 in the reference set. This issue could be mitigated by adjusting the restrictions set on StarNet's reference set, but would be at a cost on StarNet accuracy.

While stellar observations are limited by time and resources, generating synthetic spectra are limited by computing resources. Being able to produce synthetic spectra that evenly span a parameter space can provide a neural network with large amounts of data to train on and inevitably improve the model's ability to predict in regions which were initially affected by a sample size bias. This is one of the strengths of StarNet and will allow improvements to be made in StarNet's application.

Combining observed spectra with synthetically generated spectra is something that could improve the parameter range of StarNet predictions, while reducing the effect of the synthetic gap. Although ASPCAP DR12 models were produced from ASSET spectra, the DR13 spectral analysis is done with alternative stellar models, therefore this could not be done for the analyses shown in this paper, but is a priority for future applications of StarNet.

Skepticism exists around machine learning due to its historical inaccessibility and complexity, and sometimes perceived as a black box. New developments have improved usability. The training and testing of all of the models used in this paper were performed with the high level neural network library `keras` (Chollet et al., 2015), which provides a high level application program interface to the `tensorflow`

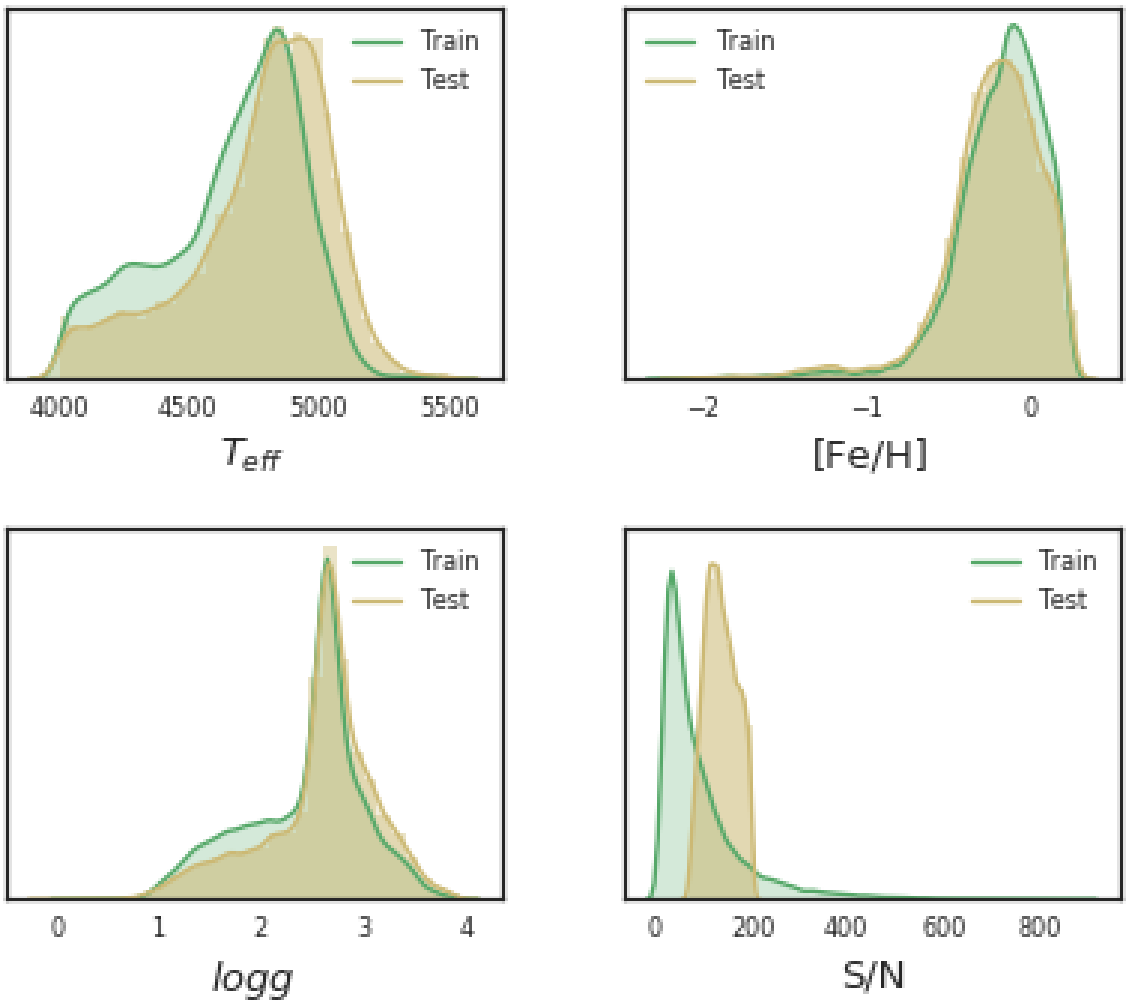

Figure A.14 Distribution of parameters in the StarNet training and test sets.

(Abadi et al., 2015) machine intelligence software package. We provide code to reproduce steps of training and testing on the APOGEE DR13 with StarNet at https://github.com/astroai/starnet.

A.7 Conclusion

We have presented a Convolutional Neural Network model that is capable of determining the stellar parameters $T_{\rm eff}$, $\log(g)$, and [Fe/H] directly from spectra. Our development of this model, StarNet, including training and testing on synthetic and real spectra (both from the APOGEE database). We have implemented an optimization procedure for hyper-parameter tuning, examining the precision in the stellar parameter predictions when developing the StarNet architecture.

By applying this StarNet model to various data releases from the APOGEE survey, we show that it is capable of estimating stellar parameters from synthetic spectra as accurately as the FERRE template fitting method used by ASPCAP. StarNet also provides similarly precise stellar parameters as other data-driven methods (such as The Cannon) when trained on a large observational data sets. We have attempted to determine the errors in the StarNet predictions in a variety of ways, and show that the scatter in the results between the individual visits for a star are similar to our propagated and total errors, which are similar to (or smaller) than the intrinsic uncertainties in the optical analyses of benchmark stars.

In our applications on the APOGEE data sets, we also explore the limitations of the training sets, the sample sizes, the stellar parameter ranges, the impact of zero-flux values in real spectra during training and during testing, and the signal-to-noise of the spectra on the accuracy of the StarNet predictions. We note that our results are robust over a large range in S/N values for the APOGEE spectra, including low S/N ($\sim$15).

In the future, testing of the intrinsic errors in neural network models should be further examined, as well as variations in the synthetic spectral grids; e.g., variations in the model atmospheres adopted when generating the synthetic spectra, changes in the continuum normalization methods, as well as the exploration of different wavelength regions. We are especially interested in applying StarNet to optical spectroscopic surveys and observations.

The authors wish to thank Dr. Mike Irwin (Institute of Astronomy, Univ. of Cambridge) and Dr. Jo Bovy (University of Toronto) for helpful comments on this work,

and Drs. Vanessa Hill, Alejandra Recio-Blanco, and Patrick de Laverny (Observatoire de la Côte d'Azur, France) for many interesting discussions on spectral analyses. SB and TO thank the NRC Herzberg Astronomy and Astrophysics for funding through their co-op program. KAV, CK, and FJ acknowledge partial funding for this work through the NSERC Discovery Grants program.

Appendix B

Optical benchmark stars

In this Appendix, we tabulate the stellar parameters for stars in globular clusters that have both APOGEE DR13 results (based on IR spectral analyses) and results in the literature (based on high-resolution optical spectral analyses). Our systematic investigation has revealed numerous stars with incomplete optical parameters in the literature (e.g., missing $T_{\rm eff}$, $\log g$, or [Fe/H]), or incomplete IR parameters in the ASPCAP database (e.g., presumably due to data acquisition issues such as low S/N or persistence). We have removed those stars from our benchmark sample, as well as targets in the APOGEE database with a high RV scatter between individual visits (which usually indicates a potential binary system). Figure A.13 compares the stellar parameters for our final sample of optical benchmark stars (as listed below, with the obvious outliers removed). Small systematic offsets in $T_{\rm eff}$, $\log g$, and [Fe/H] are found, though typically within the quoted 1σ errors.

2MASS ID	Clus	APOGEE PERS Flag	ASPCAP parameters			Mean Optical parameters			StarNet Predictions			References
			T_{eff} [K]	$log(g)$ [dex]	$[Fe/H]$ [dex]	T_{eff} [K]	$log(g)$ [dex]	$[Fe/H]$ [dex]	T_{eff} [K]	$log(g)$ [dex]	$[Fe/H]$ [dex]	
Representative Errors			92	0.11	0.05	86	0.24	0.17	47	0.14	0.07	
2M16412709+3628002	M13	–	4184	0.81	-1.54	4348	0.98	-1.54	4201	0.96	-1.48	i, ad, ag, am
2M16413053+3629434	M13	–	4431	1.55	-1.39	4410	1.2	-1.44	4434	1.49	-1.34	ad, ag
2M16413072+3630075	M13	High	4816	2.21	-1.29	4750	1.9	-1.5	4809	2.2	-1.27	l
2M16413082+3630130	M13	–	4658	1.45	-1.58	4825	1.77	-1.55	4665	1.74	-1.56	l, ah
2M16413476+3627596	M13	–	4213	1.2	-1.33	4230	0.85	-1.44	4205	1.14	-1.3	ae, ag
2M16413482+3627197	M13	High	4171	1.17	-1.34	4173	0.7	-1.49	4157	1.12	-1.3	k, ae, ag
2M16413684+3629289	M13	–	4547	1.68	-1.43	4750	2.0	-1.48	4582	1.89	-1.5	ah
2M16413707+3630378	M13	–	4550	1.62	-1.48	4700	1.7	-1.58	4597	1.87	-1.49	ah
2M16413870+3625380	M13	High	4168	1.17	-1.31	4111	0.67	-1.56	4134	1.09	-1.29	g, k, ad, ae, ag, am
2M16413945+3632029	M13	–	4883	2.14	-1.41	4850	2.1	-1.56	4839	2.21	-1.44	ah
2M16414398+3622338	M13	High	4568	1.49	-1.47	4600	1.4	-1.55	4638	1.62	-1.45	l
2M16414478+3623273	M13	High	4529	1.67	-1.47	4625	1.65	-1.6	4522	1.57	-1.49	l, ah
2M16414528+3631068	M13	–	4679	1.8	-1.41	4600	1.6	-1.57	4742	2.0	-1.34	l, ah
2M16414558+3630328	M13	–	4711	1.86	-1.43	4750	1.9	-1.57	4781	2.19	-1.35	l
2M16414744+3628284	M13	–	4214	1.21	-1.34	4180	0.8	-1.46	4203	1.14	-1.32	ae, ag
2M16414932+3625264	M13	High	4686	1.99	-1.3	4600	1.6	-1.58	4736	2.05	-1.3	l
2M16415037+3623417	M13	High	4702	1.9	-1.4	4700	1.9	-1.54	4771	1.94	-1.35	ah
2M16415160+3629363	M13	High	4914	2.02	-1.38	4975	1.7	-1.68	4782	1.95	-1.51	ah
2M16415239+3628395	M13	High	4668	1.96	-1.39	4800	2.0	-1.52	4631	1.85	-1.52	l
2M16415842+3628312	M13	High	4860	2.28	-1.32	4900	2.0	-1.53	4754	2.18	-1.36	l
2M16415862+3627465	M13	High	4719	1.94	-1.49	4850	1.9	-1.64	4618	1.89	-1.43	ah
2M13131736+1814463	M53	–	4314	0.74	-1.84	4425	1.06	-2.04	4414	1.04	-1.79	ai
2M07380627+2136542	N2420	–	4725	2.55	-0.22	4850	2.6	-0.07	4725	2.56	-0.22	an

2M07381549+2138015	N2420	–	4872	2.57	-0.21	4800	2.6	-0.06	4890	2.57	-0.21	an
2M07382696+2138244	N2420	–	4832	2.48	-0.18	4800	2.6	-0.03	4825	2.48	-0.17	an
2M12100405+1832532	N4147	High	4235	1.12	-1.53	4383	1.1	-1.3	4270	0.92	-1.73	al
2M13414576+2824597	M3	–	4051	0.84	-1.46	4137	0.69	-1.62	4057	0.89	-1.46	k, s, z, ac, ad, ag, am
2M13421204+2826265	M3	–	3968	0.95	-1.27	4000	0.54	-1.64	3975	0.87	-1.27	s, z, ac, ad, ag, am
2M13421679+2823479	M3	–	4123	1.01	-1.33	4250	0.93	-1.42	4119	0.95	-1.32	k, ad, ag
2M13423922+2827574	M3	Low	4104	1.06	-1.27	4175	0.63	-1.48	4110	1.03	-1.3	aa, ac
2M13424150+2819081	M3	–	3853	0.55	-1.17	3966	0.45	-1.53	3910	0.98	-1.12	s, z, ac, ad, ag
2M14052071+2829419	N5466	High	4341	1.28	-1.8	4499	1.27	-1.94	4472	1.38	-1.67	ai
2M08514401+1146245	M67	High	5476	3.93	-0.02	5541	3.8	0.02	5363	3.62	-0.1	j
2M15174702+0204519	M5PAL5	–	4361	1.22	-1.25	4381	1.05	-1.53	4362	1.27	-1.25	v
2M15180831+0158530	M5PAL5	–	4840	1.73	-1.37	4961	1.84	-1.59	4861	1.9	-1.39	v
2M15180987+0210088	M5PAL5	Low	4557	1.45	-1.3	4630	1.44	-1.56	4558	1.53	-1.32	v
2M15181075+0212356	M5PAL5	Low	4698	1.85	-1.18	4740	1.82	-1.37	4710	1.99	-1.13	v
2M15181867+0204327	M5PAL5	Low	3995	1.04	-1.05	4113	0.73	-1.15	3996	1.09	-1.06	m, ag, al
2M15182262+0200305	M5PAL5	–	4035	1.05	-1.03	4100	0.66	-1.3	4034	1.11	-1.02	v
2M15182283+0203097	M5PAL5	–	4251	1.35	-1.11	4250	1.1	-1.12	4234	1.3	-1.11	m, ag
2M15182345+0159572	M5PAL5	–	4483	1.76	-1.02	4300	1.3	-1.11	4459	1.69	-1.01	m, ag
2M15182591+0205076	M5PAL5	–	4198	1.37	-1.06	4300	0.8	-1.02	4175	1.23	-1.07	m, ag
2M15183223+0201341	M5PAL5	–	4060	1.05	-1.06	4200	1.0	-1.09	4053	1.13	-1.06	m, ag
2M15183531+0207400	M5PAL5	–	4327	1.51	-1.19	4409	1.3	-1.35	4340	1.45	-1.19	ag, ak, al
2M15183738+0206079	M5PAL5	Low	4241	1.1	-1.17	4236	0.61	-1.49	4240	1.08	-1.2	v
2M15183765+0201212	M5PAL5	–	4839	2.31	-1.25	4845	2.2	-1.46	4835	2.28	-1.27	v
2M15184132+0205014	M5PAL5	–	4534	1.73	-1.19	4460	1.42	-1.34	4534	1.82	-1.2	v, ag, ak
2M15184164+0203533	M5PAL5	–	4128	1.19	-1.07	4128	0.83	-1.11	4103	1.09	-1.07	m, ag, al
2M15184346+0203074	M5PAL5	–	4581	1.82	-1.12	4475	1.3	-1.38	4615	1.91	-1.13	v
2M15184374+0208171	M5PAL5	Low	4938	2.37	-1.19	4860	2.25	-1.4	4865	2.29	-1.18	v
2M15184495+0202034	M5PAL5	–	3990	1.17	-1.0	4017	0.55	-1.3	3981	1.01	-1.02	al, am
2M15184540+0204302	M5PAL5	–	4223	1.14	-1.21	4266	0.8	-1.27	4222	1.11	-1.25	m, v, ag, al, am

2M15185515+0214337	M5PAL5	–	4487	1.38	-1.28	4584	1.3	-1.5	4489	1.51	-1.31	v
2M17163427+4307363	M92	–	4638	1.19	-2.24	4750	1.63	-2.54	4791	1.78	-1.86	y, af
2M17165185+4308031	M92	–	4620	1.41	-2.24	4740	1.75	-2.72	4761	1.73	-1.81	af
2M17165557+4309277	M92	–	4264	0.6	-2.19	4340	0.35	-2.27	4382	1.05	-1.93	ac
2M17165738+4307236	M92	–	4254	0.67	-2.15	4335	0.8	-2.28	4352	1.03	-1.95	o, y, ac, ag
2M17165772+4314115	M92	–	4443	1.11	-2.21	4615	1.48	-2.34	4515	1.34	-1.89	y, af
2M17165883+4315116	M92	–	4513	1.08	-2.2	4685	1.55	-2.34	4746	1.65	-1.78	y, af
2M17165956+4306456	M92	–	4618	1.35	-2.32	4880	1.9	-2.34	4723	1.63	-1.88	y
2M17165967+4301058	M92	High	4746	1.77	-2.11	4875	1.9	-2.34	4803	1.87	-1.73	y, af
2M17170033+4311478	M92	–	4680	1.26	-2.19	4830	1.75	-2.54	4677	1.54	-1.86	y, af
2M17170043+4305117	M92	–	4601	1.35	-2.19	4725	1.65	-2.5	4727	1.77	-1.84	y, af
2M17170081+4310251	M92	–	4531	1.19	-2.18	4630	1.52	-2.54	4655	1.6	-1.88	y, af
2M17170647+4306029	M92	–	4613	1.37	-2.22	4780	1.75	-2.55	4679	1.61	-1.88	af
2M17170731+4309308	M92	–	4447	1.05	-2.16	4540	1.2	-2.34	4532	1.33	-1.9	y
2M17171221+4302209	M92	High	4833	1.93	-2.08	4940	2.0	-2.35	4768	1.83	-1.73	af
2M17171307+4309483	M92	–	4341	0.88	-2.08	4373	0.87	-2.19	4470	1.28	-1.88	o, y, ag
2M17172166+4311031	M92	–	4611	1.38	-2.2	4880	1.85	-2.39	4693	1.63	-1.84	af
2M21290843+1209118	M15	–	4467	1.08	-2.14	4640	1.4	-2.37	4595	1.35	-1.91	y
2M21294465+1207307	M15	–	4451	0.96	-2.19	4610	1.35	-2.37	4570	1.26	-1.88	y
2M21294979+1211058	M15	Low	4303	0.69	-2.16	4423	0.86	-2.26	4475	1.15	-1.94	f, o, o, p, p, r, y, ag, ag
2M21295311+1212310	M15	–	4382	0.83	-2.22	4604	1.33	-2.34	4468	1.25	-1.98	e, y
2M21295492+1213225	M15	Low	4145	0.29	-2.27	4305	0.47	-2.39	4303	0.82	-1.95	e, n, p, p, y
2M21295560+1212422	M15	–	4395	0.8	-2.18	4429	0.79	-2.38	4498	1.13	-1.9	e, p, p
2M21295562+1210455	M15	–	4250	0.56	-2.16	4200	0.15	-2.37	4387	1.04	-1.92	p, p, y
2M21295618+1212337	M15	–	4327	0.77	-2.21	4418	0.76	-2.29	4489	1.17	-1.92	o, o, p, p, ag
2M21295666+1209463	M15	High	4120	0.28	-2.34	4269	0.3	-2.44	4274	0.81	-1.94	n, p, p, y
2M21295678+1210269	M15	–	4134	0.04	-2.27	4325	0.45	-2.42	4310	0.76	-1.98	p, p
2M21295801+1214260	M15	–	4605	1.29	-2.26	4855	2.0	-2.37	4569	1.32	-1.95	y
2M21295856+1209214	M15	–	4197	0.41	-2.23	4300	0.3	-2.43	4373	0.97	-1.97	n, p, p, y

2M21300033+1210508	M15	–	4292	0.68	-2.17	4341	0.43	-2.4	4427	1.08	-1.94	e, p, p
2M21300038+1207363	M15	–	4394	0.72	-2.26	4552	1.24	-2.4	4546	1.16	-2.0	e, y
2M21300224+1211215	M15	Low	4084	0.18	-2.29	4288	0.62	-2.39	4255	0.78	-1.96	e, p, p, y
2M21300274+1210438	M15	High	4271	0.59	-2.24	4275	0.5	-2.39	4432	1.05	-1.94	p, p, y
2M21300316+1213286	M15	–	4573	0.89	-2.24	4775	1.65	-2.37	4802	1.33	-1.87	y
2M21300637+1206592	M15	High	4430	0.6	-2.33	4625	1.3	-2.4	4640	1.2	-1.9	p, p, y
2M21300696+1207465	M15	–	4709	0.85	-2.3	4940	1.5	-2.37	4656	1.02	-1.93	y
2M21301049+1210061	M15	–	4486	1.02	-2.1	4470	1.07	-2.22	4668	1.41	-1.86	f, p, ag
2M21304412+1211226	M15	–	4539	1.01	-2.08	4640	1.4	-2.37	4741	1.54	-1.88	y
2M19533747+1844596	M71	High	4069	1.33	-0.7	4200	1.2	-0.83	4068	1.34	-0.69	q, ag
2M19533757+1847286	M71	High	3906	1.22	-0.58	3996	0.88	-0.43	3918	1.15	-0.56	q, x, ag
2M19533986+1843530	M71	High	4230	1.52	-0.68	4300	1.25	-0.7	4204	1.42	-0.66	q, ag
2M19534750+1846169	M71	High	4259	1.6	-0.65	4367	1.55	-0.72	4270	1.58	-0.65	a, q, ag, ak
2M19534827+1848021	M71	High	3979	1.33	-0.6	4055	0.8	-0.89	3968	1.19	-0.59	q, ab, ag
2M19535064+1849075	M71	High	4223	1.71	-0.65	4291	1.4	-0.83	4212	1.55	-0.65	a, q, ag, ak, al
2M19535325+1846471	M71	High	3896	1.15	-0.63	4099	0.8	-0.89	3922	1.11	-0.61	a, q, ab, ag
2M19205287+3745331	N6791	High	4500	2.58	0.3	4512	2.32	0.47	4520	2.37	0.32	c, u
2M19205629+3744334	N6791	High	4472	2.53	0.32	4473	2.33	0.56	4456	2.26	0.34	c, u
2M19411355+4012205	N6819	–	4802	2.51	0.02	4835	2.61	0.1	4805	2.61	0.01	d
2M19413031+4009005	N6819	–	4079	1.55	0.04	4046	1.77	-0.18	4082	1.54	0.04	w
2M23565751+5645272	N7789	–	4560	2.37	-0.01	4345	2.2	0.15	4562	2.36	-0.01	aj
2M06293009-3116587	N2243	–	4595	2.08	-0.47	4561	1.9	-0.69	4603	2.14	-0.48	h, t

1. Average error from the ASPCAP DR13 parameters.
2. Average standard deviation of the mean from multiple (N∼3) optical parameter sources.
3. Average statistical errors for StarNet predictions with respect to ASPCAP DR13 parameters.

Source references: (a) Leep et al. 1987; (b) Carretta et al. 2007; (c) Bragaglia et al. 2001; (d) Carretta et al. 2009; (e) Minniti et al. 1993; (f) Brown et al. 1991; (g) Gratton et al. 1994; (h) Peterson et al. 1980; (i) Randich et al. 2006; (j) Cavallo et al. 2000; (k) Lehnert et al. 1991; (l) Sneden et al. 1992; (m) Sobeck et al. 2011; (n) Sneden et al. 1991; (o) Sneden et al. 1997; (p) Sneden et al. 1994; (q) Cohen 1979; (r) Cohen 1978; (s) Gratton 1982; (t) Gratton et al. 2006; (u) Lai et al. 2011; (v) Molenda-Żakowicz et al. 2013; (w) Bessell 1983; (x) Sneden et al. 2000; (y) Luck & Bond 1981; (z) Kraft et al. 1999; (aa) Cohen 1980; (ab) Shetrone et al. 1998; (ac) Kraft et al. 1992; (ad) Kraft et al. 1993; (ae) Roederer & Sneden 2011; (af) Carretta & Gratton 1997; (ag) Kraft et al. 1997; (ah) Lamb et al. 2015; (ai) Pilachowski 1985; (aj) Gratton et al. 1986; (ak) Pilachowski et al. 1983; (al) Pilachowski et al. 1980; (am) Pancino et al. 2010

Bibliography

Abadi, M. et al. 2015, TensorFlow: Large-Scale Machine Learning on Heterogeneous Systems, software available from tensorflow.org

Abate, C., Pols, O. R., Izzard, R. G., Mohamed, S. S., & de Mink, S. E. 2013, Astronomy and Astrophysics, 552, A26

Abazajian, K. N. et al. 2009, Astrophysical Journal, Supplement Series, 182, 543

Alam, S. et al. 2015, Astrophysical Journal, Supplement Series, 219, 12

Allende Prieto, C., Beers, T. C., Wilhelm, R., Newberg, H. J., Rockosi, C. M., Yanny, B., & Lee, Y. S. 2006, Astrophysical Journal, 636, 804

Allende-Prieto, C., Sivarani, T., Beers, T., & et al. 2008, The Astronomical Journal, 136, 2070

Alonso, A., Arribas, S., & Martínez-Roger, C. 1999, Astronomy and Astrophysics, Supplement Series, 140, 261

An, D. et al. 2013, Astrophysical Journal, 763, 65

— 2009, Astrophysical Journal, Letters to the Editor, 707, L64

Anguiano, B. et al. 2015, Monthly Notices of the RAS, 451, 1229

Aoki, W., Beers, T. C., Christlieb, N., Norris, J. E., Ryan, S. G., & Tsangarides, S. 2007, Astrophysical Journal, 655, 492

Aoki, W., Beers, T. C., Honda, S., & Carollo, D. 2010, Astrophysical Journal, Letters to the Editor, 723, L201

Aoki, W. et al. 2013a, Astronomical Journal, 145, 13

— 2013b, Astronomical Journal, 145, 13

Argast, D., Samland, M., Thielemann, F.-K., & Qian, Y.-Z. 2004, Astronomy and Astrophysics, 416, 997

Arlandini, C., Käppeler, F., Wisshak, K., Gallino, R., Lugaro, M., Busso, M., & Straniero, O. 1999, Astrophysical Journal, 525, 886

Asplund, M., Grevesse, N., Sauval, A. J., & Scott, P. 2009, Annual Review of Astronomy and Astrophysics, 47, 481

Bailer-Jones, C. A. 2000, arXiv preprint astro-ph/0003071

Bailer-Jones, C. A., Irwin, M., Gilmore, G., & von Hippel, T. 1997, Monthly Notices of the Royal Astronomical Society, 292, 157

Beers, T. C. & Christlieb, N. 2005, Annual Review of Astronomy and Astrophysics, 43, 531

Beers, T. C., Preston, G. W., & Shectman, S. A. 1985, Astronomical Journal, 90, 2089

Belokurov, V. et al. 2009, Monthly Notices of the RAS, 397, 1748

— 2007, Astrophysical Journal, 654, 897

Bergstra, J. S., Bardenet, R., Bengio, Y., & Kégl, B. 2011, in Advances in Neural Information Processing Systems 24, ed. J. Shawe-Taylor, R. S. Zemel, P. L. Bartlett, F. Pereira, & K. Q. Weinberger (Curran Associates, Inc.), 2546–2554

Bessell, M. 1983, Publications of the Astronomical Society of the Pacific, 95, 94

Binney, J. et al. 2014, Monthly Notices of the RAS, 439, 1231

Bisterzo, S., Gallino, R., Straniero, O., Cristallo, S., & Käppeler, F. 2012, Monthly Notices of the RAS, 422, 849

Blackwell, D. E., Shallis, M. J., & Selby, M. J. 1979, Monthly Notices of the RAS, 188, 847

Boeche, C. et al. 2013a, Astronomy and Astrophysics, 553, A19

— 2014, Astronomy and Astrophysics, 568, A71

— 2013b, Astronomy and Astrophysics, 559, A59

— 2011, Astronomical Journal, 142, 193

Böhm-Vitense, E. 1989, Introduction to Stellar Astrophysics, 256

Bond, N. A. et al. 2010, Astrophysical Journal, 716, 1

Bonifacio, P. et al. 2015, Astronomy and Astrophysics, 579, A28

— 2009, Astronomy and Astrophysics, 501, 519

Bovy, J. 2016, Astrophysical Journal, 817, 49

Bovy, J., Rix, H.-W., & Hogg, D. W. 2012a, Astrophysical Journal, 751, 131

Bovy, J., Rix, H.-W., Hogg, D. W., Beers, T. C., Lee, Y. S., & Zhang, L. 2012b, Astrophysical Journal, 755, 115

Bovy, J., Rix, H.-W., Schlafly, E. F., Nidever, D. L., Holtzman, J. A., Shetrone, M., & Beers, T. C. 2016, Astrophysical Journal, 823, 30

Bragaglia, A. et al. 2001, The Astronomical Journal, 121, 327

Brown, J. A., Wallerstein, G., & Oke, J. 1991, The Astronomical Journal, 101, 1693

Burbidge, E. M., Burbidge, G. R., Fowler, W. A., & Hoyle, F. 1957, Reviews of Modern Physics, 29, 547

Burris, D. L., Pilachowski, C. A., Armandroff, T. E., Sneden, C., Cowan, J. J., & Roe, H. 2000, Astrophysical Journal, 544, 302

Caffau, E., Ludwig, H.-G., Steffen, M., Freytag, B., & Bonifacio, P. 2011, Sol. Phys., 268, 255

Carney, B. W., Latham, D. W., Stefanik, R. P., Laird, J. B., & Morse, J. A. 2003, Astronomical Journal, 125, 293

Carollo, D. et al. 2012, Astrophysical Journal, 744, 195

— 2010, Astrophysical Journal, 712, 692

Carollo, D., Freeman, K., Beers, T. C., Placco, V. M., Tumlinson, J., & Martell, S. L. 2014, Astrophysical Journal, 788, 180

Carretta, E., Bragaglia, A., & Gratton, R. 2007, Astronomy & Astrophysics, 473, 129

Carretta, E. et al. 2009, Astronomy & Astrophysics, 505, 117

Carretta, E. & Gratton, R. 1997, Astronomy and Astrophysics Supplement Series, 121, 95

Casagrande, L., Ramírez, I., Meléndez, J., Bessell, M., & Asplund, M. 2010, Astronomy and Astrophysics, 512, A54

Casey, A. R., Hogg, D. W., Ness, M., Rix, H.-W., Ho, A. Q., & Gilmore, G. 2016, arXiv preprint arXiv:1603.03040

Casey, A. R. & Schlaufman, K. C. 2015, Astrophysical Journal, 809, 110

Cayrel, R. et al. 2004, Astronomy and Astrophysics, 416, 1117

Chen, S., Billings, S., & Grant, P. 1990, International journal of control, 51, 1191

Chiappini, C., Hirschi, R., Meynet, G., Ekström, S., Maeder, A., & Matteucci, F. 2006, Astronomy and Astrophysics, 449, L27

Chollet, F. et al. 2015, Keras, `https://github.com/fchollet/keras`

Choplin, A., Ekström, S., Meynet, G., Maeder, A., Georgy, C., & Hirschi, R. 2017, Astronomy and Astrophysics, 605, A63

Christlieb, N. 2003, in Reviews in Modern Astronomy, Vol. 16, Reviews in Modern Astronomy, ed. R. E. Schielicke, 191

Christlieb, N., Green, P. J., Wisotzki, L., & Reimers, D. 2001, Astronomy and Astrophysics, 375, 366

Christlieb, N., Wisotzki, L., & Graßhoff, G. 2002, Astronomy and Astrophysics, 391, 397

Clayton, D. D. 1983, Principles of stellar evolution and nucleosynthesis

Cohen, J. 1978, The Astrophysical Journal, 223, 487

— 1979, The Astrophysical Journal, 231, 751

— 1980, The Astrophysical Journal, 241, 981

Cohen, J. G. et al. 2004, Astrophysical Journal, 612, 1107

Cohen, J. G., Christlieb, N., Thompson, I., McWilliam, A., Shectman, S., Reimers, D., Wisotzki, L., & Kirby, E. 2013, Astrophysical Journal, 778, 56

Côté, B., Belczynski, K., Fryer, C. L., Ritter, C., Paul, A., Wehmeyer, B., & O'Shea, B. W. 2017, Astrophysical Journal, 836, 230

Côté, B., O'Shea, B. W., Ritter, C., Herwig, F., & Venn, K. A. 2016a, ArXiv e-prints

Côté, B., Ritter, C., O'Shea, B. W., Herwig, F., Pignatari, M., Jones, S., & Fryer, C. L. 2016b, Astrophysical Journal, 824, 82

Cristallo, S. et al. 2011, Astrophysical Journal, Supplement Series, 197, 17

Cunha, K. et al. 2015, The Astrophysical Journal Letters, 798, L41

Da Costa, G. S. & Armandroff, T. E. 1990, Astronomical Journal, 100, 162

Dalton, G. et al. 2016, in Proc. SPIE, Vol. 9908, Society of Photo-Optical Instrumentation Engineers (SPIE) Conference Series, 99081G

Dalton, G. et al. 2014, in Proc. SPIE, Vol. 9147, Ground-based and Airborne Instrumentation for Astronomy V, 91470L

Dalton, G. et al. 2012, in Proc. SPIE, Vol. 8446, Ground-based and Airborne Instrumentation for Astronomy IV, 84460P

Dardelet, L. et al. 2015, ArXiv e-prints

de Jong, R. S. et al. 2016, in Proc. SPIE, Vol. 9908, Society of Photo-Optical Instrumentation Engineers (SPIE) Conference Series, 99081O

De Silva, G. M. et al. 2015, Monthly Notices of the RAS, 449, 2604

Dotter, A., Chaboyer, B., Jevremović, D., Kostov, V., Baron, E., & Ferguson, J. W. 2008, The Astrophysical Journal Supplement Series, 178, 89

Eisenstein, D. J. et al. 2011, Astronomical Journal, 142, 72

Fernández-Alvar, E. et al. 2017, Monthly Notices of the RAS, 465, 1586

Fernández-Trincado, J. G. et al. 2015, Astronomy and Astrophysics, 583, A76

François, P. et al. 2007, Astronomy and Astrophysics, 476, 935

Frebel, A., Christlieb, N., Norris, J. E., Aoki, W., & Asplund, M. 2006, Astrophysical Journal, Letters to the Editor, 638, L17

Frebel, A. & Norris, J. E. 2015, Annual Review of Astronomy and Astrophysics, 53, 631

Frebel, A., Simon, J. D., Geha, M., & Willman, B. 2010, Astrophysical Journal, 708, 560

Freeman, K. & Bland-Hawthorn, J. 2002, Annual Review of Astronomy and Astrophysics, 40, 487

Freiburghaus, C., Rosswog, S., & Thielemann, F.-K. 1999, Astrophysical Journal, Letters to the Editor, 525, L121

García Pérez, A. E. et al. 2015, ArXiv e-prints

— 2016, Astronomical Journal, 151, 144

Gilmore, G. et al. 2013, The Messenger, 151, 25

— 2012a, The Messenger, 147, 25

— 2012b, The Messenger, 147, 25

Gómez, F. A. et al. 2012, Monthly Notices of the RAS, 423, 3727

Goswami, A. 2005, Monthly Notices of the RAS, 359, 531

Gratton, R. 1982, The Astrophysical Journal, 257, 640

Gratton, R., Bragaglia, A., Carretta, E., & Tosi, M. 2006, The Astrophysical Journal, 642, 462

Gratton, R. G., Quarta, M. L., & Ortolani, S. 1986, Astronomy and Astrophysics, 169, 208

Gratton, R. G., Sneden, C., Carretta, E., & Bragaglia, A. 2000, Astronomy and Astrophysics, 354, 169

Gurney, K. 1997, An introduction to neural networks (CRC press)

Gustafsson, B., Edvardsson, B., Eriksson, K., Jørgensen, U. G., Nordlund, Å., & Plez, B. 2008, Astronomy and Astrophysics, 486, 951

Hampel, M., Stancliffe, R. J., Lugaro, M., & Meyer, B. S. 2016, Astrophysical Journal, 831, 171

Han, Z., Eggleton, P. P., Podsiadlowski, P., & Tout, C. A. 1995, Monthly Notices of the RAS, 277, 1443

Hansen, C. J. et al. 2016a, Astronomy and Astrophysics, 588, A37

Hansen, T. et al. 2015, Astrophysical Journal, 807, 173

Hansen, T. T., Andersen, J., Nordström, B., Beers, T. C., Placco, V. M., Yoon, J., & Buchhave, L. A. 2016b, Astronomy and Astrophysics, 586, A160

— 2016c, ArXiv e-prints

Hasselquist, S. et al. 2017, Astrophysical Journal, 845, 162

Hawkins, K., Masseron, T., Jofré, P., Gilmore, G., Elsworth, Y., & Hekker, S. 2016, Astronomy and Astrophysics, 594, A43

He, K., Zhang, X., Ren, S., & Sun, J. 2015, CoRR, abs/1502.01852

Heger, A. & Woosley, S. E. 2010, Astrophysical Journal, 724, 341

Herwig, F. 2005, Annual Review of Astronomy and Astrophysics, 43, 435

Hill, V., Christlieb, N., Beers, T. C., Barklem, P. S., Kratz, K.-L., Nordström, B., Pfeiffer, B., & Farouqi, K. 2016, ArXiv e-prints

Hirschi, R. 2007, Astronomy and Astrophysics, 461, 571

Holtzman, J. A. et al. 2015, Astronomical Journal, 150, 148

Holtzman, J. A. et al. 2015, The Astronomical Journal, 150, 148

Honda, S., Aoki, W., Arimoto, N., & Sadakane, K. 2011, Publications of the ASJ, 63, 523

Howes, L. M. et al. 2014, Monthly Notices of the RAS, 445, 4241

— 2016, Monthly Notices of the RAS, 460, 884

— 2015, Nature, 527, 484

Ishigaki, M. N., Tominaga, N., Kobayashi, C., & Nomoto, K. 2014, Astrophysical Journal, Letters to the Editor, 792, L32

Iwamoto, N. & Saio, H. 1999, Astrophysical Journal, 521, 297

Jahandar, F. et al. 2017, ArXiv e-prints

Jonsell, K., Barklem, P. S., Gustafsson, B., Christlieb, N., Hill, V., Beers, T. C., & Holmberg, J. 2006, Astronomy and Astrophysics, 451, 651

Keller, S. C. et al. 2007, PASA, 24, 1

Kingma, D. & Ba, J. 2014, arXiv preprint arXiv:1412.6980

Kippenhahn, R. & Weigert, A. 1994, Stellar Structure and Evolution, 192

Klement, R. et al. 2009, Astrophysical Journal, 698, 865

Koch, A., McWilliam, A., Preston, G. W., & Thompson, I. B. 2016, Astronomy and Astrophysics, 587, A124

Koesterke, L., Prieto, C. A., & Lambert, D. L. 2008, The Astrophysical Journal, 680, 764

Kraft, R. P., Peterson, R. C., Guhathakurta, P., Sneden, C., Fulbright, J. P., & Langer, G. E. 1999, The Astrophysical Journal Letters, 518, L53

Kraft, R. P., Sneden, C., Langer, G., & Prosser, C. F. 1992, The Astronomical Journal, 104, 645

Kraft, R. P., Sneden, C., Langer, G., & Shetrone, M. D. 1993, The Astronomical Journal, 106, 1490

Kraft, R. P., Sneden, C., Smith, G. H., Shetrone, M. D., Langer, G., & Pilachowski, C. A. 1997, The Astronomical Journal, 113, 279

Kunder, A. et al. 2014, Astronomy and Astrophysics, 572, A30

Lai, D. K., Lee, Y. S., Bolte, M., Lucatello, S., Beers, T. C., Johnson, J. A., Sivarani, T., & Rockosi, C. M. 2011, Astrophysical Journal, 738, 51

Lai, D. K., Smith, G. H., Bolte, M., Johnson, J. A., Lucatello, S., Kraft, R. P., & Sneden, C. 2011, The Astronomical Journal, 141, 62

Lamb, M. et al. 2017, Monthly Notices of the RAS, 465, 3536

Lamb, M., Venn, K., Shetrone, M., Sakari, C., & Pritzl, B. 2015, Monthly Notices of the Royal Astronomical Society, 448, 42

Lamb, M. P., Venn, K. A., Shetrone, M. D., Sakari, C. M., & Pritzl, B. J. 2015, Monthly Notices of the RAS, 448, 42

Lardo, C. et al. 2016, Astronomy and Astrophysics, 585, A70

— 2012, Astronomy and Astrophysics, 541, A141

Lee, Y., Beers, T., Allende-Prieto, C., & et al. 2011a, The Astronomical Journal, 141, 90

Lee, Y., Beers, T., Sivarani, T., & et al. 2008, The Astronomical Journal, 136, 2022

Lee, Y. S. et al. 2011b, Astrophysical Journal, 738, 187

Lee, Y. S., Beers, T. C., Kim, Y. K., Placco, V., Yoon, J., Carollo, D., Masseron, T., & Jung, J. 2017, Astrophysical Journal, 836, 91

Lee, Y. S. et al. 2013, Astronomical Journal, 146, 132

Leep, E. M., Wallerstein, G., & Oke, J. 1987, The Astronomical Journal, 93, 338

Lehnert, M., Bell, R., & Cohen, J. 1991, The Astrophysical Journal, 367, 514

Letarte, B. et al. 2010, Astronomy and Astrophysics, 523, A17

Li, X.-R., Pan, R.-Y., & Duan, F.-Q. 2017, Research in Astronomy and Astrophysics, 17, 036

Lucatello, S., Tsangarides, S., Beers, T. C., Carretta, E., Gratton, R. G., & Ryan, S. G. 2005, Astrophysical Journal, 625, 825

Luck, R. & Bond, H. 1981, The Astrophysical Journal, 244, 919

Maaten, L. v. d. & Hinton, G. 2008, Journal of Machine Learning Research, 9, 2579

Maeder, A., Meynet, G., & Chiappini, C. 2015, Astronomy and Astrophysics, 576, A56

Majewski, S. R. et al. 2015, ArXiv e-prints

Manteiga, M., Ordóñez, D., Dafonte, C., & Arcay, B. 2010, Publications of the Astronomical Society of the Pacific, 122, 608

Martell, S. L. & Grebel, E. K. 2010, Astronomy and Astrophysics, 519, A14

Martell, S. L. et al. 2016, Astrophysical Journal, 825, 146

Mashonkina, L., Jablonka, P., Sitnova, T., Pakhomov, Y., & North, P. 2017, ArXiv e-prints

Matsuno, T., Aoki, W., Beers, T. C., Lee, Y. S., & Honda, S. 2017, Astronomical Journal, 154, 52

McClure, R. D. & Woodsworth, A. W. 1990, Astrophysical Journal, 352, 709

McConnachie, A. W. et al. 2016, ArXiv e-prints

McWilliam, A., Preston, G. W., Sneden, C., & Searle, L. 1995, Astronomical Journal, 109, 2757

Mészáros, S. et al. 2013, Astronomical Journal, 146, 133

Mészáros, S. et al. 2013, The Astronomical Journal, 146, 133

— 2015, The Astronomical Journal, 149, 153

— 2012, The Astronomical Journal, 144, 120

Meynet, G., Ekström, S., & Maeder, A. 2006, Astronomy and Astrophysics, 447, 623

Meynet, G. & Maeder, A. 2002, Astronomy and Astrophysics, 381, L25

Minniti, D., Olszewski, E. W., & Rieke, M. 1993, The Astrophysical Journal, 410, L79

Molenda-Żakowicz, J. et al. 2013, Monthly Notices of the Royal Astronomical Society, stt1095

Ness, M., Hogg, D. W., Rix, H.-W., Ho, A. Y., & Zasowski, G. 2015, The Astrophysical Journal, 808, 16

Newberg, H. J., Willett, B. A., Yanny, B., & Xu, Y. 2010, Astrophysical Journal, 711, 32

Nidever, D. L. et al. 2015, Astronomical Journal, 150, 173

Nidever, D. L. et al. 2015, The Astronomical Journal, 150, 173

Nomoto, K., Kobayashi, C., & Tominaga, N. 2013, Annual Review of Astronomy and Astrophysics, 51, 457

Nomoto, K., Tominaga, N., Umeda, H., Kobayashi, C., & Maeda, K. 2006, Nuclear Physics A, 777, 424

Norris, J. E., Christlieb, N., Korn, A. J., Eriksson, K., Bessell, M. S., Beers, T. C., Wisotzki, L., & Reimers, D. 2007, Astrophysical Journal, 670, 774

Norris, J. E., Gilmore, G., Wyse, R. F. G., Yong, D., & Frebel, A. 2010a, Astrophysical Journal, Letters to the Editor, 722, L104

Norris, J. E., Wyse, R. F. G., Gilmore, G., Yong, D., Frebel, A., Wilkinson, M. I., Belokurov, V., & Zucker, D. B. 2010b, Astrophysical Journal, 723, 1632

Norris, J. E. et al. 2013, Astrophysical Journal, 762, 28

North, P. et al. 2012, Astronomy and Astrophysics, 541, A45

Paczyński, B. 1965, , 15, 89

Pancino, E., Carrera, R., Rossetti, E., & Gallart, C. 2010, Astronomy & Astrophysics, 511, A56

Pancino, E., Lardo, C., Altavilla, G., & et al. 2017, Astronomy and Astrophysics, 598, 5

Pérez, A. E. G. et al. 2016, The Astronomical Journal, 151, 144

Piffl, T. et al. 2014a, Monthly Notices of the RAS, 445, 3133

— 2014b, Astronomy and Astrophysics, 562, A91

Pilachowski, A. 1985, Publications of the Astronomical Society of the Pacific, 97, 801

Pilachowski, C., Leep, E., & Wallerstein, G. 1980, The Astrophysical Journal, 236, 508

Pilachowski, C., Sneden, C., & Wallerstein, G. 1983, The Astrophysical Journal Supplement Series, 52, 241

Placco, V. M., Frebel, A., Beers, T. C., Karakas, A. I., Kennedy, C. R., Rossi, S., Christlieb, N., & Stancliffe, R. J. 2013, Astrophysical Journal, 770, 104

Placco, V. M., Frebel, A., Beers, T. C., & Stancliffe, R. J. 2014, Astrophysical Journal, 797, 21

Placco, V. M. et al. 2011, Astronomical Journal, 142, 188

— 2010, Astronomical Journal, 139, 1051

Preston, G. W. & Sneden, C. 2001, Astronomical Journal, 122, 1545

Ramírez, I. & Meléndez, J. 2005, Astrophysical Journal, 626, 446

Randich, S., Sestito, P., Primas, F., Pallavicini, R., & Pasquini, L. 2006, Astronomy & Astrophysics, 450, 557

Recio-Blanco, e. a. 2016, Astronomy and Astrophysics, 589, 22

— 2017, Astronomy and Astrophysics, 602, 6

Roederer, I. U., Karakas, A. I., Pignatari, M., & Herwig, F. 2016, Astrophysical Journal, 821, 37

Roederer, I. U., Preston, G. W., Thompson, I. B., Shectman, S. A., & Sneden, C. 2014a, Astrophysical Journal, 784, 158

Roederer, I. U., Preston, G. W., Thompson, I. B., Shectman, S. A., Sneden, C., Burley, G. S., & Kelson, D. D. 2014b, Astronomical Journal, 147, 136

— 2014c, Astronomical Journal, 147, 136

Roederer, I. U. & Sneden, C. 2011, The Astronomical Journal, 142, 22

Rossi, S., Beers, T. C., Sneden, C., Sevastyanenko, T., Rhee, J., & Marsteller, B. 2005, Astronomical Journal, 130, 2804

Ruchti, G. R. et al. 2010, Astrophysical Journal, Letters to the Editor, 721, L92

— 2011, Astrophysical Journal, 737, 9

Salvadori, S. & Ferrara, A. 2009, Monthly Notices of the RAS, 395, L6

Salvadori, S., Skúladóttir, Á., & Tolstoy, E. 2015, Monthly Notices of the RAS, 454, 1320

Santucci, R. M. et al. 2015, Astrophysical Journal, Letters to the Editor, 813, L16

Schlaufman, K. C. & Casey, A. R. 2014, Astrophysical Journal, 797, 13

Schlesinger, K. J. et al. 2012, Astrophysical Journal, 761, 160

Schmidt, S. J., Wagoner, E. L., Johnson, J. A., Davenport, J. R. A., Stassun, K. G., Souto, D., & Ge, J. 2016, Monthly Notices of the RAS, 460, 2611

SDSS Collaboration et al. 2016, ArXiv e-prints

Shetrone, M. et al. 2015, Astrophysical Journal, Supplement Series, 221, 24

Shetrone, M., Venn, K. A., Tolstoy, E., Primas, F., Hill, V., & Kaufer, A. 2003, Astronomical Journal, 125, 684

Shetrone, M. D., Bolte, M., & Stetson, P. B. 1998, The Astronomical Journal, 115, 1888

Shetrone, M. D., Côté, P., & Sargent, W. L. W. 2001, Astrophysical Journal, 548, 592

Simon, J. D. et al. 2011, Astrophysical Journal, 733, 46

Singh, H. P., Gulati, R. K., & Gupta, R. 1998, Monthly Notices of the Royal Astronomical Society, 295, 312

Skrutskie, M. F. et al. 2006a, Astronomical Journal, 131, 1163

— 2006b, Astronomical Journal, 131, 1163

Skúladóttir, Á., Tolstoy, E., Salvadori, S., Hill, V., Pettini, M., Shetrone, M. D., & Starkenburg, E. 2015, Astronomy and Astrophysics, 574, A129

Smiljanic, R. et al. 2014, Astronomy and Astrophysics, 570, A122

Smith, M. C. et al. 2009, Monthly Notices of the RAS, 399, 1223

— 2007, Monthly Notices of the RAS, 379, 755

Smith, V. V. et al. 2013, Astrophysical Journal, 765, 16

Sneden, C., Cowan, J. J., & Gallino, R. 2008, Annual Review of Astronomy and Astrophysics, 46, 241

Sneden, C., Kraft, R. P., Guhathakurta, P., Peterson, R. C., & Fulbright, J. P. 2004, Astronomical Journal, 127, 2162

Sneden, C., Kraft, R. P., Langer, G., Prosser, C. F., & Shetrone, M. D. 1994, The Astronomical Journal, 107, 1773

Sneden, C., Kraft, R. P., Prosser, C. F., & Langer, G. 1991, The Astronomical Journal, 102, 2001

— 1992, The Astronomical Journal, 104, 2121

Sneden, C., Kraft, R. P., Shetrone, M. D., Smith, G. H., Langer, G., & Prosser, C. F. 1997, The Astronomical Journal, 114, 1964

Sneden, C., Pilachowski, C. A., & Kraft, R. P. 2000, The Astronomical Journal, 120, 1351

Sneden, C., Preston, G. W., & Cowan, J. J. 2003, Astrophysical Journal, 592, 504

Sobeck, J. S. et al. 2011, The Astronomical Journal, 141, 175

Soubiran, C., Le Campion, J.-F., Brouillet, N., & Chemin, L. 2016, Astronomy and Astrophysics, 591, A118

Spite, M., Caffau, E., Bonifacio, P., Spite, F., Ludwig, H.-G., Plez, B., & Christlieb, N. 2013, Astronomy and Astrophysics, 552, A107

Spite, M. et al. 2006, Astronomy and Astrophysics, 455, 291

— 2005, Astronomy and Astrophysics, 430, 655

Starkenburg, E. et al. 2013, Astronomy and Astrophysics, 549, A88

— 2017, ArXiv e-prints

Starkenburg, E., Shetrone, M. D., McConnachie, A. W., & Venn, K. A. 2014, Monthly Notices of the RAS, 441, 1217

Steigman, G. 2007, Annual Review of Nuclear and Particle Science, 57, 463

Steinmetz, M. et al. 2006, Astronomical Journal, 132, 1645

Susa, H., Hasegawa, K., & Tominaga, N. 2014, Astrophysical Journal, 792, 32

Takada, M. et al. 2014, Publications of the ASJ, 66, R1

Tinsley, B. M. 1979, Astrophysical Journal, 229, 1046

Tolstoy, E., Hill, V., & Tosi, M. 2009, Annual Review of Astronomy and Astrophysics, 47, 371

Tominaga, N., Iwamoto, N., & Nomoto, K. 2014, Astrophysical Journal, 785, 98

Travaglio, C., Gallino, R., Arnone, E., Cowan, J., Jordan, F., & Sneden, C. 2004, Astrophysical Journal, 601, 864

Tsujimoto, T. & Shigeyama, T. 2014, Astrophysical Journal, Letters to the Editor, 795, L18

Umeda, H. & Nomoto, K. 2003, Nature, 422, 871

Umeda, H., Tominaga, N., Iwamoto, N., Nomoto, K., & Maeda, K. 2006, in American Institute of Physics Conference Series, Vol. 847, Origin of Matter and Evolution of Galaxies, ed. S. Kubono, W. Aoki, T. Kajino, T. Motobayashi, & K. Nomoto, 65–70

Vanture, A. D. 1992, Astronomical Journal, 103, 2035

Venn, e. a. 2012, Astrophysical Journal, 715, 25

Venn, K. A., Irwin, M., Shetrone, M. D., Tout, C. A., Hill, V., & Tolstoy, E. 2004, Astronomical Journal, 128, 1177

Venn, K. A., Tolstoy, E., Kaufer, A., Skillman, E. D., Clarkson, S. M., Smartt, S. J., Lennon, D. J., & Kudritzki, R. P. 2003, Astronomical Journal, 126, 1326

Von Hippel, T., Storrie-Lombardi, L., Storrie-Lombardi, M., & Irwin, M. 1994, Monthly Notices of the Royal Astronomical Society, 269, 97

Wang, K., Guo, P., & Luo, A.-L. 2017, Monthly Notices of the RAS, 465, 4311

Williams, M. E. K. et al. 2013, Monthly Notices of the RAS, 436, 101

— 2011, Astrophysical Journal, 728, 102

Wilson, M. L. et al. 2011, Monthly Notices of the RAS, 413, 2235

Woosley, S. E., Wilson, J. R., Mathews, G. J., Hoffman, R. D., & Meyer, B. S. 1994, Astrophysical Journal, 433, 229

Wright, E. L. et al. 2010, Astronomical Journal, 140, 1868

Wylie-de Boer, E., Freeman, K., Williams, M., Steinmetz, M., Munari, U., & Keller, S. 2012, Astrophysical Journal, 755, 35

Yanny, B. et al. 2009a, Astrophysical Journal, 700, 1282

— 2009b, Astronomical Journal, 137, 4377

Yanny, B. et al. 2009, The Astronomical Journal, 137, 4377

Yong, D., Grundahl, F., Johnson, J. A., & Asplund, M. 2008, Astrophysical Journal, 684, 1159

Yong, D. et al. 2013a, Astrophysical Journal, 762, 26

— 2013b, Astrophysical Journal, 762, 27

Yoon, J. et al. 2016, ArXiv e-prints

Youakim, K. et al. 2017, ArXiv e-prints

Zacharias, N., Monet, D. G., Levine, S. E., Urban, S. E., Gaume, R., & Wycoff, G. L. 2005, VizieR Online Data Catalog, 1297

Zamora, O. et al. 2015, Astronomical Journal, 149, 181

Zasowski, G. et al. 2013, Astronomical Journal, 146, 81